UNIVERSITÀ DEGLI STUDI DI MILANO

Dottorato di Ricerca in Scienze della Terra
Ciclo XXVII

Particle size effect on kinetics and thermodynamics of phase transitions in minerals

Ph.D. Thesis

Lucia Pagliari
ID Number R09569

Tutor
Prof.ssa Monica Dapiaggi

Co-Tutor
Prof. Alessandro Pavese

Academic Year
2013-2014

Coordinator
Prof.ssa Elisabetta Erba

Contents

Research Aim

Phase transitions in minerals are transformations naturally occurring when environmental conditions, such as pressure and temperature, change. So, studying their evolution means to understand the modifications of the physical and structural properties of a compound, which can be controlled through industrial processes and exploited in technological applications.

On this ground, the present thesis is divided into two big sectors of material science: after a short overview on the basic theory of thermodynamics and kinetics (Part I), the first branch deals with traditional ceramics (Part II), where interest is focused on quartz-cristobalite-tridymite-involving reactions; after that, the field of functional ceramics is discussed in Part III, analysing the behaviour at the nano scale of two widely studied technological materials: the half-doped La and Ca manganite and the tetragonal zirconia stabilized at room temperature by size reduction.

All these subjects of study are treated considering the effect of varying the particle size. It is well known, indeed, that reactions are promoted when particles have a greater surface to volume ratio. Therefore, when investigating phase transitions, solid state reactivity and kinetics must reflect the effect of the reduction of grain size. Knowing the mechanisms and the behaviour of materials undergoing low or high temperature processes is essential for industrial procedures to be developed. Thus, phase transitions of the cited compounds are here discussed, in the light of three completely different but complementary approaches:

1. as already mentioned, Chapter 2 is aimed at the investigation of the quartz-tridymite-cristobalite phase transition, starting from industrially-used quartz powders of different particle size distributions (PSD). Several experiments were performed on pure quartz as well as quartz mixed with a mineralizing agent (*i.e.* KOH and NaOH dissolved in two separate aqueous solutions), applying different high temperatures and dwell times and preparing the samples with different methods. *Ex-situ* and *in-situ* analyses by means of X-ray Powder Diffraction (XRPD) were conducted, in order to evaluate the amounts of the high temperature (HT) phases formed after firing and the crystallization temperatures of each polymorph. Moreover, a full isothermal kinetic study, interpreted with an Avrami-like model, was carried out by HT-XRPD on pure quartz powders, as we were dealing with a simple polymorphic phase transition. Comparisons between the two main methods of sample preparation (*i.e.* quartz with or without mineralizer) were pointed out, as well as the influence of PSD and working temperatures and times on the high temperature phase transitions and their mechanisms.

2. Chapter 3 deals with the study of $La_{0.5}Ca_{0.5}MnO_3$ (LCMO) from the point of view of the elastic properties. Strain data were collected through Resonant Ultrasound Spectroscopy (RUS) on nanocrystalline and bulk samples (previously synthesized as powders and studied by Sarkar et al. (2008), and then sintered with High Pressure Field Assisted Rapid Sintering (HP-FARS) apparatus for the research presented here), in order to make inspection on their structural and magnetic phase transitions at low temperatures, through the analysis of changes in their elastic properties. XRPD measurements were conducted just to check the grain size not to be significantly changed after sinterization, while magnetic data collections were carried out using a

Superconducting Quantum Interference Device (SQuID) magnetometer, so to correlate directly the elastic and magnetic anomalies observed in the samples. Evaluations on the coupling between strain and the order parameter associated to each phase transition were made, looking over the influence of grain size and, in particular, of nanocrystallinity.

3. Chapter 4 looks at the stabilization at room conditions of the HT tetragonal zirconia polymorph through the reduction of crystallite size. Nanocrystalline undoped and weakly doped with $YO_{1.5}$ powders were measured at high Q_{max} with XRPD, at the beamline ID31 of European Synchrotron Radiation Facility (ESRF) in Grenoble, so to obtain high resolution data and distinguish detailed information of the structure of the material under study. Reciprocal-space as well as direct-space refinements were performed, with the aim to investigate both the average and the local structure of the tetragonal zirconia. Particular attention has been given to atomic scale analysis, which allowed to understand the local environment of the structure and highlight the role of particle size reduction in the stabilization, via strain induction, of the tetragonal phase outside its stability field.

Part I

Theory of phase transitions

Chapter 1

Thermodynamics and kinetics of phase transitions. Basic concepts

By definition, a *phase* is a physically distinct homogenous part of a thermodynamic system, throughout which all physical, chemical, structural, etc. properties of the material are essentially uniform, and that can be separated from other parts of the system by boundary surfaces. Going from one of these domains to another is what is called a *phase transition*.

Phase transitions can be described in terms of classical thermodynamics. They are, indeed, induced by changes of at least one intensive thermodynamic variable characterizing the system (such as temperature or pressure), which lead the original phase to be unstable and transform to another one, in the direction of a free energy minimum, *i.e.* towards an equilibrium state. This Chapter will outline the basic thermodynamic and kinetic concepts that are involved in defining mineral equilibrium and reactions. Most of the theoretical material here outlined is liberally taken from the very well-written textbook "Introduction to mineral siences", by A. Putnis.

1.1 Basic thermodynamics

1.1.1 Enthalpy and heat capacity

The *internal energy*, U, of a mineral structure is the sum of the potential stored in the interatomic bonding and the kinetic energy of the atomic vibrations. When heat is added to the system, the kinetic energy (and hence the temperature) increases, and so does the internal energy. However, if a crystal is allowed to expand, it does some work on its surroundings, and thus the total change in the internal energy is expressed by the First Law of Thermodynamics:

$$\mathrm{d}U = \mathrm{d}Q - P\mathrm{d}V, \tag{1.1}$$

where $\mathrm{d}Q$ is the change in heat content and $P\mathrm{d}V$ is the amount of work done, P being the pressure and $\mathrm{d}V$ the change in volume.

In order to be able to classify preocesses in terms of heat evolved or absorbed, it is convenient to define two energy functions: *enthalphy*, H, and *heat capacity*, C. The former is described as

$$H = U + PV, \tag{1.2}$$

the latter is the amount of heat $\mathrm{d}Q$ involved in changing the temperature of a mole of material by $\mathrm{d}T$:

$$C = \frac{\mathrm{d}Q}{\mathrm{d}T}. \tag{1.3}$$

C has different definitions depending on the variable held constant in the system, if the constant variable of the system is volume or pressure. Dividing the terms in Eq. 1.1 by $\mathrm{d}T$ gives

$$\frac{\mathrm{d}U}{\mathrm{d}T} = \frac{\mathrm{d}Q}{\mathrm{d}T} - p\frac{\mathrm{d}V}{\mathrm{d}T}. \tag{1.4}$$

If the volume is held constant, then $\frac{\mathrm{d}V}{\mathrm{d}T} = 0$ and

$$\left(\frac{\partial U}{\partial T}\right)_V = \left(\frac{\partial Q}{\partial T}\right)_V = C_V, \tag{1.5}$$

where C_V is the heat capacity at constant volume.
If the pressure is held constant, then $\frac{\mathrm{d}p}{\mathrm{d}T} = 0$ and

$$\left(\frac{\partial H}{\partial T}\right)_P = \left(\frac{\partial Q}{\partial T}\right)_P = C_P, \tag{1.6}$$

where C_P is the heat capacity at constant pressure.
In solids, $(C_P - C_V)$ is very small and becomes significant only at high temperatures (>∼1500 K). It can be shown that

$$C_P - C_V = TV\frac{\alpha^2}{\beta}, \tag{1.7}$$

where α is the thermal expansion coefficient, while β is the compressibility. α and β reflect the response of the bond angles and bond lenghts to changes in T and P.
At low temperature, as T approaches 0 K, both C_V and C_P approach zero. Fig. 1.1 shows the way in which they vary with temperature.

The enthalpy change between temperature T_1 and T_2 is given by integrating Eq. 1.6 to give

$$\Delta H = \int_{T_1}^{T_2} C_P \mathrm{d}T \tag{1.8}$$

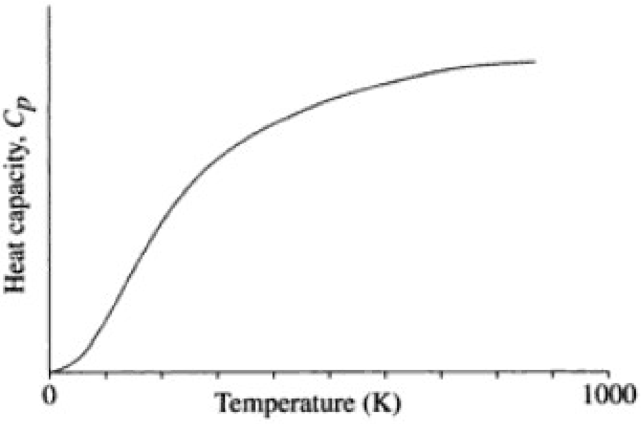

Figure 1.1: General form of the variation of C_P with temperature. Figure taken from Putnis (1992).

and the overall enthalpy at any temperature T_1 is

$$H = H_0 + \int_0^{T_1} C_P \mathrm{d}T \tag{1.9}$$

where H_0 includes the enthalpy due to the potential energy of the crystal at 0 K as well as the zero point vibrational energy. The integral includes the kinetic energy contribution up to temperature T_1 plus changes in the potential energy due to expansion and tilting of bonds.

When a phase transition occurs, there is a change in the enthalpy ΔH. If the enthalpy is reduced in the reaction, ΔH is negative and the process is termed *exothermic*, *i.e.* heat is evolved; when ΔH is positive heat is absorbed and the process is called *endothermic*.

1.1.2 Entropy

When a mineral undergoes a structural phase transition, it modifies its state of order and exchanges heat with its surroundings for compensation. A measure of change in the state of order in a mineral is given by the *entropy*, S, which overall change is defined as the sum of the entropy change in the mineral and the entropy change in the surroundings, *i.e.*

$$\mathrm{d}S = \mathrm{d}S_{system} + \mathrm{d}S_{surr}. \tag{1.10}$$

For a reversible reaction, $\mathrm{d}S = 0$, but for any natural reaction proceeding towards equilibrium, $\mathrm{d}S > 0$, according to the Second Law of Thermodynamics. This means that, if a mineral becomes more ordered in a transformation process and hence reduces its entropy, the heat liberated must increase the entropy of the surroundings by a greater amount, to satisfy the second law.

The entropy change is determined by

$$\mathrm{d}S > \frac{\mathrm{d}Q}{T}. \tag{1.11}$$

In a system free to exchange heat with its surroundings, it holds that

$$\mathrm{d}S > \frac{\mathrm{d}H}{T}, \tag{1.12}$$

noting that at constant pressure $\mathrm{d}Q = \mathrm{d}H$.

Thus, the criterion for a mineral transformation or reaction to proceed is that

$$\mathrm{d}H - T\mathrm{d}S < 0. \tag{1.13}$$

If $\mathrm{d}H - T\mathrm{d}S = 0$, no further change is possible, *i.e.* the system is at equilibrium. If $\mathrm{d}H - T\mathrm{d}S > 0$, the reaction will not proceed.

1.1.2.1 Configurational entropy

In the statistical definition, according to Boltzmann, the entropy of a system in a given state is related to the probability of the existence of that state, ω. In this context, the "state" refers to a particular distribution of atoms and their vibrational energy levels. Mathematically, this is expressed as

$$S = k\ln(\omega) \tag{1.14}$$

where k is Boltzmann's constant. The probability ω is related to the state of disorder or randomness in the structure, which may be expressed statistically by the number of different ways in which atoms can arrange themselves in that state:

$$\omega = \frac{N!}{(x_A N)!(x_B N)!}, \tag{1.15}$$

where x_A and x_B are the atomic fractions of A and B atoms, respectively, and $x_A N$ and $x_B N$ are the numbers of atoms of A and B, distributed over N sites in a hypothetical simple cubic lattice. When the number of sites is very large, as is the case in a mole of a mineral, the Stirling's approximation can be used:

$$\ln N! = N\ln N - N. \tag{1.16}$$

Thus, from Eqs. 1.31 and 1.16

$$S = -Nk(x_A\ln x_A + x_B\ln x_B). \tag{1.17}$$

For a mole of sites, N is Avogadro's number and Nk = R, the gas constant. By taking N as Avogadro's number, it is considered only one structural site over which substitution of A and B occurs, but, in a complex mineral structure, there may be more than one site per formula unit over which disorder can occur. So, the general form of the entropy is

$$S = -n\mathrm{R}(x_A \ln x_A + x_B \ln x_B), \tag{1.18}$$

where n is the number of sites on which mixing occurs. Since x_A and x_B are both fractions that range between 0 and 1, S is always positive.

In general, when the entropy is due to atomic disorder, it is known as configurational entropy and is calculated using Eq. 1.18, which is called *entropy of mixing*.

1.1.2.2 Vibrational entropy

Another important source of entropy in a crystal is due to disorder associated with the lattice vibrations. The vibrational entropy arises by considering the number of ways of distributing the phonons (whose number increases when the amplitude of atomic vibrations increases) over the vibrational energy levels which exist in a crystal. This is very much more difficult to calculate than configurational entropies because the number of energy levels is not as simply defined as the number of crystallographic sites. However, the vibrational entropy may be calculated from the heat capacity, which defines the way in which an increase in the heat content in the crystal is related to an increase in temperature. This depends on the way in which the extra phonons are distributed over the available vibrational energy levels.

The relation between the vibrational entropy and the heat capacity C_P can be seen by considering that for a reversible process $\mathrm{d}S = \frac{\mathrm{d}Q}{T}$. From Eq. 1.6, it follows that $\frac{\mathrm{d}S}{\mathrm{d}T} = \frac{C_P}{T}$ and hence

$$S = \int \frac{C_P}{T} \mathrm{d}T. \tag{1.19}$$

At any temperature T_1, the entropy is given by

$$S = S_0 + \int_0^{T_1} \frac{C_P}{T} \mathrm{d}T, \tag{1.20}$$

where S_0 is the entropy at 0 K.

A simple statement of the Third Law of Thermodynamics is that at 0 K the entropy of a perfect crystal is zero, all atoms occupying the ground state, hence $S_0 = 0$. However, if a material has a disordered atomic distribution at a higher temperature, rapid cooling may freeze in this state, even down to 0 K, where the thermodynamically favoured state would be the one with the minimum internal energy, *i.e.* complete order. Such residual disorder and the associated *zero-point entropy*, as it is called, is due to the fact that at low temperatures the rate of atomic diffusion becomes vanishingly small.

1.1.3 Free energy

In Subsection 1.1.2, it has been found that a reaction can proceed only when Eq. 1.13 is satisfied. The quantity $\mathrm{d}H - T\mathrm{d}S$, therefore, can be used to define a criterion for the direction of change in a mineral reaction and a definition of equilibrium. This quantity is known as the change in the *Gibbs free energy*, $\mathrm{d}G$, for the system. Thus

$$\begin{aligned} &\mathrm{d}G = \mathrm{d}H - T\mathrm{d}S, \\ \text{or} \quad &G = H - TS. \end{aligned} \tag{1.21}$$

The equivalent criterion when a system is considered at constant volume rather than at constant pressure would be that $(\mathrm{d}U - T\mathrm{d}S)$. The equivalent free energy is known as the *Helmholtz free energy*, $\mathrm{d}F$, of the system. Thus, at constant volume

$$F = U - TS. \tag{1.22}$$

Since constant pressure experiments with solids are far easier to perform than constant volume experiments, the Gibbs free energy is much more useful than the Helmholtz free energy.

In Eq. 1.68, the definition of enthalpy $H = U + PV$ can be used, leading to

$$G = U + PV - TS. \tag{1.23}$$

Differentiating gives

$$\mathrm{d}G = \mathrm{d}U + P\mathrm{d}V - T\mathrm{d}S - S\mathrm{d}T. \tag{1.24}$$

From the first law ($\mathrm{d}U = \mathrm{d}Q - P\mathrm{d}V$) and for a reversible process ($\mathrm{d}Q = T\mathrm{d}S$), it follows that, at equilibrium,

$$\mathrm{d}G = V\mathrm{d}P - S\mathrm{d}T. \tag{1.25}$$

Therefore, at constant pressure

$$\left(\frac{\partial G}{\partial T}\right)_P = -S \tag{1.26}$$

and at constant temperature

$$\left(\frac{\partial G}{\partial P}\right)_T = V. \tag{1.27}$$

1.1.4 Thermodynamic classification of phase transitions

Phase transitions occur in response to a change in the external environment. At the equilibrium temperature (or pressure) at which the transition theoretically takes place, the Gibbs free energies of the two polymorphs are equal and hence there is no discontinuity in the free energy G on passing from one structure to another. However, in *first-order phase transition* the first derivatives of the free energy $\frac{\partial G}{\partial T}$ and $\frac{\partial G}{\partial P}$ are discontinuous. Since $\frac{\partial G}{\partial T} = -S$ and $\frac{\partial G}{\partial P} = V$, first-order phase transitions are characterized by discontinuous changes in entropy and volume at the critical temperature, as well as in enthalpy. At the transformation T, the specific heat becomes infinite, since the addition (or subtraction in an exothermic change) of heat serves to convert more of one phase into another, rather than to change the temperature.

In *second-order phase transition* the first derivatives of the free energy are continuous, but the second derivatives $\frac{\partial^2 G}{\partial T^2}$ and $\frac{\partial^2 G}{\partial P^2}$ are discontinuous. Since

$$\frac{\partial^2 G}{\partial T^2} = -\frac{\partial S}{\partial T} = -\frac{C_P}{T} \tag{1.28}$$

$$\text{and} \quad \frac{\partial^2 G}{\partial P^2} = -V\beta; \quad \frac{\partial^2 G}{\partial T \partial P} = V\alpha \tag{1.29}$$

the discontinuities occur in the specific heat capacity C_P, in the compressibility β and in the thermal expansion α. Fig. 1.2 shows these changes in thermodynamic properties through first- and second-order phase transitions.

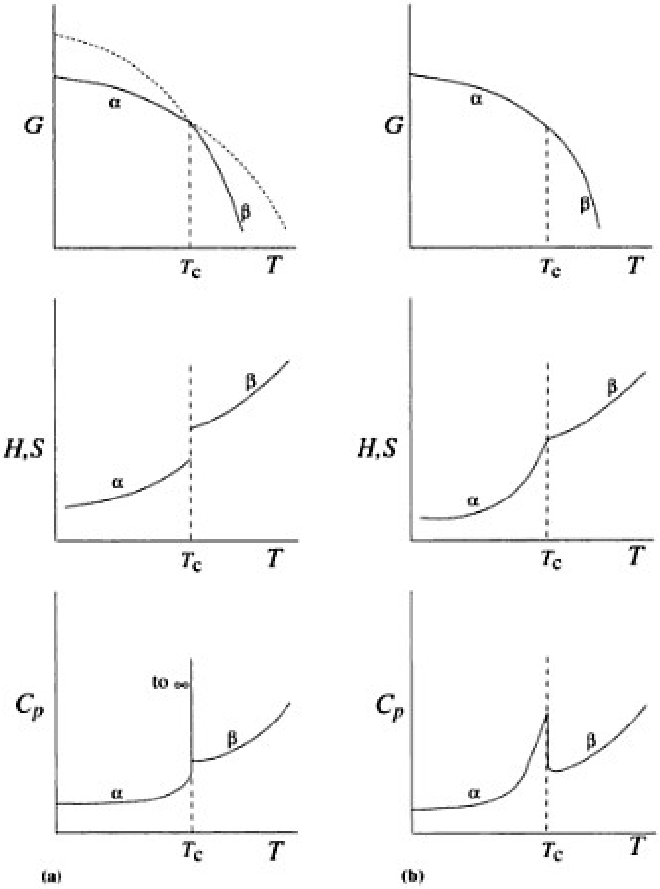

Figure 1.2: Changes in the thermodynamic properties, free energy (G), enthalpy (H), entropy (S) and specific heat (C_P) as functions of temperature, for a (a) first- and (b) second-order transformation between two phases α and β. Figure taken from Putnis (1992).

Although this classification appears to be quite clearcut, the two mentioned categories should be regarded as extreme cases. Indeed, even first-order transitions show continuous changes before T_c is reached (the so-called "premonitory" effects), and the discontinuity at T_c may be quite small. Moreover, in the second-order transformations most of the structural change takes place before T_c is reached, and T_c represents the temperature at which changes are effectively complete. There are cases where transitions are referred to as "nearly second-order" and the changeover from first- to second-order is difficult to define.

1.2 Kinetics

Kinetics is the branch of chemistry concerned with measuring and studying the rates of reactions, *i.e.* the speed of changes in the concentration of reactants in a chemical reaction. It deals with investigations on how different experimental conditions can influence the speed of a reaction and yields information about the reaction's mechanism and transition states, as well as the construction of mathematical models that can describe the characteristics of the reaction.

Indeed, although a negative free energy change is a necessary prerequisite for a mineral transformation to occur (as seen in the previous Section), it does not garantee that it will do so at any measurable rate. The rate depends on the *mechanism* of the reactions involved and may bear no relation to the magnitude of the free energy reduction which drives the transformation. This is illustrated by the effect of catalysts on chemical reactions: they do not change the free energy of the phases, but provide a faster mechanism. The commonplace observation that minerals stable at high temperatures and/or pressures are preserved outside their stability fields is due to the fact that atomic mechanisms of bond-breaking and diffusion may be very slow.

If kinetics are determined by factors other than ΔG, one must consider the states through which a system passes during the transformation. Since equilibrium thermodynamics does not describe these states, additional concepts are necessary in order to deal with reaction rates. This Section will illustrate some basic ideas of kinetic theory.

1.2.1 The activated state and the associated thermodynamic functions

At equilibrium, when $\Delta G = 0$, no transformation can take place. Some overstepping is always required to provide the free energy reduction, and this means that the pathway from the initial state to the final state (which are both in equilibrium) must pass through a maximum of free energy. This intermediate configuration is known as *activated state* and Fig. 1.3 points out exactly this concept.

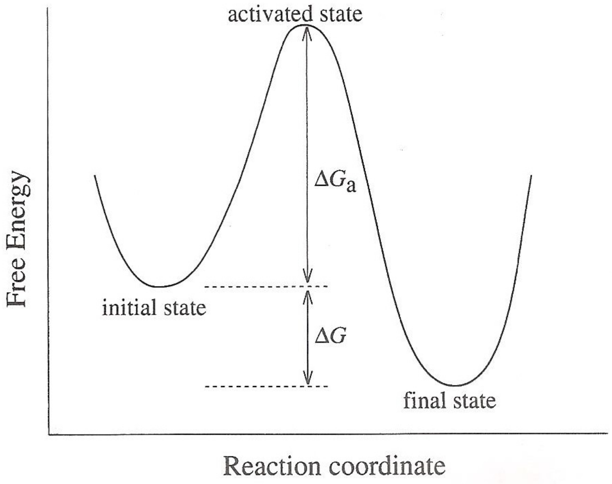

Figure 1.3: The free energy curve, showing the pathway from an initial state to a final state passing through an intermediate activated state. The "reaction coordinate" is any variable that defines the progress along the reaction path. Figure taken from Putnis (1992).

As consequence of what just claimed, the free energy of activation ΔG_a depends on the reaction pathway and, in heterogeneous reactions, is indipendent of the thermodynamics of the initial and final states. The pathway with the lowest ΔG_a will be the one taken. A necessary condition for a transformation to take place at a measurable rate is that sufficient atoms have enough energy to achieve the transition state. This energy is supplied by thermal fluctuations: at all temperatures, even at 0 K, indeed, atoms are in motions and collisions between them produce wide variations in the energy of individual atoms, some of which reach energies greatly in excess of the mean. This concept of an activation energy barrier qualitatively explains some feactures, characterizing mineral reactions:

1. the persistence of metastable states, due to ΔG_a being very large compared to the mean free energy;

2. the independence of the reaction rate on the driving force;

3. the effect of catalysts which provide a reaction path with lower ΔG_a;

4. the slow rate of many transformations, due to the fact that only a small number of the available atoms have sufficient free energy to overcome the activation energy barrier.

In a formal way, the Gibbs free energy of activation G_a can be defined as following

$$G_a = H_a - TS_a, \tag{1.30}$$

where the subscripts refer to the activated state.
For most solid state reactions at low pressures, the volume change is small and hence the change in enthalpy ΔH_a is approximated to the internal energy of the activated state. In such cases and commonly, the term "*activation energy*" is used as synonym with activation enthalpy, but it must not be confused with the free energy of activation. The activation energy is the difference between the internal energy (or enthalpy) of the transition state and that of the initial state. Its curve is very similar to the one for free energy (Fig. 1.3), except that the overall enthalpy change ΔH may be positive (endothermic process) or negative (exothermic reaction).
Similarly, the entropy of activation ΔS_a is defined as the difference between the entropy of the activated state and that of the initial state, and can be expressed by

$$\Delta S_a = \mathrm{R}\ln\left(\frac{\omega_a}{\omega_i}\right), \tag{1.31}$$

where ω_a and ω_i are the numbers of complexions associated with the activated and initial state, respectively. "Complexions" means all of the different ways in which the atoms can be spatially distributed and how their thermal, electronic and other forms of energy are distributed over the permitted energy levels. The entropy change, therefore, includes changes in the configurational, electronic and vibrational entropy.

A large number of reaction paths results in a large S_a and hence, from Eq. 1.30, a lower free energy of activation. Therefore, in general reactions between two states with a larger number of reaction pathways are faster. In view of the requirement that an atom must acquire sufficient energy to overcome the activation energy barrier, it is useful and necessary to determine how the thermal energy is distributed among the particles in the system. In any system at equilibrium, the fraction f of the total particles having a thermal energy not less than ΔH_a is given by Boltzmann distribution:

$$f = \exp\Big(\frac{-\Delta H_a}{\mathrm{R}T}\Big), \tag{1.32}$$

where ΔH_a refers to the activation energy per mole.

1.2.2 Rate and Arrhenius equation

For a process which involves only one basic atomic step, characterized by a unique activation energy ΔH_a, for example the diffusion of atoms from one site to another, the reaction rate is proportional to:

1. the frequency with which atoms attempt to jump from one site to the next, *i.e.* the vibration frequency ν;
2. the fraction of atoms with enough energy to surmount the activation energy barrier, *i.e.* Eq. 1.32;
3. the probability p that the atom which has the required energy satisfies some geometrical conditions, *i.e.* it is jumping the right direction. For example, for NaCl structure $p = 1/6$, since each atomic site is surrounded by 6 neighbouring sites; for more complex structures p is less; for atomic diffusion involving the co-operative movement of several atoms p may be very small.

This can be written in a formal way:

$$\text{Rate} \propto p \cdot \nu \cdot \exp\Big(\frac{-\Delta H_a}{\mathrm{R}T}\Big) = \frac{\mathrm{d}\alpha}{\mathrm{d}t}, \tag{1.33}$$

where $\alpha(t)$ is the ratio of the number of atoms/unit volume in the final state at time t to the number of atoms per unit volume in the initial state at time $t = 0$, *i.e.* the fraction of atoms which have diffused or transformed.
p is related to the entropy of activation as following:

$$p = \frac{\omega_a}{\omega_i}, \tag{1.34}$$

that is the ratio of the number of complexions associated with the transition state to that associated with the initial state.
From Eqs. 1.31 and 1.30

$$p = \exp\Big(\frac{\Delta S_a}{\mathrm{R}}\Big), \tag{1.35}$$

$$\text{and therefore} \quad \frac{\mathrm{d}\alpha}{\mathrm{d}t} = \nu \cdot \exp\Big(\frac{\Delta S_a}{\mathrm{R}}\Big) \cdot \exp\Big(\frac{-\Delta H_a}{\mathrm{R}T}\Big) = \nu \cdot \exp\Big(\frac{-\Delta G_a}{\mathrm{R}T}\Big). \tag{1.36}$$

More commonly, Eq. 1.36 can be written

$$\begin{aligned} &\frac{\mathrm{d}\alpha}{\mathrm{d}t} = A \cdot \exp\Big(\frac{-\Delta H_a}{\mathrm{R}T}\Big) \\ \text{or} \quad &\frac{\mathrm{d}\alpha}{\mathrm{d}t} = A \cdot \exp\Big(\frac{-E_a}{\mathrm{R}T}\Big), \end{aligned} \tag{1.37}$$

where the pre-exponential factor A, which contains the entropy of activation term, is known as the *frequency factor*, while E_a is an empirical activation energy (note that Δ prefix has been removed merely for convenience). Eq. 1.37 is known as the *Arrhenius equation*, and, if both A and E_a are indipendent of temperature, it can be linearized as following:

$$\ln\frac{\mathrm{d}\alpha}{\mathrm{d}t} = \ln A - \frac{E_a}{\mathrm{R}T}. \tag{1.38}$$

A plot of $\ln\frac{\mathrm{d}\alpha}{\mathrm{d}t}$ against $\frac{1}{T}$ is termed *Arrhenius plot* and represents a straight line with gradient $\frac{E_a}{\mathrm{R}}$ and intercept on the rate axis of $\ln A$. The magnitude of E_a describes the temperature dependence of the reaction rate, while the pre-exponential A determines the absolute reaction rate. Considering that the reaction rate is controlled by an exponential function, it is not surprising that metastable states are so commonly found during mineral transformations. Values of apparent activation energy encountered in solid state processes in minerals usually range between 200 and 400 kJmol^{-1}.

1.2.3 Rate equations and the Avrami model

The rate of a heterogeneous reaction at fixed temperature, pressure, etc. is a function of time, due to the fact that reaction rates depend on the concentration of reactants and these change continuously as the reaction proceeds. This problem is overcome by expressing the experimental results in terms of a *rate equation*, which represents the rate as a function of the concentration or fraction of the transformation completed. Since

$$\text{Rate} = k \cdot \mathrm{f}(C), \tag{1.39}$$

being k the *rate constant* and C the concentration of reactants, it can be found that

$$\frac{\mathrm{d}\alpha}{\mathrm{d}t} = k \cdot \mathrm{f}(\alpha), \tag{1.40}$$

where α is the fraction transformed. $\mathrm{f}(\alpha)$ is some function of α.
Experimentally the measured variable is α, not $\frac{\mathrm{d}\alpha}{\mathrm{d}t}$, so it is more convenient to put this equation in the following form (obtained after integration):

$$\mathrm{g}(\alpha) = kt, \tag{1.41}$$

where $\mathrm{g}(\alpha)$ is a further function of α. Eq. 1.41 is known as an *integrated rate equation*. The function $\mathrm{g}(\alpha)$ can now be determined empirically, by finding functions which describe the variation of α with time. When an

equation which fits the observed data is found, the rate constant k can be obtained.
Rate equations are not always defined strictly in accordance with Eq. 1.40 and in many cases the usage can be quite loose.

Empirically, it is found that the isothermal kinetics of a wide range of mineral reactions can be described by an equation of the general form

$$\frac{\mathrm{d}\alpha}{\mathrm{d}t} = k^n t^{n-1}(1-\alpha), \tag{1.42}$$

where n is a constant which depends on the mechanism. Separating the variables and integrating gives

$$\int \frac{\mathrm{d}\alpha}{1-\alpha} = \int k^n t^{n-1} \mathrm{d}t$$

$$\text{and} \quad \ln \frac{1}{1-\alpha} = (kt)^n, \tag{1.43}$$

where the term $\frac{1}{n}$ has been incorporated into the constant. This can also be written as following

$$\alpha = 1 - \exp(-kt)^n, \tag{1.44}$$

which is known as the *Avrami equation*. It has a sigmoidal form, the reaction rate being small at the beginning, then increasing to a maximum, and finally decreasing to zero as the reaction goes to completion. The rate constant k has dimensions time^{-1}.
To extract values of the rate constant from Eq. 1.44, the usual approach is to linearize the equation:

$$\begin{aligned} &1-\alpha = \exp(-k^n t^n) \\ &\ln(1-\alpha) = -k^n t^n \\ &-\ln(\ln(1-\alpha)) = n\ln(k) + n\ln(t). \end{aligned} \tag{1.45}$$

Thus, a reaction whose kinetics conform to this Avrami equation gives a straight line when $-\ln(\ln(1-\alpha))$ is plotted against $\ln(t)$. The value of n, which is used as an empirical parameter necessary to compare reaction mechanisms, is derived from the slope of the line. The intercept on the y-axis gives the value of $n\ln k$ from which the rate constant k is determined.
The value of apparent activation energy E_a can then be obtained from the Arrhenius plot of $\ln k$ against $\frac{1}{T}$. The disadvantage of this method is that it is not possible to ascertain whether the apparent activation energy changes during the course of an isothermal transformation. Moreover, the determined value of k depends on the empirical selection of the function $\mathrm{f}(\alpha)$ in the rate equation 1.40. The empirical activation energy determined in this way may depend, therefore, on the choice of rate equation. Indeed, a number of different forms of the rate equation may fit the data equally well, but result in different values, so it is essential to specify clearly the rate equation used in the determination.

1.3 Landau theory

By the determination of thermodynamical properties it is possible to evaluate the effect of a structural phase transition on the overall free energy. One common method to doing so is to measure the enthalpy and entropy changes by some calorimetric technique. Calculations of the thermodynamics of structural changes involve microscopic models, which attempt to describe the variation in free energy from interaction energies between atoms.

A very different approach to determining free energy changes is based on Landau theory. It relates the variations in macroscopic properties, such as strain, optical birefringence, average site occupancy, etc., to the changes in thermodynamic properties: if the mathematical form of the relationship between the change in free energy and the change in some macroscopic property is known, easily measurable properties can provide quantitative thermodynamic data.

The central concept of Landau theory is the *order parameter*, which describes the course of a phase transition. In particular, the order parameter, usually symbolised by Q, is associated with the change in some macroscopic property through the phase transition and is scaled so that it is assigned a value of 0 in the high temperature (HT) form and 1 in the low temperature form. Therefore, Q defines the deviation of the low temperature phase from that of the high temperature phase and the temperature evolution of the order parameter describes the thermodynamic character of the phase transition.

The measured physical property is not necessarily directly proportional to Q, but can scale with Q^2, for example. The definition of the Landau order parameter has a rigorous theoretical basis in terms of the symmetry relations between the high and low temperature forms, and standard tables list the correct form of the order parameter and its relationship to certain physical properties for a given change in symmetry.

Landau theory describes those phase transitions in which low temperature form is derived from the high temperature modification by a loss of some of the symmetry elements, which implies that the basic structures of the two forms are topologically similar. The low temperature form may be a distorted version of the high temperature one, or it may have an ordered cation distribution while the high temperature modification is disordered. Formally, the symmetry of the low temperature phase must be a subgroup of the high temperature symmetry; this symmerty relationship allows Q to be mathematically related to the thermodynamic measured quantities.

1.3.1 The Landau free energy

Once the correlation between the order parameter and the estimated property is defined, the next step is to describe how the excess free energy is related to Q. The excess free energy ΔG (which, for convenience, is hereafter shortened by G) is the excess over that which the high form would have if the phase transition did not occur. Landau proposed that the excess free energy due to a phase transition can be described as a polynomial expansion of the order parameter Q:

$$G = aQ + \frac{1}{2}AQ^2 + \frac{1}{3}bQ^3 + \frac{1}{4}BQ^4 + ..., \tag{1.46}$$

where a, A, b, B, etc., are coefficients which may or may not depend on material properties or on extensive variables.

The equilibrium behaviour of Q through a phase transition is determined by minimising G with respect to Q and therefore:

$$\frac{\mathrm{d}G}{\mathrm{d}Q} = 0 \quad \text{and} \quad \frac{\mathrm{d}^2G}{\mathrm{d}Q^2} > 0. \tag{1.47}$$

In the high symmetry form which is stable above some critical temperature T_c, the order parameter $Q = 0$. The equilibrium criteria expressed in Eq. 1.47 can only be satisfied if the linear term is absent and A is positive. If A is negative, Q must be bigger than 0 and the low temperature form becomes stable. Hence, as the temperature falls, the sign of A crosses over from positive to negative at $T = T_c$. This temperature dependence of A is expressed as a linear function of T:

$$A = a(T - T_c) \tag{1.48}$$

where a is another constant. Coefficients b, B, c, etc. are assumed to be indipendent of T.
From the considerations above, Eq. 1.46 becomes

$$G = \frac{1}{2}a(T - T_c)Q^2 + \frac{1}{3}bQ^3 + \frac{1}{4}BQ^4 + ... \tag{1.49}$$

The form of this free energy expansion is also determined by the nature of the symmetry change involved in the transition. If a phase transformation is thermodynamically second-order, Q varies continuously between 0 and 1 and this implies that, for the condition expressed in Eq. 1.47 to be satified, all the odd-order coefficients (b, c, etc.) must be zero. If odd-order coefficient are present, the transition must be discontinuous, *i.e.* thermodinamically first-order. The symmetry changes which allow odd-order terms in the Landau free energy expansion are tabulated in standard texts (*e.g.* Carpenter, 1992.).
When odd-order terms are absent, the excess free energy reduces to

$$G = \frac{1}{2}a(T - T_c)Q^2 + \frac{1}{4}BQ^4 + \frac{1}{6}CQ^6 + ... \tag{1.50}$$

Normally two or three terms of this expansion are adequate to describe the free energy changes from experimentally measured values of Q.
Although this expression allows Q to vary continuously between 0 and 1, it does not preclude the possibility of a discontinuity, and this depends on the value of B:

1. when B is positive and the sixth-order term is negligible, the phase transition is second-order.
   At equilibrium, the variation of Q with temperature is

   $$\frac{\mathrm{d}G}{\mathrm{d}Q} = a(T - T_c)Q + BQ^3 = 0 \tag{1.51}$$

   $$\text{and} \quad Q = \left(\frac{a}{b}(T_c - T)\right)^{\frac{1}{2}}. \tag{1.52}$$

By definition $Q = 1$ at $T = 0$, hence

$$\frac{a}{B} = \frac{1}{T_c}$$
$$\text{and} \quad Q = \left(\frac{(T_c - T)}{T_c}\right)^{\frac{1}{2}}. \tag{1.53}$$

The variation of Q is shown in Fig. 1.4 a.

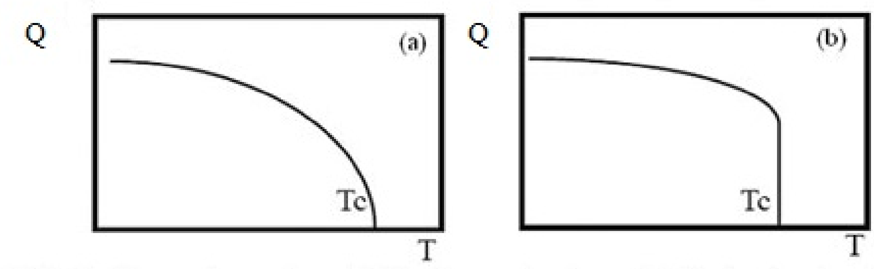

Figure 1.4: The variation of the order parameter Q with increasing temperature for a second-order (a) and a first-order (b) phase transition. In the latter Q has a discontinuity at $T = T_c$. Above T_c the order parameter is zero. Figure taken from Pandu (2014).

Substituting Eq. 1.53 in Eq. 1.50 and neglecting the sixth-order term, the temperature dependence for the excess free energy can be obtained:

$$G = -\frac{a^2}{4B}(T - T_c)^2. \tag{1.54}$$

Fig. 1.5 reports this dependence as function of the order parameter: at temperatures below T_c a continuous free energy pathway exists to the minimum value, which moves to larger values of Q as temperature falls.

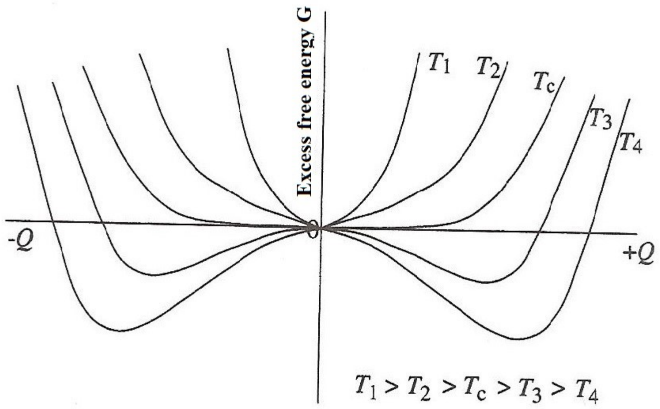

Figure 1.5: The excess free energy G as a function of the order parameter Q for a second-order phase transition. Above T_c the free energy increases for any non-zero value of Q, while below T_c a continuous free energy pathway leads to the free energy minimum. Figure taken from Putnis (1992).

2. when B is negative, the sixth-order term is required, in order to obtain a free energy minimum in the low temperature phase when $Q > 0$, and both a and C must be positive. The phase transition is first-order.
   The equilibrium condition is

$$\frac{\mathrm{d}G}{\mathrm{d}Q} = a(T - T_c)Q + BQ^3 + CQ^5 = 0, \tag{1.55}$$

   from which

$$\begin{aligned} & Q^2 = \frac{-B \pm (B^2 - 4aC(T - T_c))^{\frac{1}{2}}}{2C} \\ & \text{or} \quad Q = 0. \end{aligned} \tag{1.56}$$

   This expression describes a discontinuity in Q as a function of T and Fig. 1.4 b shows the same relationship. The temperature dependence of the free energy also shows this jump in the order parameter from $Q = 0$ to $Q = Q_0$ at the equilibrium transformation temperature T_{tr}, which is higher than T_c (see Fig. 1.6) and which is given by

$$T_{tr} = T_c + \frac{3B^2}{16aC}. \tag{1.57}$$

   On the other hand, Q_0 is defined as following

$$Q_0 = \pm\left(\frac{-4a(T_{tr} - T_c)}{B}\right)^{\frac{1}{2}}. \tag{1.58}$$

   The size of the discontinuity Q_0 indicates how strongly first-order the transition is: the more negative the value of B, the larger the first-order step and the greater the difference between T_{tr} and T_c.

3. when $B = 0$, the phase transition is *tricritical* and is the case which corresponds to the boundary between a first-order transition (B negative) and a second-order transition (B positive). The sixth-order term is required with C positive, in order to produce a minimum in the low temperature form.
   The excess free energy at equilibrium is given by

$$G = \frac{1}{2}a(T - T_c)Q^2 + \frac{1}{6}CQ^6. \tag{1.59}$$

   Repeating the minimisation procedure as above gives the equilibrium variation of Q with temperature as

$$Q = \frac{a}{C}(T_c - T)^{\frac{1}{4}} \tag{1.60}$$

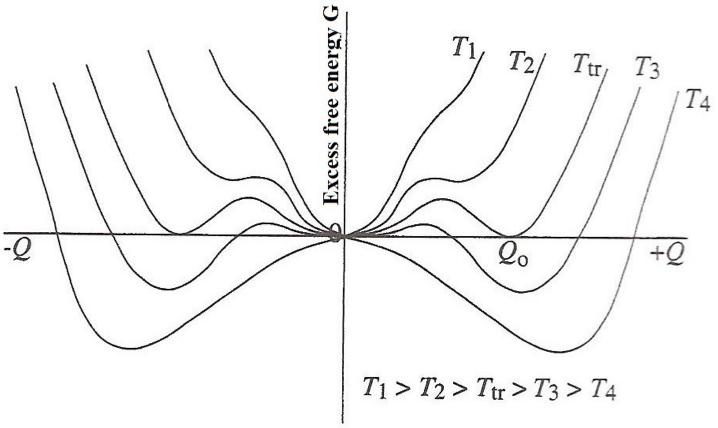

Figure 1.6: The excess free energy G as a function of the order parameter Q for a first-order phase transition. At the transition temperature $T = T_{tr}$ there is a jump in the order parameter, from $Q = 0$ to $Q = Q_0$, accompanied by a free energy barrier. At sufficiently low temperatures continuous pathways towards equilibrium become available. Figure taken from Putnis (1992).

$$\text{and} \quad T_c = \frac{C}{a}. \tag{1.61}$$

Therefore

$$Q = \left(\frac{T_c - T}{T_c}\right)^{\frac{1}{4}} \tag{1.62}$$

The variation of Q with T is continuous between 0 and 1, in a similar way to a second-order transition. Indeed, one can derive the general relationship between Q and T:

$$Q = \left(\frac{T_c - T}{T_c}\right)^{\beta}, \tag{1.63}$$

where β is termed the *critical exponent* and describes the variation of the order parameter with temperature for continuous transformations. For the two ideal cases considered here, $\beta = \frac{1}{2}$ refers to a second-order transition and $\beta = \frac{1}{4}$ to a tricritical one.

In all the three cases of transitions, it is easy to determine the excess enthalpy, entropy and heat capacity, starting from the definition of the free energy change and its coefficients. However, these concepts are not here reported, as they are not relevant for the aim of the present thesis.

1.3.2 The effect of spontaneous strain

During a phase transition there are several different contributions to the free energy change, all of which are incorporated in the Landau coefficients. Therefore, the effect of pressure, the volume change, the variation in composition, etc., as well as of strain can be separate and independently evaluated by including them in the coefficients. For the current thesis, the case of strain is the interesting one, thus the next theretical part will concern its related concepts.

1.3.2.1 Fundamentals on elasticity theory

Robert Hooke proposed first the relationship between a stress applied to a spring and its response, by formulating the fundamental law of elasticity:

$$F = kx, \tag{1.64}$$

where F is the applied load, x is the resultant extension of the spring and k is the spring constant.
This equation, which is known as *Hooke's law*, can be generalized for any elastic material undergoing small distortions due to stress:

$$\sigma = Ee, \tag{1.65}$$

where σ is the applied stress, e is strain and E is the Young's (or elastic) modulus. E describes how resistant the material is to the applied stress, and thus is a constant which varies depending on the material: if a material does not stretch, compress or bend, in response to the applied stress, E is high, and vice versa.
This equation relates to applied loads and resultant strains which develop through only one direction. In order to extend the concept in the three-dimension space, Voigt notation can be used:

$$\sigma_i = C_{ik}e_k, \tag{1.66}$$

where σ_i and e_k are stress and strain tensors, respectively (represented by 3×3 matrices), and C_{ik} is the elastic constant tensor (a 6 × 6 matrix).

As materials used in industrial applications are usually polycristalline aggregates of the same composition, instead of single crystals, it is more useful to consider the behaviour of the material as a whole. This behaviour can be described by the *bulk modulus* K, which measures the resistance to uniform compression, and the *shear modulus* G, which defines the resistance to shear stress:

$$K = \frac{1}{3}(C_{11} + 2C_{12}) \tag{1.67}$$

$$G = C_{44} = \frac{1}{2}(C_{11} - C_{12}). \tag{1.68}$$

C_{11} and C_{44} are the only two independent elastic constants for bulk isotropic polycrystals; moreover, together with C_{12}, they are not the single crystal elastic constants, but are polycrystalline values.

1.3.2.2 Application of Landau theory to elastic anomalies

As already mentioned, during a phase transition different physical properties can change, and the result is a change also in the shape of the unit cell. This variation is expressed in terms of the *spontaneous strain*, *e*, which is defined in terms of the lattice parameters and always measured relative to an undistorted cell at the same temperature. If the transition yields to a cubic-to-tetragonal change in the structure, for example, the spontaneous strain can be expressed as

$$e = \frac{a_1 - a_0}{a_0}, \tag{1.69}$$

where a_0 is the cubic lattice parameter, and a_1 and c_1 are those of the tetragonal cell. Therefore, both the form of the spontaneous strain and its relationship with Q are dependent on the symmetry change involved in the transition.

In particular, if there is no change in translational symmetry of the lattice and the unit cell merely changes its shape, no extra points appear in the reciprocal lattice, thus the transition does not involve variations in the boundaries of the Brillouin zone. Transformations of this type are called *zone centre transitions*, and e usually scales with Q. On the other hand, if there is a change in the reciprocal lattice as would occur if the translational symmetry changed, the boundaries of the Brillouin zone are affected. This is termed a *zone boundary transition*, and e is generally proportional to Q^2.

When the change in the order parameter induces a spontaneous strain, the two are coupled together. Therefore, the effect of strain and the coupling between order parameter and strain can be included in the Landau expansion, which becomes

$$G = G_Q + G_{elastic} + G_{coupling}, \tag{1.70}$$

where G_Q is the excess free energy described until here, due to the order parameter alone and expressed by Eq. 1.50, while $G_{elastic}$ and $G_{coupling}$ are defined below:

- $G_{elastic}$ is the elastic potential energy which defines the work done against the bare elastic constants, C^0_{ik}, and does not include the effects of the transition. It is calculated directly from Hooke's low:

$$G_{elastic} = \frac{1}{2}\sum_{i,k} C^0_{ik} e_i e_k. \tag{1.71}$$

- $G_{coupling}$ is the energy due to coupling between strains and the order parameter. Indeed, strain is usually a secondary driving parameter and another mechanism which drive the transition is present, *e.g.* tilting of octahedra or polarization. In such cases, the term $G_{coupling}$ is necessary in the Landau equation:

$$G_{coupling} = \sum_{i,m,n} \lambda_{i,m,n} e_i^m Q^n, \tag{1.72}$$

where $\lambda_{i,m,n}$ are the coupling coefficients which describe how strains e_i interact with the order parameter;

m and n values tipically range between 1 and 3, while i and k between 1 and 6.
The magnitude of the coupling coefficients establishs the magnitude of the elastic anomalies, which means that the way in which the coupling between the order parameter and strain is described in the free energy expansion depends on the symmetry change associated with the transition. The simplest case is when the transformation does not involve any variation in the translational symmetry (*i.e.* zone centre transition): the order parameter is linearly coupled to strain, hence only the terms of $G_{coupling}$ with eQ are present in the Landau expression and the coupling is termed *bilinear*. On the contrary, when the transition is zone boundary, the coupling is *quadratic*, thus involves terms built up using eQ^2 (the term eQ is negligible). Finally, when the transformations combine zone boundary and zone centre transitions, the appropriate coupling terms include both eQ and eQ^2.

Substituting Eqs. 1.71, 1.72 and 1.50 in Eq. 1.70, one gets the expanded form of the total free energy change:

$$G = \frac{1}{2}a(T - T_c)Q^2 + \frac{1}{4}BQ^4 + \frac{1}{6}CQ^6 + \frac{1}{2}\sum_{i,k} C^0_{ik}e_i e_k + \sum_{i,m,n} \lambda_{i,m,n} e_i^m Q^n \tag{1.73}$$

From the study of the excess free energy, it is possible to calculate the elastic constants, which variations across a transformation are fingerprints of the type of transition. In particular, if a phase transition is described by order parameter coupled with strain, the most general approach used to determine the elastic constants from the free energy is the equation proposed by Slonczewski & Thomas (1970):

$$C_{ik} = \frac{\partial^2 G}{\partial e_i \partial e_k} - \sum_{i,k} \frac{\partial^2 G}{\partial e_i \partial Q} \cdot \left(\frac{\partial^2 G}{\partial Q^2}\right)^{-1} \cdot \frac{\partial^2 G}{\partial e_k \partial Q}. \tag{1.74}$$

When strain data are experimentally measured, one can calculate values for the elastic constants through Eq. 1.74 and, for a polycrystalline material, bulk and shear moduli can be derived applying Eqs. 1.67 and 1.68. Moreover, since elastic constants are highly sensitive to phase transformations, the calculated elastic constants can be compared with the experimentally measured values, in order to test the transition mechanism proposed by the Landau model: if there is correspondence, the model is accurate (Carpenter & Salje, 1998).

Part II

Traditional ceramics

Chapter 2

Silica polymorphs in industry

2.1 Introduction

2.1.1 Overview on silica transitions and structures

The phase relationships among the low pressure silica polymorphs first were sorted out by Fenner (1913). Fig. 2.1 represents the silica phase diagram that he proposed, and displays all the theoretical temperatures at which the trasitions occur at room pressure. This transformation sequence upon heating involves α-quartz, β-quartz (573 °C), β-tridymite (870 °C) and β-cristobalite (1470 °C), which melts at 1705 °C. Given that the formation of β-tridymite requires particular impurities to be present [Palmer, 1994], β-cristobalite can even appear at lower temperature. Cristobalite also develops at $T \leq 1000$ °C, from SiO_2 glass [Gupta & Jau-Ho, 1994]. Upon cooling, β-tridymite and β-cristobalite turn into their metastable α-phases at 114 and 270 °C, respectively, not being able to overcome the activation energy barrier to change into their stable silica phases. These transitions are fully reversible even at relatively quick temperature changes, just like the transition of α-quartz to β-quartz, as they are all displacive transformations.

At low pressures there are three groups of silica polymorphs, each of which has two closely related members: one low-temperature member, given by an α- or *low*-prefix, and one high-temperature member of the same name, with a β- or *high*-prefix. Table 2.1 lists some important information about the stability and the structure of all these modifications.

The basic structural element of silica is the $(SiO_4)^{4-}$ tetrahedron. Quartz consists of interconnected $(SiO_4)^{4-}$ tetrahedra that build up a rigid three-dimensional network. There are many possible ways of connecting $SiO_4{}^{4-}$ tetrahedra, different from that found in quartz, and realized in various other silica polymorphs. Since all of them consist of a three-dimensional $(SiO_4)^{4-}$ network, they are all classified as *network silicates*. What distinguishes the silica modifications is primarily the angle of the more flexible Si–O–Si bond that connects the tetrahedra. These values are reported in Table 2.1.

In quartz, $(SiO_4)^{4-}$ tetrahedra are arranged in virtual threefold helices that run parallel to the c-axis and wind around it either clockwise or counterclockwise. (Clockwise and counterclockwise corresponds to being right-handed and left-handed). A helix has no mirror symmetry, thus it is congruent with itself when rotated by 180°. This is in accordance with the fact that both ends of a quartz crystal show the same types of crystal faces. A very distinctive feature of quartz crystal structure is the presence of two kind of channels that run through the entire crystal parallel to the c-axis: two threefold helices produce a virtual sixfold helix which, in turn, forms the larger channel in its centre, but every single threefold helix forms itself the second type of channel, which is smaller than the previous mentioned. The sixfold helix and the threefold helices are of opposite handedness. Each

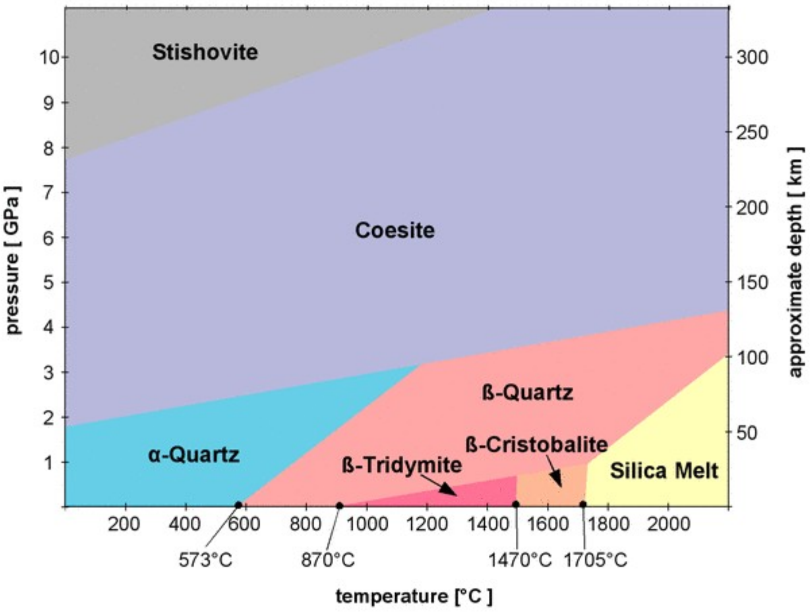

Figure 2.1: The silica phase diagram. Figure taken from http://www.quartzpage.de/gen_mod.html.

$(SiO_4)^{4-}$ tetrahedron is member of two threefold and two sixfold helices. All these characteristics can be found when inspecting Fig. 2.2.

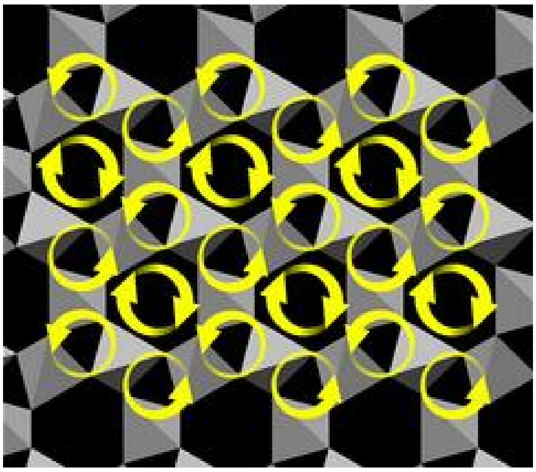

Figure 2.2: The quartz structure, in which the sixfold and threefold helices are indicated by clockwise and counterclockwise arrows, respectively (as an example). Figure taken from http://www.quartzpage.de/gen_struct.html.

Concerning the structures of β-tridymite and β-cristobalite (Fig. 2.3), they are based on 6-membered rings layers, composed of $(SiO_4)^{4-}$ corner-sharing tetrahedra; in the hexagonal rings, alternate tetrahedra point up and down. The layers are stacked on top of each other, linked by the tetrahedra vertexes, the stacking sequence being different for the two silica polymorphs. Tridymite has a two-layer repeat sequence ABABAB and an hexagonal structure, with layers parallel to the (001) planes; cristobalite has a three layer repeat ABCABC, which gives a face-centered cubic structure, with the layers parallel to the (111) planes [Putnis, 1992]. Figure 2.3 shows the comparison in the stacking sequences of β-tridymite and β-cristobalite: in the former, the six-membered rings are stacked in such a way that wide channels are present in the [001] direction, while, in the latter, structural "cages", constituted by one hexagonal ring, plugged by one upward pointing and one downward pointing tetra-

Table 2.1: The low pressure silica polymorphs. The two-letter terminology reported in brackets near the crystal systems of tridymite describes the modification of this phase: the first letter signifies the crystal system, the second the unit cell type [Nukui et al., 1978]. The lattice parameters are taken from Heaney, 1994.

β-polymorph	**β-Quartz**	**β-Tridymite**	**β-Cristobalite**
stable at	573-870 °C	870-1470 °C	>1470 °C
metastable at	–	117-870 °C	270-1470 °C
crystal system	hexagonal	hexagonal (HP)	cubic
space group	$P6_422$ or $P6_222$	$P6_3mmc$	$Fd3m$
lattice parameters	a = 5.00 Å c = 5.46 Å	a = 5.05 Å c = 8.28 Å	a = 7.13 Å
Si–O–Si angle	153°	180°	151°

α-polymorph	**α-Quartz**	**α-Tridymite**	**α-Cristobalite**
stable at	<573 °C	–	–
metastable at	–	<117 °C	<270 °C
crystal system	trigonal	monoclinic (MC) & orthorhombic (OC, OS, OP)	tetragonal
space group	$P3_121$ or $P3_221$	MC: Cc; OC: $C222_1$; OS: Superstructure; OP: $P2_12_12_1$	$P4_12_12$
lattice parameters	a = 4.91 Å c = 5.40 Å	MC: a = 18.49 Å, b = 4.99 Å, c = 25.83 Å, β = 117.75° OC: a = 8.73 Å, b = 5.04 Å, c = 8.28 Å OS: a = 95-65 Å, b = 5.02 Å, c = 8.18 Å OP: a = 25.65 Å, b = 5.02 Å, c = 8.15 Å	a = 4.97 Å c = 6.93 Å
Si–O–Si angle	144°	140°	147°

hedron [Palmer, 1994]. High temperature tridymite and cristobalite can be also thought as polytypes, as both structures can be constructed from a different stacking of the same module (the six-membered rings layer).

It is very well known from literature that the formation temperature of the HT silica polymorphs is favoured by the presence of alkali-metal impurities. A number of research works have been published during the last 30-40 years, showing the influence of impurities on the temperature of formation of the various polymorphs (see Heaney (1994) for a review). Back in 1941, Moseman & Pitzer showed that, when pure quartz is heated, it transforms directly into cristobalite at about 1050 °C, while tridymite forms only if a mineralizing agent is present (such as Na_2CO_3). Buerger (1954), Flörke (1956), Holmquist (1958) and Stevens et al. (1997) found the same result. Some authors proposed also that tridymite can not nucleate if a cristobalite nucleus is first formed, being the structure of tridymite very similar to that of cristobalite [Stevens et al., 1997; Flörke & Schneider, 1986; Nukui & Flörke, 1987]. Thermodynamic insight on the transformation of β-quartz into β-cristobalite is given by Richet et al. (1982), who calculated an equilibrium temperature, from their drop calorimetry measurements, for this transition, of 835 °C; the lowest experimental temperature for the formation of cristobalite was observed by Hill & Roy (1958) to be 900 °C, but with the presence of a mineralizing agent (Na_2CO_3).

In their 2001 paper, Venezia et al. showed the influence of alkali ions (Li, Na, K, and Cs) on the crystallization of the various crystalline forms of silica: (i) smaller ions (Li and Na) can produce crystalline silica polymorphs only in small quantities (Li promotes the formation of quartz at 800 °C, and of quartz and cristobalite at 1000 °C, while Na boosts the crystallization of cristobalite at 1000 °C); (ii) larger ions (K and Cs) need to be present in a larger amount (4 times more) to induce amorphous crystallization: K promotes the formation of cristobalite and tridymite at 800 °C, and of tridymite and cristobalite at 1000 °C, while Cs never reaches the complete crystallization of the silica glass and promotes the formation of cristobalite (with a large amount of amorphous silica) at 800 °C, and of cristobalite and tridymite (with still a smaller amount of amorphous silica) at 1000 °C. More recently, a study on

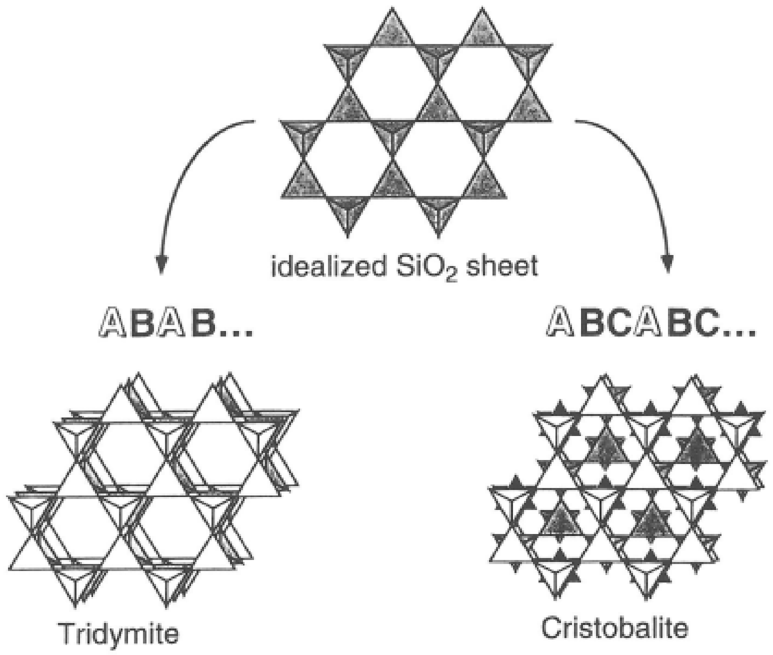

Figure 2.3: Two methods of stacking identical tetrahedral sheets. A simple two-layer AB repeat sequence gives the idealized hexagonal tridymite structure, while a three-layer ABC repeat sequence gives the idealized cubic cristobalite structure. Figure taken from Heaney et al. (1994).

the crystallization of glass-ceramic [Alharbi et al., 2012] in the K_2O-Na_2O-B_2O_3-SiO_2 system, with the addition of TiO_2, Cr_2O_3 and LiF, showed that at 1000 °C and for 1 h cristobalite formation is promoted (with very little tridymite), if no extra elements are added; the same happens (with small variations) with the inclusion of Cr and Ti to the system. On the other hand, the smaller Li ion induces, during the same thermal treatment, the crystallization of tridymite with a very little amount of cristobalite.

2.1.2 Industrial implications and aim of the project

Traditional ceramics are materials derived from common, naturally occurring raw materials, *i.e.* clay minerals, quartz and feldspar. These are the major components of a starting mixture used for the production of ceramics, but little quantities of other elements or compounds can be added, depending on the desired properties in the final object. Different may be the proportions of the raw materials put in the mixture; in the case of ordinary sanitary-ware materials, the simplest starting mixture has the following composition: 50 wt% kaolinitic clay, 25 wt% feldspar and 25 wt% quartz, so all these components play fundamental roles during the sintering process. In the light of these considerations, much interest is paid to cristobalite-involving reactions.

At high temperatures, quartz transforms in tridymite and/or cristobalite, which may preserve in the final product as metastable phases. Their presence in the ceramic bodies may be desirable, depending on the cases, due to their thermal expansion properties. In particular, α- and β-cristobalite have average bulk thermal expansion values of 91.7 and $6 \times 10^{-6}\ ^{-1}$, respectively [Fei, 1995], and such remarkably different thermal dilations lead to two important considerations:

1. a controlled formation of cristobalite is exploited to properly ”tune” the thermal expansion of a ceramic body, in order to make it match well with that of the glaze, thus avoiding the appearance of flaws due to a mismatch between inner and surface;

2. the shrinkage upon cooling of ceramic body can be cospicuous, so that, especially in sanitaryware-fireclay technology [Njoya et al., 2012], the use of chamotte (calcined clay or ball-clay) becomes extensive, in order to avoid the promotion of cristobalite crystallization, but this results in a reduction on the quality of the final product [Shackelford & Doremus, 2008].

For these reasons, studying the behaviour of quartz at high temperatures is crucial: if the cristobalite content can be handled, the properties of the final material may be improved. In this light, the formation of tridymite, instead of that of cristobalite, may become the solution at the "thermal expansion problem".

Moreover, the stage of advancement of any high temperature transformation, both in natural and industrial environment, depends on the particle size distribution (PSD) of the involved materials and firing-time experienced [Bernasconi et al., 2011]. Such an aspect becomes crucial in traditional ceramic manufacturing contexts, in which the raw materials used have undergone milling treatments to comply with processing features of the wholesale production, thus steering the phase composition and texture of the final output. Even though are aware that quartz is not the only source for cristobalite formation during ceramic production (see for example Ferrari & Gualtieri, 2006, and references within), being it the metakaolinite coming from thermal decomposition of kaolinite, still the kinetics of the HT silica phase transitions is an important step in the course of understanding the kinetics and the energetics of the whole high temperature process that generates a traditional ceramic body.

The aim of the present study is to investigate the quartz-tridymite-cristobalite transformations, paying particular attention to PSD of the starting quartz powders, firing-time, firing-temperature, presence of a mineralizing agent and sample preparation. The entire study was conducted keeping always in mind the usual industrial procedures, *i.e.* the maximum temperatures reached and the times necessary to bring the sintering process to completion (see Fig. 2.4 for an ordinary industrial firing procedure), as well as the addition of water in the starting powder mixture. In this view, two sets of experiments were planned: (i) those in which measurements are carried out on samples that have undergone annealing after thermal treatment; (ii) those that are meant to enable the study of the reaction kinetic parameters.
Such investigations are carried out by *ex-situ* and *in-situ* X-ray Powder Diffraction (XRPD) experiments. The quartz-cristobalite transformation turned out to be the only phase transition which was possible to be studied from the kinetic point of view; its kinetics is explored by isothermal runs and then interpreted by a formalism that uses the Avrami model.

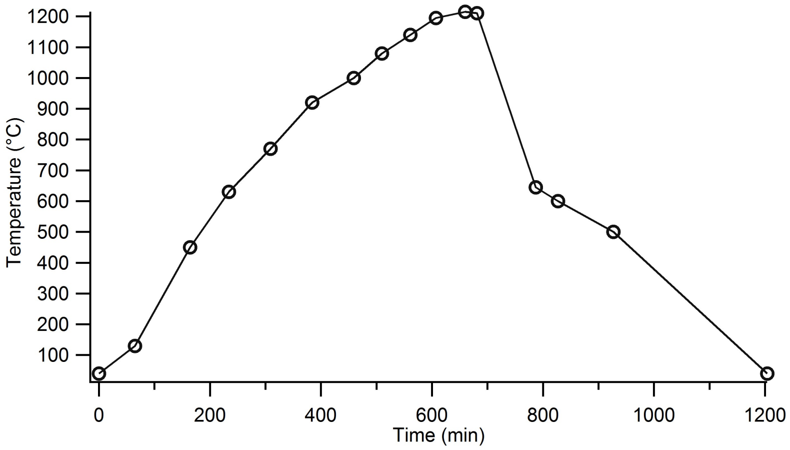

Figure 2.4: Example of an industrial cycle.

2.2 Investigations on pure quartz

First of all, interest has been paid to the evolution at high temperature of industrially-used pure quartz powders, in order to establish their behaviour and understand the transformations occurring without the use of any mineralizing agent. These powders have different grain size distributions: the principal aim is, indeed, to focus on the effect that particle size gives to the phase transitions which quartz undergoes. The samples and procedures used in the experiments and the results obtained are hereafter described.

2.2.1 Experimental

2.2.1.1 Starting powders

Five quartz powder samples were used to conduct the studies reported in this Chapter.
They were provided by Sibelco and have different micro-structural parameters, which are set out in Table 2.2, while Fig. 2.5 displays their individual PSDs.

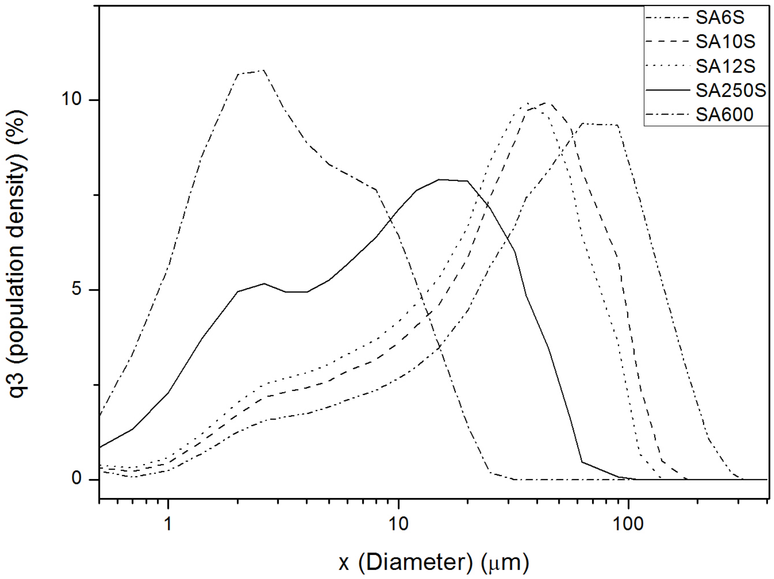

Figure 2.5: Particle size distribution of the five powder investigated.

Sample	<d>(μm)	D50 (μm)	Mode (μm)	<D$_v$>(nm)	RMS strain (10^{-4})
SA10S	28.38	23.42	50.22	270(3)	3.81(5)
SA6S	24.59	17.90	34.58	251(3)	4.06(5)
SA12S	23.05	18.24	31.50	256.8(1)	3.84(4)
SA250S	15.78	10.90	23.81	230(3)	3.72(6)
SA600	4.135	2.689	2.787	167(1)	3.48(7)

Table 2.2: Granulometric characterization of the starting powders. <D$_v$> and RMS strain come from the analysis of the powder diffraction peak broadening (see the experimental paragraph for details).

Given that the <d>-values of the quartz powders range from 4 to 29 μm but none of them lies in the interval 4.5-15 μm, two more mixtures were prepared, by blending the two finest raw powders: 50%SA600 (50% SA600

+ 50% SA250S; <d> = 9.958 μm) and 70%SA600 (70% SA600 + 30% SA250S; <d> = 7.629 μm).
The PSDs were measured as follows: first, 7 g of sample were mixed with 40 ml of de-ionised water, 5 ml of 1% sodium hydroxide solution and 5 ml of 1% sodium hexa meta phosphate (Calgon) solution, in a high speed homogeniser, at 10000 rpm, for one minute; then, the resultant slurry was screened through a 125 μm sieve and classified, taking into account the eventual residue found after sifting. PSDs were eventually measured by a CILAS LASER MOD 920L.

2.2.1.2 Samples and X-ray powder diffraction

Three series of high temperature experiments were carried out.
The first one was meant to provide an overview on the behaviour at non-ambient conditions of the available samples. *Ex-situ* analyses were performed on samples heated in a LKN-S86 Nannetti muffle furnace (Fig. 2.6) at 1200 and 1300 °C (ramp time: 6 hours) and then cooled slowly down to room temperature. Three sample preparation techniques were used: (i) dry compression to form tablets; (ii) mixing sample and water to obtain a paste; (iii) bare powders. Altogether, 21 samples were produced, three for each PSD.

Figure 2.6: The LKN-S86 Nannetti muffle furnace used for the sample preparation. Picture taken from `http://www.nannettisrl.it/prodotti.php?id=15`.

X-ray powder diffraction patterns were collected by a θ-2θ Bragg-Brentano parafocusing PANalytical X'Pert PRO diffractometer, equipped with multi-channel X'Celerator detector (Fig. 2.7). A Cu-Kα radiation with λ = 1.5418 Å was used. The optics were very simple, with a fixed divergence slit of 0.5° and an antiscatter slit of 0.5°. Samples were ground in an agate mortar and then pressed in a back-loading sample holder; diffraction patterns were collected from 5 to 80° 2θ, with a step size of about 0.017° 2θ, and a counting time of 30 s per step.

In the second series of measurements the coarsest, the finest and the intermediate grain-size powders (SA10S, SA600 and SA250S respectively) were used to investigate the quartz-cristobalite transformation as a function of time-temperature. Wet samples were chosen for such experimental runs as they provide conditions closer to those of the industrial environments. The samples were heated at 1200 and 1300 °C for 50 min, 2, 4 and 6 h, and then cooled down slowly. Heating treatments and XRPD measurements were carried out with the same instruments and experimental set-ups reported above.
The third set of measurements was oriented to the study of the reaction kinetics of quartz-cristobalite phase transition, by *in-situ* experiments. A θ-θ geometry Philips X'Pert diffractometer (Fig. 2.8) was used, equipped with an

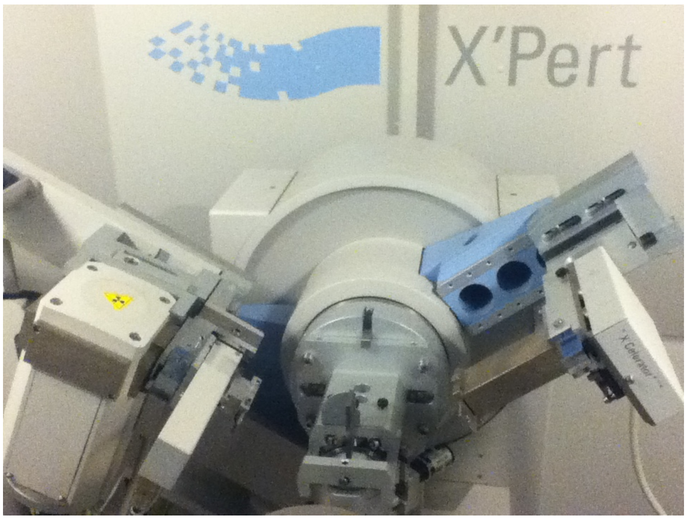

Figure 2.7: The diffractometer used for different analyses presented in this thesis.

Anton-Paar heating chamber (HTK 16 MSW) and a Pt heating strip, which is able to achieve a maximum temperature of ~1600 °C. (Both the latter diffractometer and the previous one are located at Department of Earth Sciences, University of Milano, Italy). Explorative heating ramps were performed on the finest and coarsest samples (SA600 and SA10S, respectively): the maximum temperature was ~1300 °C, and data were collected from 19 to 75° 2θ at room temperature before and after treatment, and from 19.5 to 27° 2θ, every 50 °C, until about 500 °C, and every 5 °C from 500 to 1300 °C, with a step-size of 0.03° 2θ and a counting time of 1 s/step. Such 2θ-intervals allow one to record the most intense peaks of quartz and cristobalite. Isothermal kinetics experiments were then carried out by the same diffractometer and high temperature device, and using SA600-SA10S-SA250S-samples. Each sample was studied along three isotherms, chosen as a function of the preliminary ramp experiments.

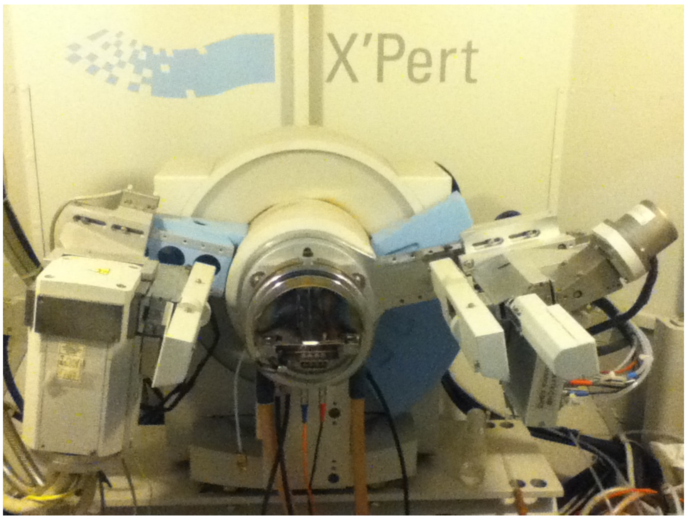

Figure 2.8: The diffractometer equipped with the Anton-Paar heating chamber. It was used for all the *in-situ* experiments conducted on quartz powders.

XRPD patterns were collected for all the samples, before and after thermal treatments. The quantitative analyses and the determination of the volume-average crystallite coherence domain size (<D_v>) and Root Mean Square (RMS) micro-strain [Snyder et al., 1999] were performed by the Rietveld refinement technique [Rietveld, 1969 & 2010] combined with the Warren-Averbach [Warren, 1969] method (MAUD software [Ferrari & Lutterotti, 1994] and isotropic model). For all the experiments, it was not possible to refine the RMS strain parameter of cristobalite when its content was less than 2 wt%: in such cases the too low diffraction peak intensity did not allow the separation of the size and strain profile contributions.

2.2.2 Kinetics theory

The role of the particle size in affecting the reaction kinetics of a powder has earlier been discussed by Koga & Criado (1997, 1998) and it is here re-considered. The PSD of quartz is modeled, by the sake of simplicity, through a histogram composed of a set of j-bins, each bearing a ξ_j fraction by weight of the original material with average $2D_j$ size.

It is useful to introduce the following definition for a generic observable F that takes the values F_j in the j^{th}-bin:

$$\overline{F} = \sum_j F_j \cdot \xi_j. \tag{2.1}$$

Assuming that the activation energy E_a is the same for any particle size, one then can write the reaction kinetics equation for the j-fraction as

$$\mathrm{g}(\alpha_j; p_j) = A_j \exp\Big(-\frac{E_a}{\mathrm{R}T}\Big) \cdot t \tag{2.2}$$

where α_j is the coordinate of transformation attributed to the j^{th}-bin (being α a generic coordinate that monitors the new phase of formation, for which $\lim_{t\to\infty} \alpha(T) = 1$ and defined by Eq. 1.44) and p_j is a possible parameter depending on the j^{th}-bin. In some case, it may be convenient to use $\ln(\mathrm{g}(\alpha_j; p_j)) = \ln(A_j) - \frac{E_a}{\mathrm{R}T} + \ln(t)$; the formalism developed here, starting from Eq. 2.2, does not change.
If one sets $\alpha_j = \overline{\alpha} + \epsilon_j$ and $p_j = \overline{p} + \delta p_j$, then, from Eq. 2.2, it follows:

$$\sum_j \mathrm{g}(\overline{\alpha} + \epsilon_j; \overline{p} + \delta p_j) \cdot \xi_j = \exp\Big(-\frac{E_a}{\mathrm{R}T}\Big) \cdot t \cdot \sum_j A_j \cdot \xi_j \tag{2.3}$$

If one Taylor-expands in ϵ_j and δp_j the right-hand member of Eq. 2.3, and
(i) takes into account that $\sum_j \epsilon_j \times \xi_j = 0$ and $\sum_j \delta p_j \cdot \xi_j = 0$;
(ii) neglects the second order terms in ϵ_j and δp_j;
then it follows

$$\sum_j \mathrm{g}(\overline{\alpha}; \overline{p}) \cdot \xi_j = \exp\Big(-\frac{E_a}{\mathrm{R}T}\Big) \cdot t \cdot \overline{A}. \tag{2.4}$$

After having tried out several kinetic models [Khawam & Flanagan 2006], an Avrami-like formalism [Avrami, 1939; Avrami, 1940; Avrami, 1941] has been chosen as it proved to be the most satisfactory one in terms of: (i) matching between observations and theory, (ii) and consistence between the inferred E_as *versus* <d> of quartz. In this light, the reaction rate is described by the general equation beneath

$$[-\ln(1-\alpha)]^{\frac{1}{n}} = kt. \tag{2.5}$$

The dependence on each j^{th}-bin is transferred to the exponential *n*, *i.e.* n_j, and the equation above changes accordingly into

$$\Big[\ln(-\ln(1-\alpha_j))\Big]\frac{1}{n_j} = \ln(A_j) + \Big[-\frac{E_a}{\mathrm{R}T}\Big] + \ln(t). \tag{2.6}$$

Summing over all possible bins and taking into account the fraction by weight for each j^{th}-bin, one has

$$\sum_j \Big[\ln(-\ln(1-\alpha_j))\frac{1}{n_j}\Big]\xi_j = \Big(-\frac{E_a}{\mathrm{R}T}\Big) + \ln(t) + \sum_j \ln(A_j)\cdot\xi_j. \tag{2.7}$$

From Eq. 2.4 it finally follows:

$$\ln(-\ln(1-\overline{\alpha}))\cdot\sum_j\Big(\frac{\xi_j}{n_j}\Big) = \Big(-\frac{E_a}{\mathrm{R}T}\Big) + \ln(t) + \sum_j \ln(A_j)\cdot\xi_j, \tag{2.8a}$$

and finally

$$(-\ln(1-\overline{\alpha}))^{\frac{1}{\hat{n}}} = \hat{\mathrm{A}}\cdot\exp\Big(-\frac{E_a}{\mathrm{R}T}\Big)\cdot t, \tag{2.8b}$$

where $\frac{1}{\hat{n}} = \overline{\frac{1}{n}} = \sum_j\Big(\frac{\xi_j}{n_j}\Big)$ and $\ln(\hat{\mathrm{A}}) = \overline{\ln(\mathrm{A})} = \sum_j \ln(A_j)\cdot\xi_j$ are the quantities measured by isothermal experiments.

2.2.3 Results and discussion

Several experiments have been carried out, in order to determine the amount of cristobalite formed and to understand the kinetics of the quartz-cristobalite transformation. They were conducted on pure quartz powders (i), tablets (ii) and pastes (iii) by heating *ex-situ* at various temperatures and for different times. *In-situ* measurements were also performed on the coarsest and the finest samples, with the aim of getting an idea of the crystallization temperature of the first cristobalite. After that, a full isothermal kinetic analysis was done by applying the Avrami model for interpretation of data.

The results described hereafter are divided into two parts: the characterization of the starting quartz powders, used also in the following study (see Section 2.3), and the discussion of the results obtained after the firing process of these powders.

2.2.3.1 Characterization of the starting powders

Tables 2.2 and 2.3 show the results of a characterization of the initial quartz powders. The volume-average domain size and the RMS strain of quartz are presented in Table 2.2, and can be directly compared with the granulometric parameters in the same Table. In particular, note that the smaller <d> the smaller <D_v>. The differences in terms of <D_v> between starting powders are expectable even by a bare inspection of Fig. 2.9, which shows the portion of diffraction pattern, wherein the main peak of quartz is located.

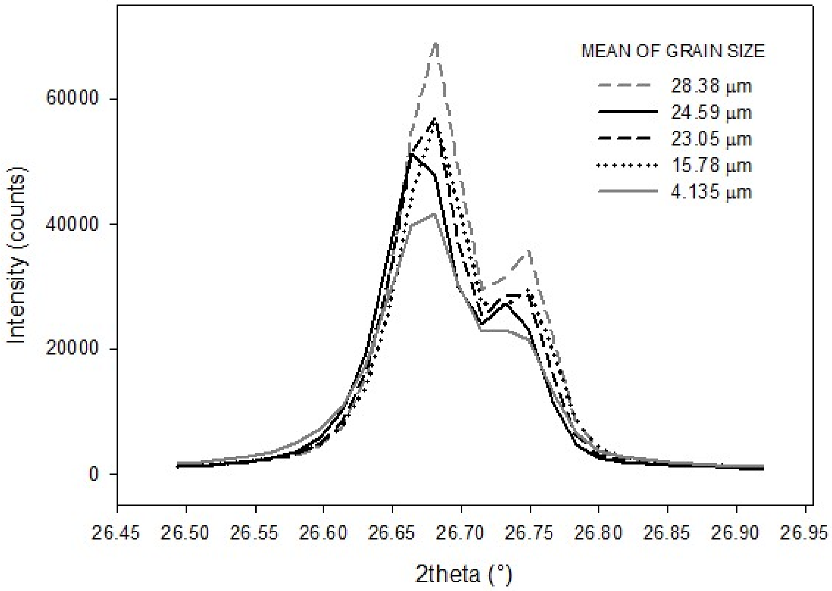

Figure 2.9: The main peak of quartz for the five starting powders under investigation.

Table 2.3: Chemical and physical characterization of the starting raw powders.

Sample	% min SiO_2	% max Al_2O_3	% max Fe_2O_3	% max TiO_2	% max K_2O	Loss on ignition (%)	Density (T/m^3)	Specific surface (cm^3/g)
SA10S	99.0	0.3	0.03	0.03	0.05	0.2	1.0	2800
SA6S	99.0	0.3	0.04	0.03	0.05	0.2	1.2	1900
SA12S	99.0	0.3	0.03	0.03	0.05	0.2	0.9	3500
SA250S	99.0	0.4	0.05	0.03	0.05	0.3	0.70	5700(900)
SA600	99.0	0.5	0.06	0.03	0.05	0.3	0.5	13800(2800)

A decrease of the particle size is accompanied by an increase of the peak's broadening, indicating a general reduction of the crystalline domain size and increase of RMS strain. The inverse relationship between crystallite size and RMS strain is very well known in literature in materials subjected to mechanical treatment [Criado et al., 1986; D'Incau et al., 2007].

2.2.3.2 Characterization of the treated powders

***Ex-situ* experiments**

Fig. 2.10 shows the Rietveld refinement, performed with MAUD software, of the finest wet sample heated at 1200 °C for 6 hours, just as an example. The blue dots are the experimental data, while the black superimposed line is the calculated pattern; the curve below the graph is the difference between calculated and experimental data and should be as linear as possible. From similar fits of all the samples, the quantity of cristobalite was obtained, as well as the crystallite size and the RMS strain.

Fig. 2.11 displays the cristobalite amount obtained from the *ex-situ* experiments at 1200 °C and 1300 °C for 6 hours, as a function of <d> and sample preparation. Fig. 2.11 A shows the results related only to experiments

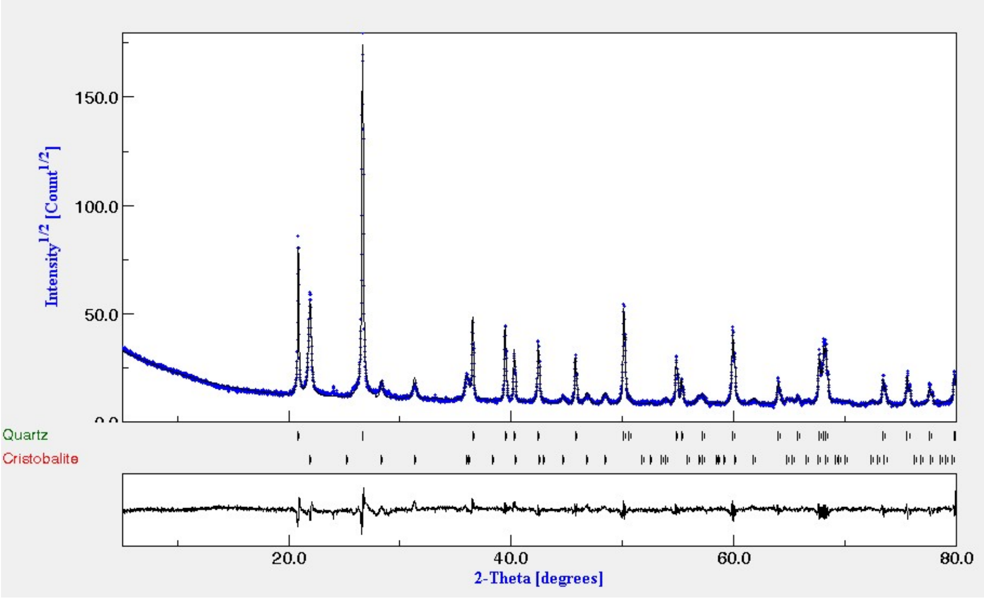

Figure 2.10: Rietveld refinement, made with MAUD software, of the finest sample wetted with water and fired at 1200 °C for 6 hours. The blue dots are the experimental data, the black superimposed line is the calculated pattern and the curve below the graph is the difference between calculated and experimental data.

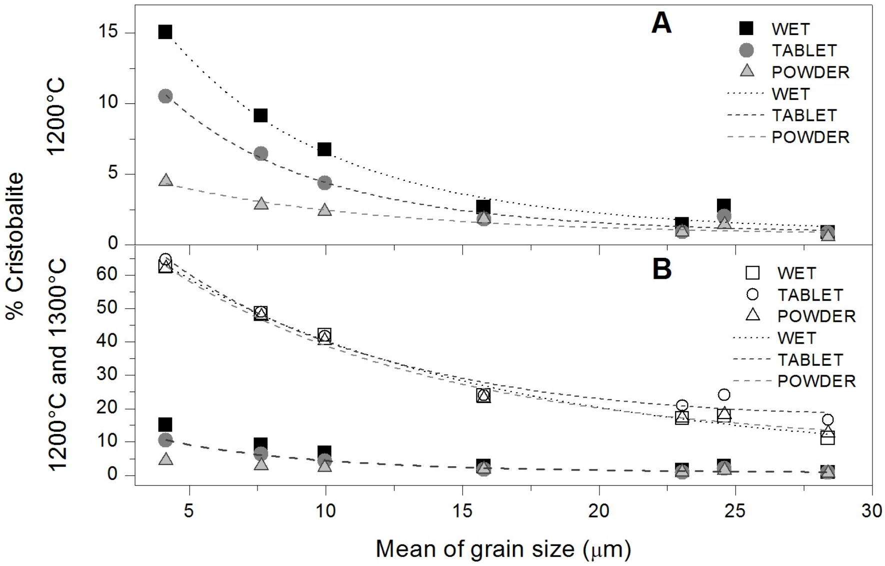

Figure 2.11: Wt% of cristobalite after the *ex-situ* test conducted at 1200 °C (A) and at 1300 °C (B). B shows again results at 1200 °C as a comparison.

with the maximum temperature of 1200 °C, whereas Fig. 2.11 B collates the issues from both temperatures. The formation of cristobalite through such treatments exhibits a remarkable dependence on both <d> and sample preparation. Rising temperature by 100 °C causes the amount of formed cristobalite to increase by more than 6 times, for the sample with the smallest particle size, and by 2-3 times, for the coarsest one. The method of sample preparation influences the final quantity of cristobalite only when the firing temperature is 1200 °C, and in particular for the finest samples: the wet sample preparation boosts cristobalite (Fig. 2.11 A), whereas the bare and dry powders yield the lowest amount; such difference nearly cancels out at 1300 °C (Fig. 2.11 B). This is likely ascribable to that wet preparation allows a better particle-particle contact, thus favouring heat transmission and solid state reactions induced thereby.

Fig. 2.12 concerns the cristobalite formation in the finest, coarsest and intermediate size samples at 1200 °C and 1300 °C, as a function of time.

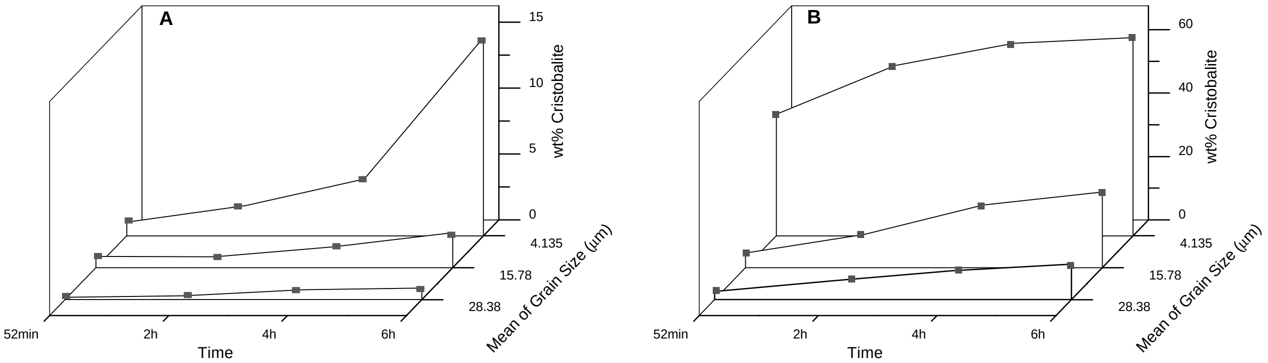

Figure 2.12: Amount of cristobalite formed at 1200 °C (A) and 1300 °C (B) applying the maximum temperature for different times.

At 1200 °C, the amount of cristobalite is in general small, but a remarkable increase occurs in the finest sample only, and after 6 hour of treatment. At 1300 °C the effect of the firing time seems to be modest after 52 min, regardless of the average particle size.

Fig. 2.13 shows the ΔD_v of the samples, *i.e.* the difference between the crystalline domain size of quartz before and after high temperature treatment, as a function of the amount of cristobalite formed at 1200 °C and 1300 °C. At 1200 °C (Fig. 2.13 A), the fine samples show a negative value for ΔD_v, and therefore they exhibit a larger average crystallite size after heating (grain growth is well known to be promoted by high temperatures). However, all samples with a large <d> (above $\sim$15 μm) have a smaller average crystallite size after heating, showing therefore that the reactions occurring on cooling have an influence on the coherence of the domains that tend to *break* due to the volume difference of the involved polymorphs. At the highest temperature (1300 °C, Fig. 2.13 B), this is again true, but the sample with a <d> of about 25 μm lies somehow in between the two different behaviours.

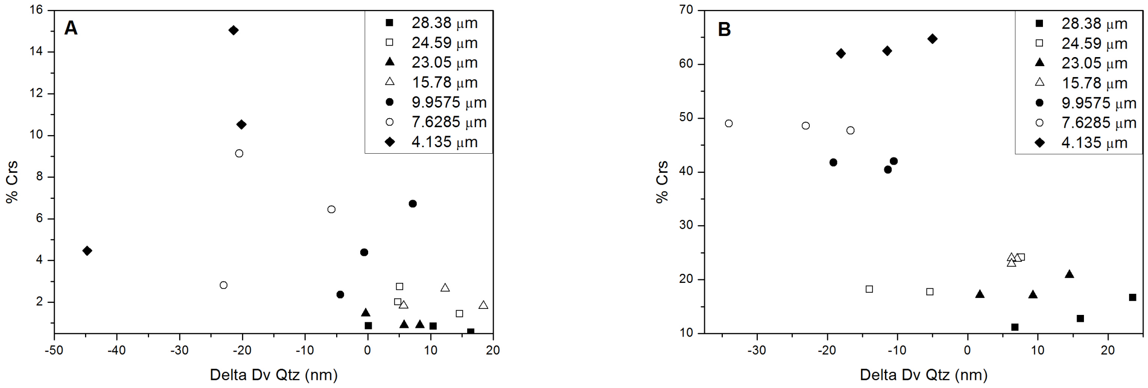

Figure 2.13: Relationship between ΔD_v of quartz and the amount of cristobalite formed at 1200 °C (A) and 1300 °C (B).

The difference between the initial and the final strain of quartz (ΔRMS) was also determined, and is reported in Fig. 2.14. Such difference is negative for all of the samples explored, proving the occurrence of residual stress in quartz undergone high temperature treatment. The fine samples seem to be more affected than the other samples, but all the values are very small and close to each other (order of 10^{-4}-10^{-5}).

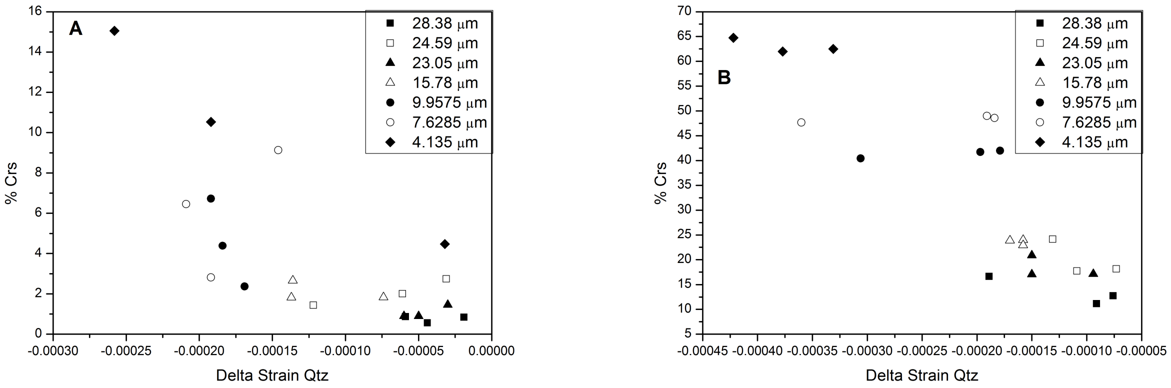

Figure 2.14: Relationship between RMS strain of quartz and the amount of cristobalite formed at 1200 °C (A) and 1300 °C (B).

Both ΔD_v and ΔRMS strain do not show any dependence on the method of sample preparation.

Heating ramp experiments

In-situ heating ramp experiments on the finest and the coarsest powders were performed, reaching about 1300 °C (details on the procedure can be found in the experimental section). The coarsest sample (SA10S), of which Fig. 2.15 A shows the diffraction patterns in the interested thermal range, starts to transform into cristobalite at 1250 °C, and at 1300 °C about 2.70% of this latter is formed.

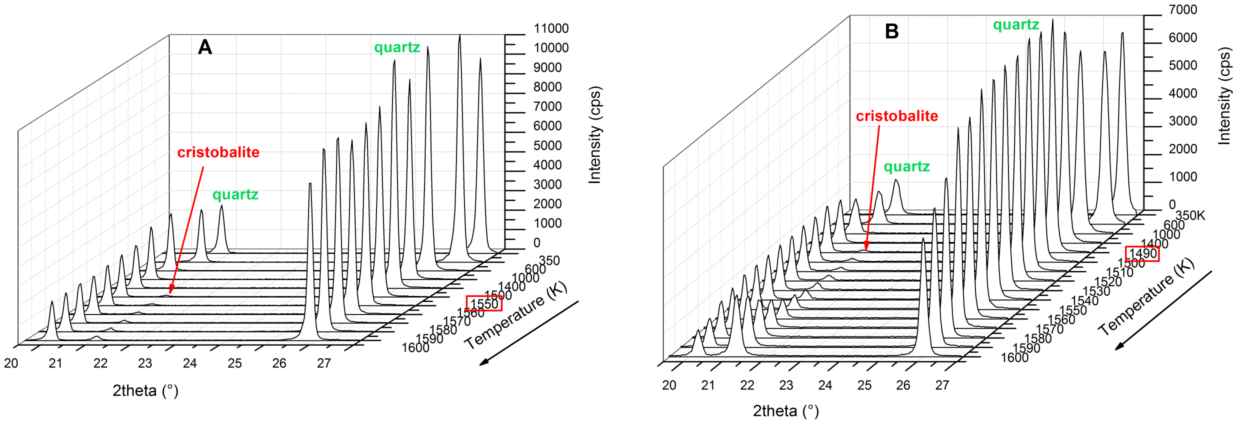

Figure 2.15: Diffraction patterns at increasing temperatures collected in the little angle range which contains the main peaks of both quartz and cristobalite. A refers to the coarsest sample (SA10S) and B to the finest provided powder (SA600).

The finest sample (SA600) gives at the end of the heating ramp about 40.60% of cristobalite, which starts to form at about 1190 °C (see Fig. 2.15 B). As expected, this hints a relevant role is played by the particle size, in quartz-cristobalite conversion.

Isothermal kinetics analyses

On the basis of the *ex-situ* and *in-situ* experiments discussed above, we have chosen the temperature values at which to carry out isothermal measurements to investigate the quartz-cristobalite reaction kinetics, using the finest (SA600), the coarsest (SA10S) and the intermediate (SA250S) grain-sized samples.

Fig. 2.16 reports the three isotherms investigated for each sample; they trend linearly and are nearly parallel to each other, thus suggesting that the reaction mechanism is independent of temperature, over the explored range. Moreover, the first data points, referred to the lowest temperature, follow a trend with different slope with respect to the higher temperatures, in all the samples. As demonstrated, the data can be fitted nicely with an Avrami-type model; this means that the formation of cristobalite starts with an induction time (necessary for the growth of critical-sized nuclei, which later start to grow into proper crystals), followed by an acceleration period. The induction time is strongly temperature-dependent: it is longer at lower temperature, but considerably decreases with increasing temperature. The different slope in the data with the lowest temperature may therefore be due to this reason and this fact may explain why, in some cases, the parallelism of lines is not respected.

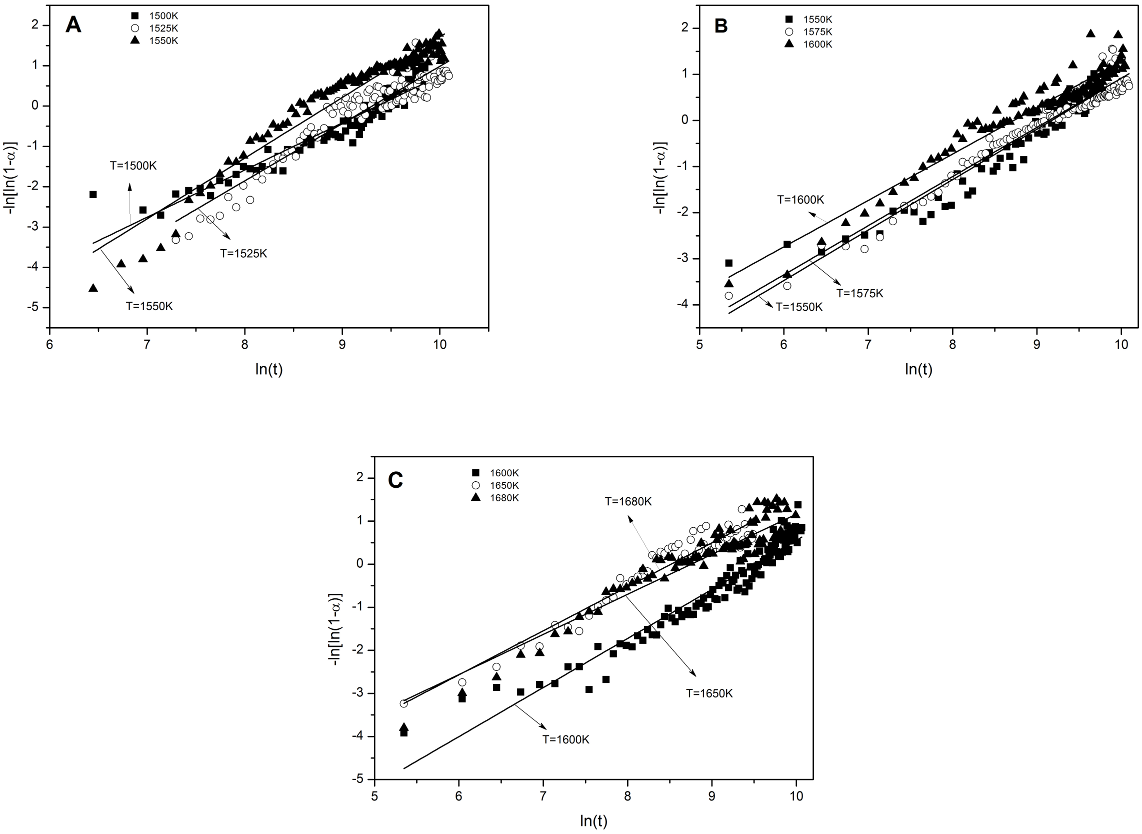

Figure 2.16: Application of the Avrami equation for the finest (A), intermediate grain-sized (B) and coarsest (C) powders, heated at different temperatures depending on the sample: 1500, 1525 and 1550 K for SA600; 1550, 1575 and 1600 K for SA250S; 1600, 1650 and 1680 K for SA10S.

The kinetic exponent n ranges from 0.89 to 1.49 (see Table 2.4): from Galwey & Brown (1998), fractional n-values hint at diffusion-controlled crystal growth, or processes involving complex size and shape particle distributions for reactants and transformation products.

In particular, as to n one observes that:

1. SA250S and SA10S give n values close to each other, with <n> around 1;
2. SA600 yields n values about 1.5, save for T = 1500 K. This brings to light that the finest sample exhibits a

Table 2.4: Results from the kinetics experiments

Sample	Average grain size <d>(μm)	Working T (K)	n	<n>	ln(k) (s^{-1})	A (s^{-1})	E_a (kJ mol^{-1})
SA600	4.135	1500	1.15	1.37	-9.37	411.83	193(73)
		1525	1.47		-9.28		
		1550	1.49		-8.87		
SA250S	15.78	1550	1.06	1.01	-9.22	115.7	181(78)
		1575	1.04		-9.16		
		1600	0.94		-8.78		
SA10S	28.38	1600	1.07	0.96	-9.51	3710.79	234(191)
		1650	0.92		-8.44		
		1680	0.89		-8.78		

remarkable sensitivity to T, as proven by that a 25 K-shift is sufficient to affect the kinetic exponent. Taking into account Eq. 2.8a, it is likely that an effect related to the size-classes gives rise to such discrepancy with respect to what occurs at higher temperatures;

3. the average grain size influences n so as to lead to two distinct kinetic classes: the one including SA250S and SA10S, and the other SA600;
4. <n> seems to exhibit an inverse dependence on <d>.

Fig. 2.17, which represents the Arrhenius plot for all the samples, shows a reasonably good correlation ($R^2 \sim 0.85$ in all the cases, except in SA10S, where the k values are more scattered, leading to a lower R^2) that allows one to determine the pre-exponential parameter A and the apparent activation energy E_a of the phase transition process.

The activation energies change from 181 to 234 kJ mol^{-1}, which are in keeping with literature values for such a kind of processes [*e.g.* Gualtieri et al., 1995; Dapiaggi et al., 2007; Hu et al., 2007; Gualtieri et al., 2003; Dos Santos & Dos Santos, 2002]. The E_a's are similar to each other, and almost undistinguishable if one takes into account the uncertainties, determined by the errors propagation. In this view, the grain size seems not to significantly influence the activation energy of the transition process, as shown in Fig. 2.18, in agreement with the assumption of the model here used that takes E_a as independent of the size-class. The A-pre-exponential coefficients exhibit a remarkable scattering, without any apparent correlation to <d>.

After cooling to room temperature, full-range diffraction data were collected and then analysed with the Rietveld refinement. Figure 2.19 shows the amount of cristobalite crystallized after each isotherm. As seen before, the sample with the smaller grain dimension (SA600) reacts more easily: cristobalite forms at lower temperatures with respect to the other samples and in larger quantities upon the same applied conditions.

At a given temperature the amount of cristobalite formed increases upon decreasing the grain size of quartz involved. The more the particle size increases, the more the temperature necessary to crystallize cristobalite is higher and the less is the tendency of this phase to form. The latter aspect is shown by that the slopes of the linear interpolations of cristobalite *versus* T for each sample in Figure 2.19 decrease as a function of <d>.

2.2.4 Conclusions

This first study on quartz powders has been undertaken with the aim to elucidate the kinetics of the quartz-cristobalite phase transition which occurs during the production of many ceramic materials. In particular, the attention has been focused on the effects of size reduction on the cristobalite formation at high temperatures, con-

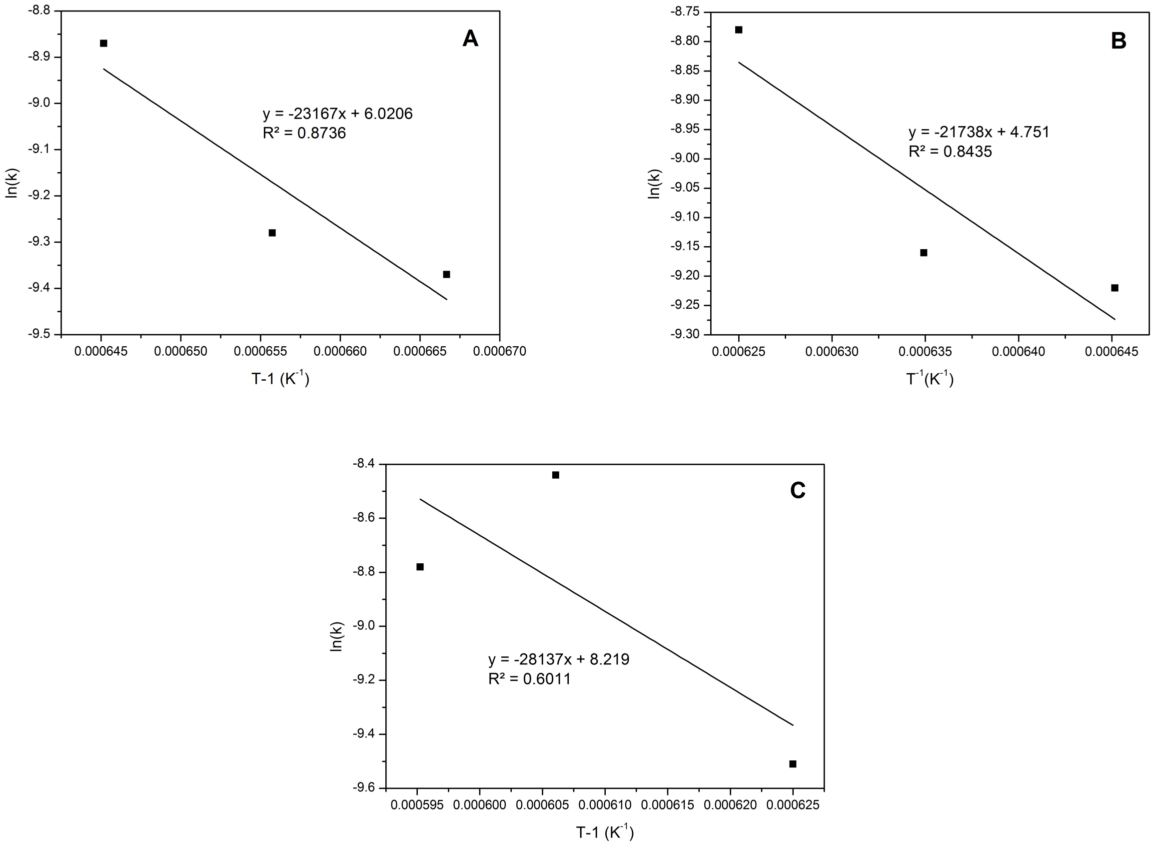

Figure 2.17: Arrhenius plot for SA600 (A), SA250S (B) and SA10S (C), starting from the values of k obtained from the application of the Avrami model.

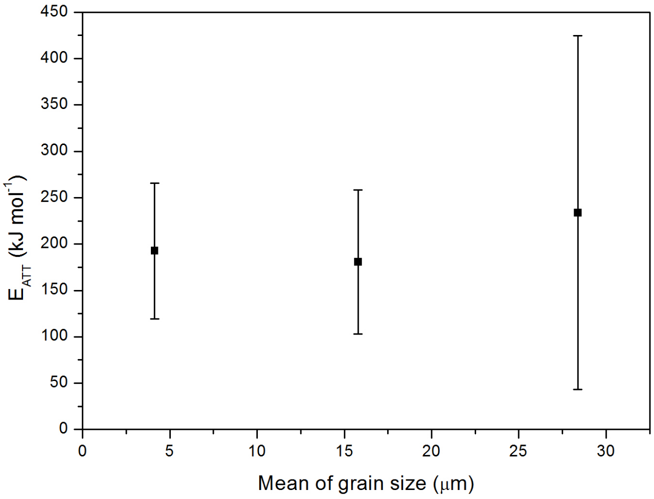

Figure 2.18: Apparent activation energy as a function of grain size.

sidering both the obtained quantities of that phase and the kinetic process of the transformation.

On the ground of the results discussed above, the following conclusions have been achieved:

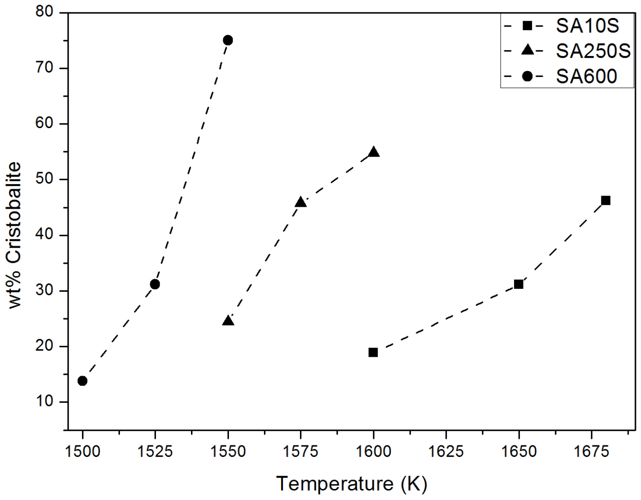

Figure 2.19: Amount of cristobalite after the isothermal analyses for the three samples investigated.

1. high temperature promotes cristobalite crystallization and the method of sample preparation influences the amount of its formation (wet samples show larger amounts of cristobalite), but only at comparatively low temperature, *i.e.* 1200 °C. This is reflective of a kinetic effect;
2. the formation of cristobalite is always favoured by a small grain size of the starting powder, in keeping with that generally the smaller the particles, the more easily a transformation takes place;
3. the Avrami model proves that the exponential term, n, is related to the average particle size of starting quartz, whereas the activation energy, E_a does not seem to depend on <d> of the powders on study;
4. n values range from 0.89 to 1.49, according to the rule that the smaller <d> the larger n. E_a has average value of ~203 kJ mol^{-1}.

2.3 Investigations with the usage of mineralizing agents

After a thorough study on pure quartz, which firing gives only cristobalite as forming phase, attention has been given to how mineralizing agents added to the starting quartz powders change the HT phase transitions. It is evident from literature that mixing quartz with some elements, such as Na, K, Ca, Li, not only tridymite becomes stable and crystallizes, but also the transformation temperatures are lowered (see Subsection 2.1.1). The present Section reports the *ex-situ* and *in-situ* experiments made on some of the same quartz powders employed in the previous study, mixed with a sodium or potassium based aqueous solution, and shows the results achieved, also comparing with the case of pure quartz, already discussed above.

2.3.1 Experimental

SA600, SA250S and SA10S powders, whose characteristics are illustrated in Table 2.2 and in Fig. 2.5, were considered for the following new experiments.

About 5 g of each powder were mixed with 1.8 ml of 20 wt% aqueous sodium or potassium hydroxide solution, in order to obtain a viscous blend, as in the industrial process, and treated at high temperatures in the same Nannetti muffle furnace mentioned above, at 900, 1000, 1100 and 1200 °C. After dwell times of 1 hour (as in industry) and 6 hours, the samples were cooled slowly down to ambient conditions and ground up in a Retsch ball mill MM400 (Fig. 2.20) for X-ray powder diffraction data collections. In this way, a total number of 48 samples were produced and analysed from an *ex-situ* point of view.

In order to estimate the glass content formed during the HT process, 10 wt% of corundum was added to all the fired samples as an internal standard. These mixtures were ground again in an agate mortar, in order to make them uniform, and pressed in back-loading sample holders for XRPD measurements. The θ-2θ diffractometer and the conditions of data collection were the same as reported in Subsection 2.2.1.2. The Rietveld refinements were carried out again using the MAUD software (with the application of the isotropic model) and the determination of the amorphous phase was obtained according to Gualtieri (2000).

Figure 2.20: The Retsch ball mill MM400. Picture taken from `http://www.daigger.com/store/retsch-mm301-ball-mill1909ba/18275`.

Heating ramps on the SA600 powder, wetted with NaOH and KOH solutions, in the way described above, were conducted using the θ-θ diffractometer shown in Fig. 2.8, in order to study the transformations occurring during heating, by *in-situ* experiments. Data collections were firstly carried out every 50 K from room conditions up to 1600 K, in a narrow range of diffraction angles (19.5-27° 2θ), to have an idea of the temperatures to investigate in details afterwards. The thorough measurements were then conducted between 15 and 75° 2θ every 20 K from 1100 until 1500 K. The step size and the counting step were always 0.03° 2θ and 1 s/step, respectively.

2.3.2 Results and Discussion

Several experiments have been performed, in order to find out the minimum temperatures (and times) (i) at which only tridymite is formed, (ii) for the first tridymite to form and (iii) for the crystallization of cristobalite, so to compare with the study presented in Section 2.2.

2.3.2.1 *Ex-situ* results

Several tests have been performed by heating *ex-situ* at various temperatures and by analysing the products. Samples, which differ not only in the firing temperature but also in the grain size distribution of the starting quartz and in the chemical composition of the solution added, were collected after one hour (as in a real industrial process) and six hours of dwell time at the maximum temperature. Table 2.5 summarizes the results obtained after treatment of all these samples.

Table 2.5: Results from the *ex-situ* experiments, based on the use of two mineralizing agents.

Sample	Mineralizer	T (°C)	Quartz (wt%)	Cristobalite (wt%)	Tridymite (wt%)	Amorphous phase (wt%)	Quartz (wt%)	Cristobalite (wt%)	Tridymite (wt%)	Amorphous phase (wt%)
			dwell time = 1 h				dwell time = 6 h			
SA600	KOH	900	62.08	0.00	0.00	37.92	74.94	0.00	0.00	25.06
		1000	74.06	0.00	0.00	25.94	31.32	32.83	5.15	30.71
		1100	1.29	38.17	33.78	26.77	1.45	17.44	61.48	19.62
		1200	0.38	9.30	55.95	34.37	0.29	2.12	63.44	34.14
	NaOH	900	83.71	0.00	0.00	16.29	55.69	5.48	1.46	37.36
		1000	4.84	52.29	10.34	32.53	0.86	7.14	61.72	30.28
		1100	1.15	8.11	52.70	38.04	0.17	3.76	51.19	44.88
		1200	0.23	7.61	60.18	31.99	0.13	3.27	56.23	40.37
SA250S	KOH	900	81.81	0.00	0.00	18.19	87.45	0.00	0.00	12.55
		1000	76.93	4.49	0.00	18.58	11.91	54.12	13.20	20.78
		1100	3.92	52.33	20.41	23.34	3.11	19.51	55.16	22.22
		1200	0.92	24.44	51.50	23.14	0.31	10.27	63.79	25.62
	NaOH	900	80.13	0.00	0.00	19.87	61.80	11.43	0.00	26.77
		1000	38.69	42.37	4.95	13.99	2.74	17.31	49.24	30.72
		1100	1.26	23.08	46.73	28.93	0.39	11.90	61.74	25.97
		1200	0.36	12.64	55.92	31.08	0.62	9.80	62.55	27.04
SA10S	KOH	900	77.45	0.00	0.00	22.55	80.78	0.00	0.00	19.22
		1000	78.06	0.00	0.00	21.94	5.71	44.84	18.96	30.49
		1100	2.50	31.16	44.18	22.16	1.06	14.02	59.02	25.90
		1200	1.14	18.15	56.56	24.15	0.40	10.53	69.44	19.62
	NaOH	900	79.56	0.00	0.00	20.44	50.83	22.11	0.00	27.06
		1000	15.95	39.70	16.10	28.26	4.46	14.21	52.48	28.86
		1100	1.88	15.17	54.20	28.75	0.66	10.87	69.63	18.84
		1200	0.46	7.96	59.18	32.40	1.83	7.47	61.29	29.42

As easily comprehensible, many are the factors that can influence the occurring silica phase transitions. The present Subsection is, therefore, divided into several parts, in order to focus on few combined parameters.

Influence of temperature and time

Fig. 2.21 compares the results on the finest sample (<d> = 4.135 μm), as a function of temperature. On the left hand side, the amounts of the phases obtained after treatment with KOH are represented, while the right hand side shows the quatities obtained with the use of NaOH. In each half of the figure, it is possible to appreciate the influence of dwell time: the left hand side has a dwell time of 1 hour, the right hand side has a dwell time of 6 hours. The influence of temperature is shown on the x-axis. The finer sample has been chosen for the representation of results, as it is the smaller grain-sized and, as seen in the previous Section, is the most reactive, thus its behaviour is the most interesting.

From that figure, it appears clear that, at 900 °C, the amount of quartz is very high for all time/mineralizer combinations. The only forming phase is the amorphous one, which is always present in quite relevant amounts (between 16 wt% and 38 wt%). The temperature of 900 °C is, therefore, too low to allow crystalline phases to grow.

Looking at the left hand side of Fig. 2.21, *i.e.* the one in which KOH was used as mineralizer, it can be noticed that quartz is still present at 1000 °C, though less than half for the 6 hours dwell time with respect to the 1 hour dwell time, and it disappears (less than 2 wt%) at the same temperature when NaOH is used and 6 hours of dwell time are applied. At higher temperatures quartz is still almost completely removed. At 1100 °C the main difference is in the ratio cristobalite/tridymite, favourable to the former for 1 hour dwell time, and to the latter for the 6 hours dwell time. From this observation, it is reasonable to think that cristobalite is the first forming and that tridymite

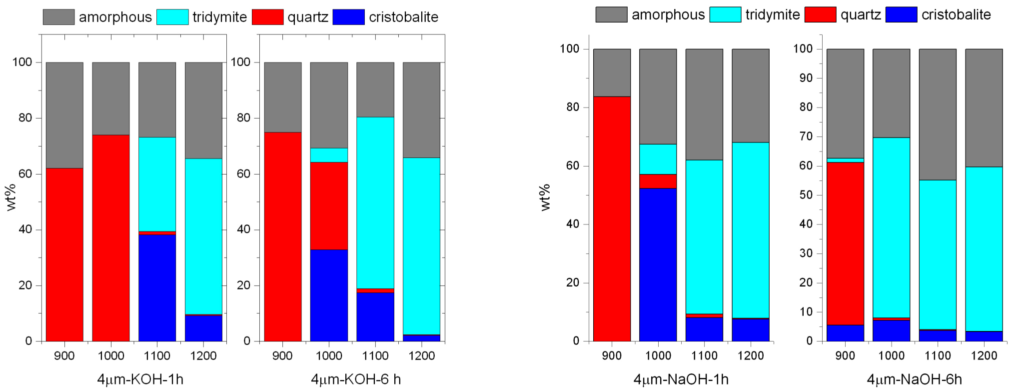

(a) KOH

(b) NaOH

Figure 2.21: Influence of temperature and time on the finest sample: the data are presented as a function of temperature in each graph, with KOH as mineralizer on the left half, and NaOH on the right half, and with 1 hour dwell time on the left hand side of each half, 6 hours dwell time on the right.

grows also at its expense (in accordance with Stevens et al. (1997); Flörke & Schneider (1986); Nukui & Flörke (1987)). At 1200 °C, the difference between the two dwell times gets smaller, and the ratio cristobalite/tridymite becomes lower, as the tridymite crystallization is promoted.

The right hand side of the same figure, with NaOH as mineralizer, shows a smaller amount of quartz at 1000 °C, with respect to KOH, at 1 hour as well as at 6 hours dwell time. The amount of cristobalite is large only at 1000 °C for 1 hour dwell time, while for the rest of time/temperature combinations it becomes fairly small, with tridymite as the major phase.

Influence of mineralizer and time

Fig. 2.21 highlights clearly also the various effects produced by different mineralizers. At 900 °C and 1 hour dwell time NaOH forms smaller amounts of the first new phase, *i.e.* the amorphous phase, with respect to KOH, letting one think that the reaction is slower and needs more time and/or higher temperatures to speed up. After this induction time, the reactions seem to be faster and facilitated when NaOH is used. Indeed, at 1000 °C and 1 hour the reduction of quartz is signifiant and the formation of the HT phases (especially that of cristobalite) is promoted when the mineralizing agent is NaOH, while KOH forms again only the amorphous material. As seen before, cristobalite crystallizes first, while tridymite forms also from it, thus the progress of the reaction should lead to a decrease in the cristobalite content and an increase in the tridymite content. This is what happens also here: tridymite crystallizes at the expense of quartz, as well as of cristobalite, which, therefore, decreases very much. This phase transition occurs before in the case of the usage of NaOH (at 1000 °C, after 6 hours of dwell time, almost all the cristobalite is gone), but KOH is able to reach a similar ratio cristobalite/tridymite when 1200 °C is applied for 1 hour (and 6 hours).

Influence of grain size and time

For the comparison among the grain size of the starting quartz, two temperatures have been chosen: 1000 °C and 1200 °C, as they appear to be the most interesting. 900 °C and 1200 °C are not shown, because the former does not induce much reactions and the latter seems to take the samples at the equilibrium stage.

Fig. 2.22 refers to the influence of grain size at 1000 °C: again KOH (1 and 6 hours dwell time) is on left hand side and NaOH is on the right hand side.

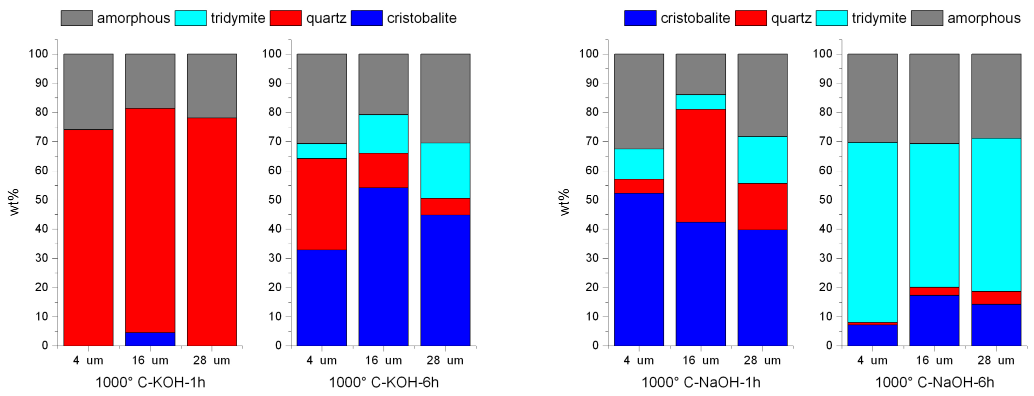

(a) KOH (b) NaOH

Figure 2.22: Influence of grain size and time at 1000 °C: the data are presented as a function of grain size in each graph, with KOH as mineralizer on the left half, and NaOH on the right half, and with 1 hour dwell time on the left hand side of each half, 6 hours dwell time on the right.

Starting again by analysing the results obtained with the use of KOH (Fig. 2.22, on the left), it can be said that quartz is still the major phase at 1000 °C for all the grain sizes for 1 hour dwell time, with the exception of a small amount of cristobalite in the middle sample. Quartz is also still present (though in minor amounts) for a dwell time of 6 hours: here the major phase is cristobalite, with small amounts of tridymite (between 5 and 19 wt%).

The right half of the same figure (NaOH as mineralizer) shows that 1 hour dwell time with NaOH at 1000 °C gives approximately the same results of a dwell time of 6 hours with KOH. The differences between these two datasets can be found in the relative amounts of quartz and the high temperature phases: with NaOH, cristobalite becomes the major phase, quartz reduces its content (although with some differences among the samples) and tridymite starts to crystallize in a significant amount. The quantity of the remaining quartz is smallest for the finest sample, but there seems to be no relationship between the quartz content and the grain size: in fact, quartz initially grows and then decreases again, with the increment of <d>. However, if one looks at the sum of the high temperature phases, it is evident that the finest sample is the most reactive of the three in all the mineralizer/time associations, except the KOH/6hours combination. This observation can be well deduced also from Fig. 2.23.

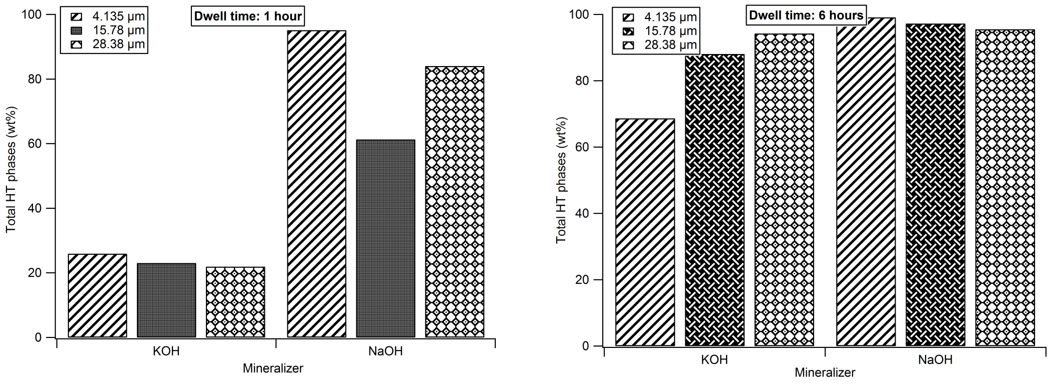

Figure 2.23: Influence of grain size and time at 1000 °C on the amount of total high temperature phases formed after heating. On the left, the data refers to 1 hour of dwell time; on the right, to 6 hours dwell time. Each left hand side of half figure shows results obtained when KOH is the mineralizing agent; each right hand side is relative to NaOH use.

By looking at the left hand side of Fig. 2.22, it can be said, as last consideration, that quartz is almost completely removed in all the samples, while tridymite becomes the major phase; cristobalite is always present at

10-18 wt%; the amorphous phase is nearly the same for all the grain sizes.

Fig. 2.24 shows again the influence of grain size as in Fig. 2.22, but the temperature in this case is 1200 °C. At this condition, it appears clear that quartz is almost completely absent in all the combinations time/temperature/grain size. There are no large differences in the phase ratios among the samples, but it can be said that the finest one has a smaller cristobalite content, in keeping with the fact that small grain sizes promote reactions, and so tridymite has time to grow at the expense of both quartz and cristobalite. Tridymite is the dominant phase in all the cases represented in the figure, followed by a still conspicuous amount of the amorphous phase, which does not differ so much from sample to sample, but is present in higher amount when the starting quartz is finer.

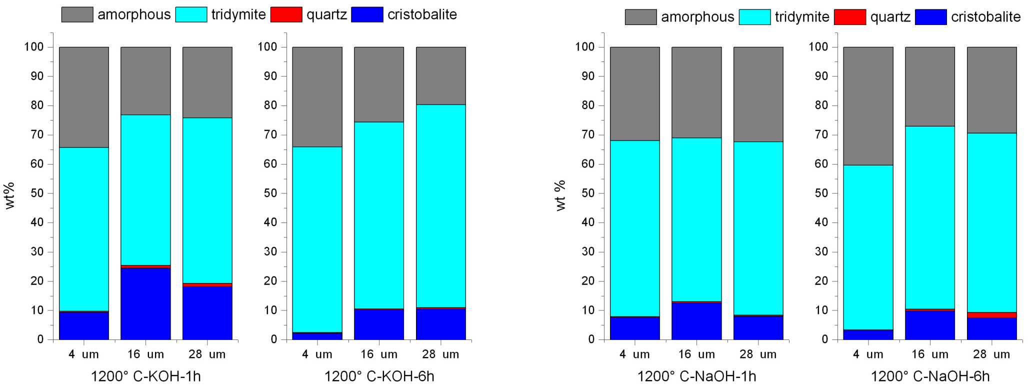

(a) KOH (b) NaOH

Figure 2.24: Influence of grain size and time at 1200 °C: the data are presented as a function of grain size in each graph, with KOH as mineralizer on the left half, and NaOH on the right half, and with 1 hour dwell time on the left hand side of each half, 6 hours dwell time on the right.

The amorphous phase

From the results expressed previously, further questions arise: Is the equilibrium reached for the samples fired at 1200 °C? Why is there still quite a large amorphous content, at that temperature? One would expect that, at the equilibrium, the amorphous phase would be absent or at least negligible, as the crystalline phases thermodynamically stable should have had the time to form. On the contrary, all the samples treated with a mineralizer and here investigated contain the amorphous phase, which ranges between 12 wt% and 45 wt% (look at Table 2.5). Fig. 2.25 displays the diffraction patterns of the fine sample (SA600 fired at 1200 °C for 6 hours, just as example) mixed with NaOH (in red), KOH (in blue) and distilled water (in green) (the latter is the wet sample studied in Section 2.2): the increased background for samples treated with a mineralizing agent proves the presence of the amorphous phase, which was not detected in the previous set of experiments (see the pattern of the wet quartz, which has a flatter background).

In order to check whether the amourphous content was due to lack of time for crystallization or to something else, a test was performed by changing the amount of mineralizer in the starting mixture, from a very small content to a very large one. This experiment was conducted on the finest sample (SA600), at 1000 °C and 6 hours dwell time, and Fig. 2.26, as well as Table 2.6, shows the results obtained.

The amorphous content relative to the use of 1.8 ml of solution, as is the case described until now, is very similar to that obtained from this new experiment (compare row 4 of Table 2.6 with rows 3 and 7 of Table 2.5, in the column relative to the 6 hours of dwell time), proving that the results discussed above are reproducible and that those represented here are reliable.

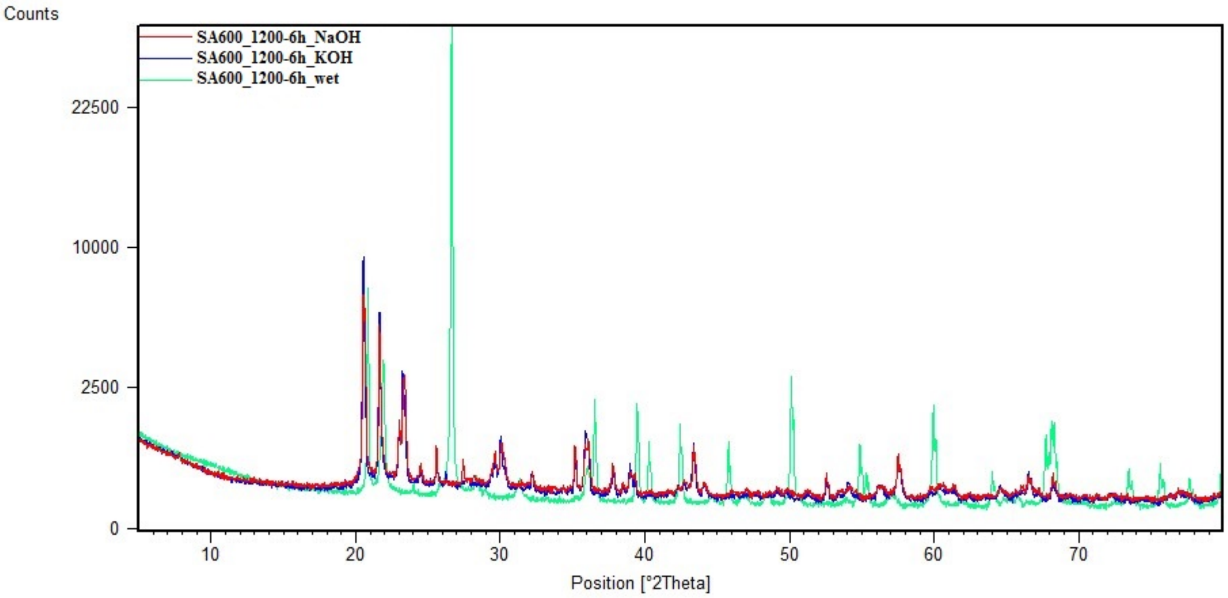

Figure 2.25: Comparison between the diffraction patterns of the finest sample (SA600) fired at 1200 °C for 6 h, with NaOH (red), KOH (blue) and distilled water (green), *i.e.* the wet sample studied in the first set of experiments (Section 2.2). It is clear the absence of the amorphous phase in the pure quartz sample as the background does not show the typical hump. On the contrary, the samples mixed with mineralizers display an increased background, proving the presence of amorphous material.

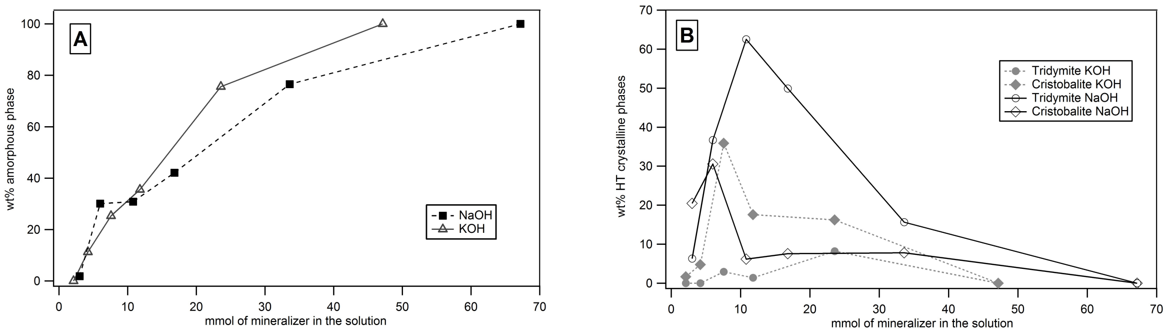

Figure 2.26: The amorphous content (A) and the amount of the high temperature crystalline phases (B) as function of mineralizer content. The lines between points are just guides for the eye.

Table 2.6: Results from the *ex-situ* experiment on sample SA600, treated at 1000 °C for 6 hours, with KOH and NaOH in different amounts.

Volume of solution (ml)	Amount of mineralizer (mmol)	Quartz (wt%)	Cristobalite (wt%)	Tridymite (wt%)	Amorphous phase (wt%)	Amount of mineralizer (mmol)	Quartz (wt%)	Cristobalite (wt%)	Tridymite (wt%)	Amorphous phase (wt%)
	KOH					NaOH				
0.50	2.11	98.35	1.65	0.00	0.00	3.00	71.41	20.46	6.30	1.83
1.00	4.21	84.00	4.80	0.00	11.23	6.00	2.72	30.54	36.68	30.06
1.80	7.58	36.00	35.90	2.94	25.28	10.80	0.51	6.16	62.50	30.84
2.80	11.79	45.00	17.60	1.38	35.54	16.80	0.44	7.56	49.90	42.10
5.60	23.58	0.00	16.23	8.20	75.57	33.60	0.00	7.82	15.64	76.53
11.20	47.15	0.00	0.00	0.00	100.00	67.20	0.00	0.00	0.00	100.00

From Fig. 2.26 A, it is clear that there is a direct relationship between the mineralizer content and the amount of amorphous material formed during the heating/cooling process: when the amount of mineralizing agent is too large, the obtained sample is totally amorphous, while smaller quantities of mineralizer end up in a totally crystalline mixture. Thus, the mineralizing agent stabilizes the thermodinamically unstable phase, that is the amorphous phase, and this is in agreement with Venezia et al. (2001), who found that alkali ions, such as Na^+ or K^+, promote the amorphous formation and produce very little amount of crystalline phases. However, if the mineralizer content is too small, the mixture is almost totally composed of quartz, so no high temperature polymorphs formed. In fact, from Fig. 2.26 A combined with Fig. 2.26 B, it is clear that small amounts of mineralizer result in a mixture containing quartz, as both amorphous phase and cristobalite and tridymite are present in very small quantities.

As the amount of mineralizer increases, it is evident that adding Na^+ is a much more efficient way to obtain tridymite with respect to adding K^+: with NaOH the maximum amount of tridymite formed is 62.50 wt%, while with KOH it is present at 8.20 wt%, but, in the latter case, the quantity of mineralizer needed is higher, thus leading to a larger amount of amorphous material. On the other hand, the maximum amount of cristobalite can be found for KOH as mineralizing agent: ∼36 wt% cristobalite is crystallized when KOH is used, ∼30 wt% with the addition of NaOH. The most favourable combinations, in term of the highest content of HT crystalline phases and the lowest of amorphous material, seems to be, at 1000 °C and 6 hours dwell time, the addition of 6-11 mmol NaOH (see Table 2.6 for the proportion of products).

2.3.2.2 *In-situ* results

After having studied the relationship between grain size, time, temperature, and amount and type of mineralizer with the *ex-situ* experiments, still the mechanism of stabilization of the high temperature phases by means of the adjunct of mineralizer was not completely understood, and to the best of the author knowledge, not present in the current literature. For this reason, an *in-situ* experiment has been performed, with the aim of mimicking the heating ramp to which the quartz sample was subjected to. Being the finest sample (SA600) the most interesting in terms of occurred reactions and of replacement of quartz, it was the one used in this kind of measurements. Heating ramps have been done in a narrow range from 1100-1200 K (depending on the mineralizer used) up to 1500 K and Fig. 2.27 shows the diffraction patterns obtained.

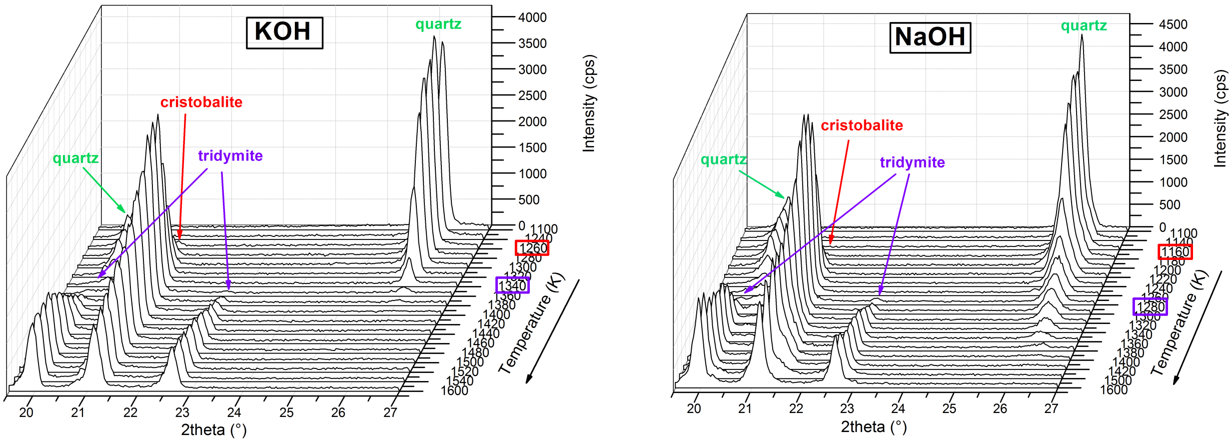

Figure 2.27: Heating ramps for sample SA600 wetted with KOH (left) and NaOH (right) aqueous solutions.

The elimination of quartz is evident from the disappearance of its peaks in the diffraction patterns collected at various temperatures (look especially at its main peak at 26.6° 2θ). In correspondence of the decreasing of quartz peaks, that of cristobalite (∼21° 2θ) appears and increases, until also tridymite forms (peaks at ∼20° 2θ and

∼22.5° 2θ): at that time cristobalite reduces, proving that tridymite crystallizes in despite of cristobalite, together with quartz. This sequence of phase transitions, which is opposite to that reported in the silica phase diagram, is observed when both KOH and NaOH are used as mineralizers; the only difference is the minimum temperatures of formation of cristobalite and tridymite, being them 100 °C less when the mineralizing agent is NaOH (∼1000 °C for KOH and ∼900 °C for NaOH). Thus the crystallization temperatures of HT polymorphs are lowered of 200-300 °C, if a mineralizer is added to pure quartz.

Because it was not possible, being this an high temperature experiment, to add an internal standard to evaluate the amount of amorphous material in the sample, the quantities of the crystalline phases are all overestimated of an unknown amount (the amorphous content is likely varying during the heating ramp). Therefore, it was not reasonable to do a full quantitative analysis of the samples during the heating stage, so the amount of the various crystalline phases have been estimated, at the various temperatures, by means of the area of one or more significant diffraction peak of the forming crystalline phases. Figure 2.28 shows the area of main peaks of quartz (circles), cristobalite (squares) and tridymite (diamonds) changing with increasing temperature.

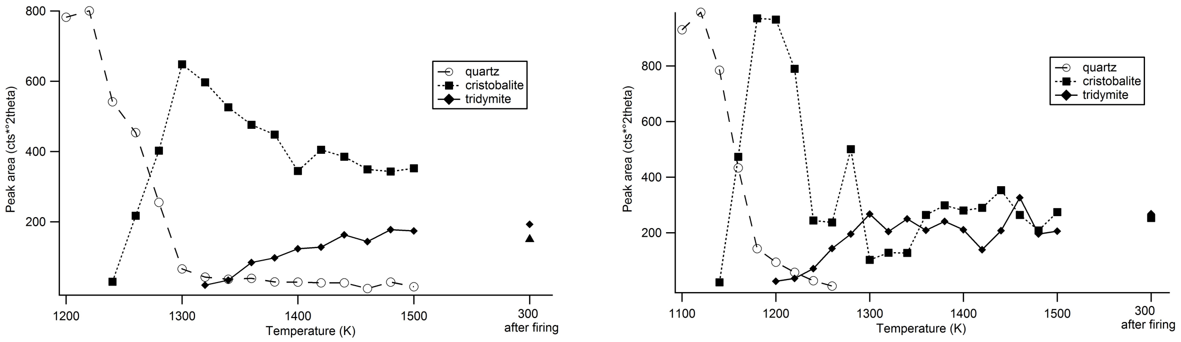

(a) KOH (b) NaOH

Figure 2.28: Evolution of peaks area during the heating ramp.

As confirmation of what already noticed qualitatively from Fig. 2.27, it stands immediately out that cristobalite is the first phase formed and that its amount starts decreasing after the appearance of tridymite. Quartz reduces when cristobalite crystallizes, its decrease becomes slower when tridymite starts to grow and, after the firing process, it is completely replaced by its two polymorphs, which are present in similar amounts. The use of NaOH as mineralizer, in particular, leads to a complete removal of quartz already at ∼1250 K. Tridymite and cristobalite formation is always promoted by NaOH, because reactions are faster (look at the slopes) and take place at lower temperatures. By the way, the use of any mineralizing agent decreases very much the crystalization temperature of cristobalite (about 300 °C), which was found to be about 1200 °C when pure quartz is treated (see Section 2.2).

The fact that tridymite is a product of the reduction of both quartz and cristobalite does not allow the tridymite crystallization to be studied from a kinetic point of view: all the phases present at high temperature are, indeed, intimately correlated, thus preventing separating all the effects and denying the possibility of focusing on the pure tridymite-cristobalite (or tridymite-quartz) phase transition.

2.3.3 Conclusions

The aim of this second investigation on quartz was to inspect the effects of mineralizing agents on silica phase transitions, in order to show the differences between the two method of sample preparation, *i.e.* with or without the addition of a mineralizing compound to the starting quartz powder. Attention has been paid also on the influence of quartz PSD and working temperatures and times.

From the discussion proposed above, it can be summarized that:

1. cristobalite forms first with respect to tridymite, which, in turn, crystallizes also at its expense, in keeping with literature and in contrast with the ideal sequence of HT silica phase transitions;
2. the mineralizers lower the crystallization temperature of cristobalite (compare with Section 2.2, which appears even at 900 °C when sodium hydroxide is added to the starting quartz (at ∼1000 °C if potassium hydroxide is used);
3. quartz can be almost completely removed (<∼3 wt%) at 1100 and 1200 °C, while the use of NaOH and of a smaller grain-sized quartz powder can reduce its amount more easily, even at lower temperatures (*e.g.* for SA600 mixed with NaOH and fired at 1000 °C for 6 hours, the remaining quartz is 0.86 wt%);
4. the quantity of HT phases formed after firing is controlled by kinetics;
5. on a quality level, it can be said that NaOH seems to induce a faster kinetics with respect to KOH, even though the induction time seems to be longer;
6. the amount of mineralizer influences the amorphous content, in a sense that the higher the quantity of mineralizer, the larger the amount of amorphous material, at least up to a certain saturation value;
7. a small grain size seems to produce more high temperature phases, even though the proportion between phases do not show any relevant relationship, and in keeping with the fact that the finer the particles the higher the reactivity (like in the previous Section).

2.4 Concluding remarks

The present Chapter illustrated the behaviour of industrially-used quartz powders when they were mixed with mineralizers, and when they were treated without any addition of chemical compounds. It is well known that the particle size reduction can induce stronger reactivities, so it was interesting to use different grain-sized starting powders for the experiments, in order to evaluate the effect of this promising factor. It has been shown that quartz PSD plays a crucial role in the cristobalite and tridymite formation: the finest the sample, the bigger the amount of the high temperature phases formed. Kinetics of quartz-cristobalite transition also shows a dependence on the grain size parameter: the kinetic exponent n, which depends on the mechanism involved, is in inverse proportion with <d>.

Moreover, it has been demostrated that the use of an alkali ion as mineralizing agent boosts the reactions, lowering the formation temperature of cristobalite. In particular, the most effective tested compound was found to be sodium hydroxide, which accelerates all the transformations and reduces the energy necessary to promote them, in terms of decreasing times and temperatures of firing process.

The results presented here, therefore, have important industrial implications: on the basis of the conclusions here reported, industries can, indeed, choose the most appropriate raw materials and the most convenient conditions to apply to their ceramic process, in order to obtain the best desired final product, and, at the same time, save energy, subject matter so relevant nowadays.

Part III

Functional ceramic materials

Chapter 3

Elasticity in perovskite phase transitions: the case of La$_{0.5}$Ca$_{0.5}$MnO$_3$

3.1 Introduction

3.1.1 Perovskite structure

The perovskite structure, named after the mineral perovskite CaTiO$_3$, is adopted by many compounds with the general formula ABO$_3$. The ideal structure is cubic (space group: *Pm*$\bar{3}$*m*; a = 3.901 Å), with A and B as cations (see Fig. 3.1). All the atoms in the lattice are on special positions within the unit cell: the A cation has fractional coordinates $(\frac{1}{2}, \frac{1}{2}, \frac{1}{2})$, the B cation is on the origin (0, 0, 0) and the oxygen atoms have coordinates $(\frac{1}{2}, 0, 0)$, $(0, \frac{1}{2}, 0)$ and $(0, 0, \frac{1}{2})$ (the structure can also be drawn with the origin on the A site instead). The A atom is at the centre of the cube and is coordinated to 12 oxygen atoms located at the midpoint of each cube edge. The B cation is in octahedral coordination with the neighbouring oxygen anions, and neighbouring BO$_6$ octahedra are joined at corners to form a network that runs throughout the entire crystal. In this ideal arrangement the ratio of the A–O to the B–O bond lenghts must be equal to $\sqrt{2}$.

When this condition cannot be met, the structure distorts by changing the shape of the octahedron (the cation moving off-centre) or by twisting the linkages between octahedra, and reduction in symmetry is a possible consequence. The ideal perovskite structure is, indeed, quite demanding in relation to the relative sizes of the A and B cations. However, at high temperatures, when there is more flexibility in the bonds and the atoms have greater vibrational amplitudes, the restriction on the ratio of A–O to B–O bond lenghts is relaxed to some extent. This means that, even if the cation sizes are not right, the structure can still be cubic at high temperatures, while at low temperatures it will have to distort to accomodate them.
The distortions of the perovskite structure are essentially three:

1. when the A cation is too small for the large 12-fold site, the octahedra tilt relative to one another, and so reduce the size of the A site. This is shown in Fig. 3.2, where the tilts, indicated by the semicircular arrows, are about an axis normal to the page. Adjacent octahedra tilt in opposite senses and are therefore no longer equivalent, as they were in the ideal cubic structure. Hence, the size of the unit cell is increased, while the symmetry reduces to tetragonal. The tilts can be also slightly out of plane, like in pure and doped CaTiO$_3$, and this distortion further reduces the symmetry to orthorhombic.

2. when the B cation is too small for the octahedral site, the cation moves off-centre within the octahedron. This is the case of BaTiO$_3$ (it does not occur as a mineral), which has the Ti atom, at temperatures below

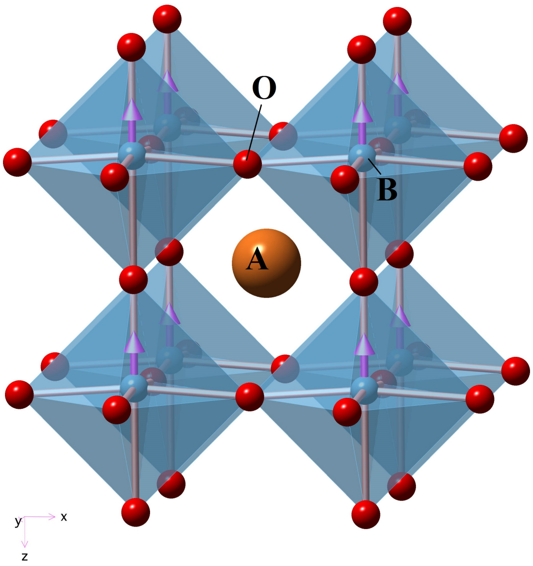

Figure 3.1: The ideal cubic structure of perovskite ABO_3, in which the corner-sharing BO_6 octahedra form a cube with the B atoms at the corners and A atoms at the centre.

120 °C, displaced very slightly from the centre of the octahedron towards an oxygen at one of the corners. This displacement (represented in Fig. 3.2 by the straight arrows) also very slightly distorts the octahedron, reducing the symmetry to tetragonal, but retaining the basic unit cell size. If these shifts are all in the same direction, there is a net movement of change resulting in a structure with a dipole moment; this spontaneous electrical polarization is termed *ferroelectricity*. The polarization can be affected by an applied electric field and this leads to considerable applications of perovskites in electronic devices.

3. when the A–O and/or B–O bonds have a pronounced covalency, this results in a distortion of the octahedron itself.

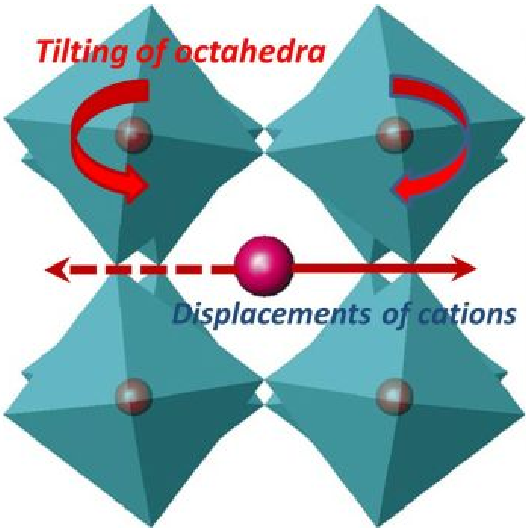

Figure 3.2: Two modifications of the perovskite structure: tilting of alternate BO_6 octahedra in opposite senses (semicircular arrows) and displacement of the B cations from the centre of octahedra (straight arrows). Figure taken from `http://www.physik.uni-siegen.de/fkp/masterworkprojects/twinning_project/?lang=de`.

Each kind of distortion may occur independently in a given compound, or in combination, leading to a great variety of different structural modifications depending on the sizes and the bonding character of the cations.

3.1.2 Structural and elastic properties of La, Ca manganites and aim of the project

A recent focus in materials physics has been on the functional properties of materials with multiple instabilities that involve combinations of ferro/antiferroelectric, ferro/antiferromagnetic and ferroelastic phase transitions. In multiferroics the aim is to induce a magnetic response by applying an electric field or a ferroelectric response by applying a magnetic field, in magnetoresistant materials a change in electrical resistivity is induced by a magnetic field and in magnetocalorics (or electrocalorics) the need is to induce thermal changes by applying a magnetic (or electric) field, etc. Behind these efforts is the aim to understand the mechanisms by which the different properties are interdependent so that required patterns of behaviour can be tuned through the choice of structure type, composition, grain size or, in the case of thin films, the choice of substrate.

In this context, perhaps the most universal mechanism is strain. Any change that occurs in a structure, whether due to ordering of magnetic moments, changes in electronic configuration or atomic displacements, is accompanied by some degree of lattice distortion. It follows, firstly, that strains which are common to two different ferroic properties in a single phase or in an intimate mixture of two phases will cause them to be coupled and, secondly, that the overall structural and thermodynamic behaviour must depend on the (relatively large) length scale of strain interactions rather than the (relatively short) length scale of interactions between magnetic or electric dipoles. The primary objective of the study presented in this Chapter was to use elastic and anelastic properties to characterize strain relaxation behaviour as a function of grain size, down to the nano scale, in the competition between ferromagnetic ordering and charge ordering of colossal magnetoresistant manganites.

Strain coupling phenomena can be investigated directly through determinations of lattice parameters and indirectly through their influence on elastic moduli. The elastic moduli are particularly sensitive measures because they represent susceptibility with respect to strain in a manner that is analogous to magnetic susceptibility with respect to a magnetic order parameter, and dielectric permittivity with respect to a ferroelectric order parameter. The half-doped La, Ca phase, $La_{1-x}Ca_xMnO_3$ with x = 0.5 (LCMO), was chosen for the present investigation because it lies in the range of temperature-composition space where the energetics of the charge ordered insulating phase (x > 0.5) and the La-rich ferromagnetic metallic phase (x < 0.5) are almost exactly balanced (Fig. 3.3). This balance is known to be tipped in favor of ferromagnetism when grain size is reduced to dimensions where strong magnetic dipole interactions can occur but cooperative Jahn-Teller distortions are reduced [Levy et al., 2000; Sarkar et al., 2008; Rozenberg et al., 2009; Jirak et al., 2010; Auslender et al., 2010; Lahiri et al., 2012]. On the base of the results described below, it can be argued that suppression of the charge ordered phase is due specifically to suppression of long range ferroelastic shear strain, even though local Jahn-Teller distortions of MnO_6 octahedra still occur. This is fundamentally different from the influence of homogeneous strain imposed by a substrate on a thin film because it will involve strain heterogeneity on a local scale within the nanocrystals.

Fig. 3.4 shows the stable structure (which is orthorhombic: space group: *Pnma*; a = 5.42 Å, b = 7.64 Å, c = 5.43 Å) of the material under study and highlights the distortion of the configuration of octahedra with respect to the ideal cubic structure (compare Fig. 3.4 B with Fig. 3.1).

The structural and magnetic behaviour of $La_{1-x}Ca_xMnO_3$ is well known. Bulk samples of $La_{0.5}Ca_{0.5}MnO_3$ undergo a charge ordering transition to an incommensurate structure at charge-ordering temperature (T_{co}) ~225 K which is driven largely by cooperative Jahn-Teller distortions [Radaelli et al., 1997; Mori et al., 1998b]. There is a marked hysteresis with respect to the temperature dependence of the superstructure repeat, which changes from incommensurate to commensurate near 130 K during cooling and near 180 K during heating [Radaelli et

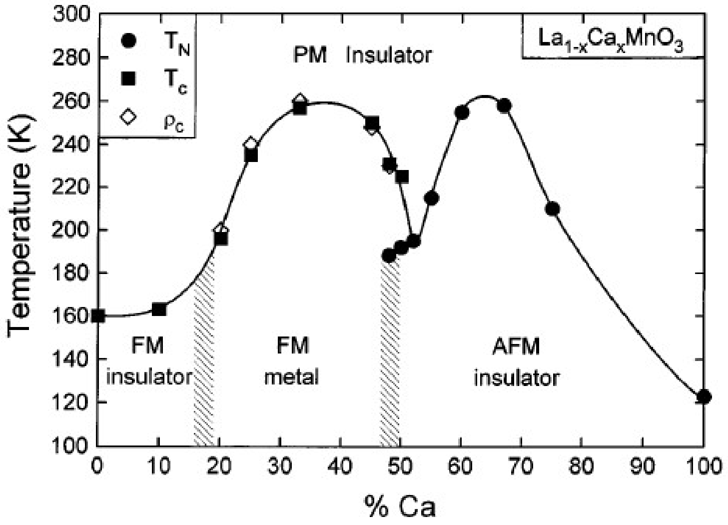

Figure 3.3: The phase diagram of $La_{1-x}Ca_xMnO_3$ as function of Ca content, built up from the study of Schiffer et al. (1995) and reported in the same paper.

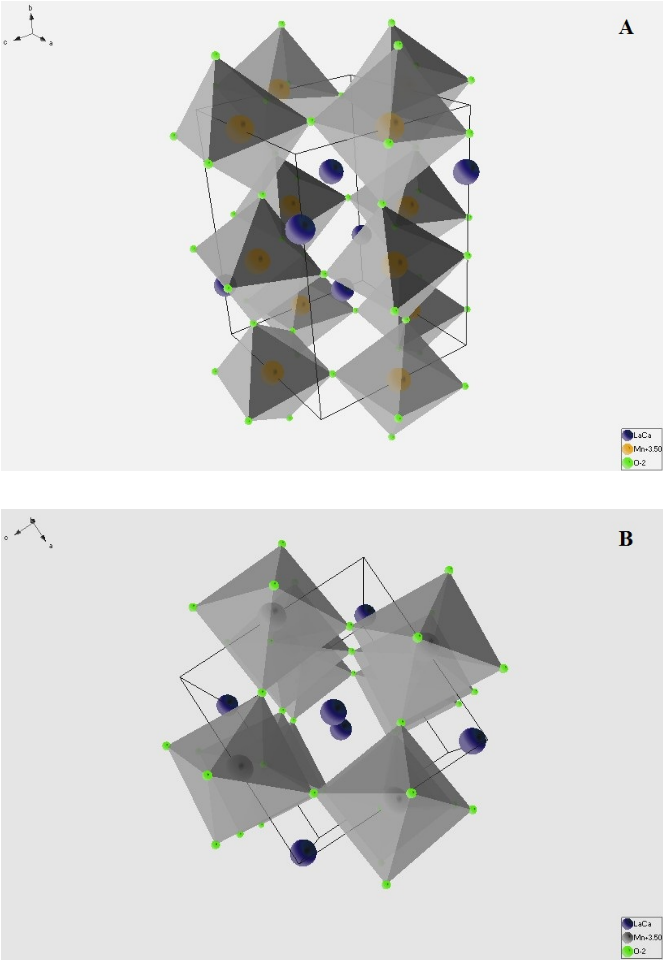

Figure 3.4: The orthorhombic structure of $La_{0.5}Ca_{0.5}MnO_3$. B shows the unit cell along c-axis, emphasizing the tilting of octahedra with respect to the cubic structure.

al., 1997; Chen & Cheong, 1996; Pissas & Kallias, 2003]. An antiferromagnetic ordering transition has its Néel point, T_N, near 160 K during cooling and near 190 K during heating in weak/zero field [Ramirez et al., 1996; Schiffer et al., 1995], *i.e.* almost coincident with the incommensurate–commensurate transition. The ground state is generally accepted as being an insulating, antiferromagnetically ordered, commensurate structure with some degree of charge order [*e.g.* Rodriguez et al., 2005]. Competition with the ferromagnetic metallic structure is reflected in the fact that there is invariably evidence for the presence of a second phase at all temperatures below T_{co}. In the range $T_{co} > T > T_N$, the coexistence is believed to be of ferromagnetic metal finely dispersed within a paramagnetic charge ordered insulator [Mori et al., 1998a & 1998b; Huang et al., 2000; Rivadulla et al., 2002; Loudon et al., 2002]. Below T_N the ferromagnetic phase remains but its volume fraction reduces substantially. By way of contrast, in nanocrystalline samples there is a transition directly from the high temperature paramagnetic structure to the ferromagnetic structure at $T_c \sim$ 250-260 K [Levy et al., 2000; Sarkar et al., 2008; Jirak et al., 2010; Auslender et al., 2010]. Essentially the same value of T_c has been reported also in other samples for which no information about grain size is given [*e.g.* Huang et al., 2000; Parisi et al., 2001; Trukhanov et al., 2002]. The ferromagnetic phase remains stable down to low temperatures and there appears to be no evidence for a change to antiferromagnetic order or the development of two phase mixtures. This magnetic and structural evolution is superimposed on the *Pnma* perovskite structure which has tilted octahedra over the entire temperature interval of interest. The crossover from charge order and antiferromagnetism to ferromagnetism seems also to be typical of the effect of reducing grain size in magnetoresistant manganites more generally [*e.g.* Jirak et al., 2010; Lahiri et al., 2012; Rao et al., 2005 & 2006; Biswas et al., 2005; Bingham et al., 2012; Chowdhury et al., 2013], and cooperative Jahn-Teller distortions become suppressed also in $\mathrm{LaMnO}_{3+\delta}$ ($\delta \approx 0.03$) [Ghosh et al., 2014].

Changes in bulk elastic moduli, as measured on ceramic samples of $\mathrm{La}_{0.5}\mathrm{Ca}_{0.5}\mathrm{MnO}_3$ at frequencies of 0.1-5.1 Hz [Zheng et al., 2002a; Chen et al., 2010], $\sim$7 MHz [Fujishiro et al., 2001 & 2006] and 10 MHz [Chen et al., 2010; Zheng et al., 2000 & 2001], all show softening from both high and low temperatures towards a single rounded minimum at a temperature between $\sim$220 and 230 K. This pattern appears to be independent of measuring frequency [Zheng et al., 2002a; Chen et al., 2010] and coincides with steep variations in lattice parameters that are indicative of the charge ordering transition [Radaelli et al., 1997; Huang et al., 2000; García-Muñoz et al., 1999]. The transition is also marked by an increase in acoustic attenuation which reaches a peak $\sim$10 K below the temperature at which the elastic moduli have their minimum values [Zheng et al., 2000; 2001 & 2002a]. By way of contrast, there appear to be no obvious variations in acoustic velocities, acoustic attenuation or lattice parameters associated with the antiferromagnetic ordering transition at lower temperatures. Thus it appears that strain/order parameter coupling in the system is dominated by contributions from the Jahn-Teller component of the charge ordering transition [Chen et al., 2007 & 2010; Zheng et al., 2000 & 2003; Li et al., 2002; Qian et al., 2005].

The weakness or absence of coupling between antiferromagnetic ordering transition and strain in $\mathrm{La}_{1-x}\mathrm{Ca}_x\mathrm{MnO}_3$ is confirmed by the lack of variation in lattice parameters or acoustic velocities near T_N in samples with x > 0.5 where the charge order and antiferromagnetic ordering transitions are more widely separated during both heating and cooling (*e.g.* compare lattice parameter and acoustic velocity data of Li et al. (2002) with Néel point measurements of Pissas & Kallias (2003)). In sharp contrast, there is detectable strain coupling associated with ferromagnetic ordering in samples with x < 0.5, though it is quite different in character. For example, the data of Radaelli et al. (1995) for $\mathrm{La}_{0.75}\mathrm{Ca}_{0.25}\mathrm{MnO}_3$ show a uniform reduction of all three orthorhombic lattice parameters below the Curie temperature (T_c) $\approx$ 240 K, signifying a volume reduction of $\sim$0.1% but little or no change in shear strain with respect to the parent cubic structure. This is synchronous with a metal–insulator transition and, although there is a significant elastic anomaly, the pattern is different from that associated with charge ordering. Acoustic velocity data for samples with x = 0.25, 0.3, 0.33 and 0.43 do not show the softening as $T \to T_c$ from above which characterizes proximity to a (zone-centre) Jahn-Teller driven instability, though there is stiffening immediately below T_c [Zhu et al., 1999a & b & 2000; Zheng et al., 2002b; Belevtsev et al., 2006]. The peak in acoustic loss is narrower and coincides with the minimum in acoustic velocity in these samples [Zhu et al., 1999a & b; Zheng et al., 2002b] signifying, also, a different loss mechanism.

For the present work, $La_{0.5}Ca_{0.5}MnO_3$ powders of Sarkar et al. (2008) with different grain sizes were pressed into pellets which, in turn, were used for measurements of elastic and anelastic properties by Resonant Ultrasound Spectroscopy (RUS). In order to distinguish between crystallite size and grain size, the samples have been reanalyzed by X-ray powder diffraction. New magnetic measurements on the RUS samples were obtained so as to allow correlations of anomalies in elastic and magnetic properties directly. Macroscopic strains have been analysed using lattice parameters for bulk and nanocrystalline samples from Sarkar et al. (2008) and, for a bulk sample including hysteresis, using the data of Radaelli et al. (1997).

3.2 Resonant ultrasound spectroscopy technique

Resonance techniques have been used to measure elastic properties in the laboratory since at least the 1920s [McSkimin, 1964]. They were confined to samples with rather unusual geometries, such as bars with length-to-diameter ratios of ten or more, because those were the only geometries for which it was practical to solve the associated forward resonance problem, *i.e.* the determination of the normal modes of a body by using the information on its physical features. Later researchers exploited spherical samples of isotropic materials, but limitations in computational resources and theories applicable only to rectangular geometry did not allow significant improvements. In 1991, Visscher et al. proposed the use of the Hamilton's principle approach to the calculation of vibrational modes, in order to compute the resonance frequencies of anisotropic elastic objects of arbitrary shape. This method turned out to be very successful, also because it was possible to attribute individual resonances to each particular geometry, so that the appeal for elastic resonance methods increased significantly. The advances in computing power and the availability of a large variety of algorithms and programming languages led to a more wide spread of resonance techniques, when elasticity studies are required, and one of the most straightforward experimental methods used nowadays in this field is resonant ultrasound spectroscopy.

RUS is largely used to study phase transitions, as it allows to determine the elastic/anelastic behaviour of a material as a function of temperature. In particular, it measures the frequencies, in the region of $\sim$0.1-2 MHz, of vibrational modes of a sample, which depend on its shape, density, dimensions and, indeed, on the symmetry of its elastic tensor (which is determined by the crystal symmetry). Experiments can be carried out at temperatures down to $\sim$5 K and up to $\sim$1800 K.

Rectangular parallelepiped with orthogonal faces is the usual and more appropriate geometry, as none of the resonances degenerates and so all modes can be observed individually. This shape is even better than a cube, not only because it is extremely difficult to produce an exactly cubic sample, but also and especially because a parallelepiped with significantly different edge lengths yields a spectrum with resonance peaks more widely distributed (and therefore easier to detect). Nevertheless, any shape is permitted.

The dimensions of a detectable sample range from few hundred microns and masses less than 100 μg, up to several cm and masses of several kg. Investigations can be carried out on single crystals, for which the absolute values of all independent elastic constants can be derived, or polycrystalline materials, for which the evaluation of bulk and shear moduli is the study of interest. The square of the resonance frequency, f, of any peak in a RUS spectrum scales linearly with the square of the effective elastic modulus (or combination of moduli) associated with that vibrational mode [Migliori & Sarrao, 1997]. Therefore, it is possible to see the form of the variation of

elastic constants directly from the variation of the resonance peaks measured as a function of temperature, without any data analysis. Variations in the *quality factor*, Q^{-1}, which is a measure of anelastic dissipation, can also be obtained from *in-situ* measurements at high temperatures. Even if the quality of spectra is relatively poor, such that absolute values of elastic moduli can not be obtained, it is still possible to use frequencies of individual peaks as indicators of changes in elastic properties with temperature (this criterion is the one used also in the study illustrated in the present Chapter).
As RUS is highly sensitive to cracks and flaws, it is also commonly used as a non-destructive technique for the detection of imperfections in materials during their production: collected spectra are compared to those of the "perfect" material and discrepacies can be highlighted.

3.3 Experimental

3.3.1 Sample preparation

The samples used in the investigation reported here are $La_{0.5}Ca_{0.5}MnO_3$ nanocrystals, synthesized with a polymeric (polyol) precursor technique and already studied by Sarkar et al. (2008).
In the synthesis process, high purity (>90%) $(CH_3COO)_3La\cdot 1.5H_2O$, $Ca(CH_3CO_2)_2\cdot H_2O$ and $(CH_3COO)_2\ Mn\cdot 4H_2O$ (provided by Sigma Aldrich) were dissolved in the desired stoichiometric proportions in acetic acid and water. An appropriate amount of ethylene glycol was also added, in order to help in forming a close network of cations from the precursor solution, and assist the reaction, enabling phase transformation at relatively low temperatures. This solution was heated until the sol was formed and then the gel was dried overnight at $\approx$150 °C. Pyrolysis was done at 350-450 °C, followed by a sintering at $\approx$650 °C to obtain the desired pure chemical phase. The procedure led to nanocrystals with a particle size of $\sim$15 nm, which were consequently used for making samples of larger size by heat treatment: they were sintered at different temperatures changing from 650 °C to 1300 °C and varying time periods (5-30 hrs). These different sintering times and temperatures contribute to particle growths to various sizes, making it possible to increase grain sizes as large as 3.6 μm. The measured particle sizes of these staring powders are reported in the second column of Table 3.1.

The second step of sample preparation was the sintering process, which was conducted using the High Pressure Field Assisted Rapid Sintering (HP-FARS) apparatus, situated at the Department of Chemistry of University of Pavia, Italy. During each sintering procedure, a little amount of powder was laid in a double stage die: an external graphite die case is connected to two electrodes in order to produce, by Joule effect, thermal energy to transfer to the internal silicon carbide punches which are kept in contact with the sample by two thin graphite gaskets. A shielded K-type thermocouple is inserted in the external graphite cylinder (fittingly pierced), in order to check the temperature of the system. The working principle of the technique lies in the application of a low-voltage high-intensity current together with a uniaxial load on the sample, so to obtain relatively highly dense pellets in very few minutes, and, at the same time, not to change significantly the particle dimensions. The reduction in grain growth is indeed achieved by applying lower temperatures, which are replaced by higher pressures by using an internal silicon carbide die (instead of a graphite one, which is usually present in the more common SPS instruments, as illustrated in Fig. 3.5). Further details concerning the HP-FARS procedure can be found in Anselmi-Tamburini et al. (2012) and Maglia et al. (2013), just as few examples. After the die case containing the powder was loaded in the apparatus, a moderate initial uniaxial pressure was applied and the temperature was increased up to the desired value. Once the wanted temperature was reached, the pressure was rapidly increased to the final value, kept constant for 5 minutes and then quickly released and the power was turned off. This procedure provides cylindrical pellets of 5 mm in diameter and 1 mm thick, with masses of $\sim$0.12 g. Pellet F was broken

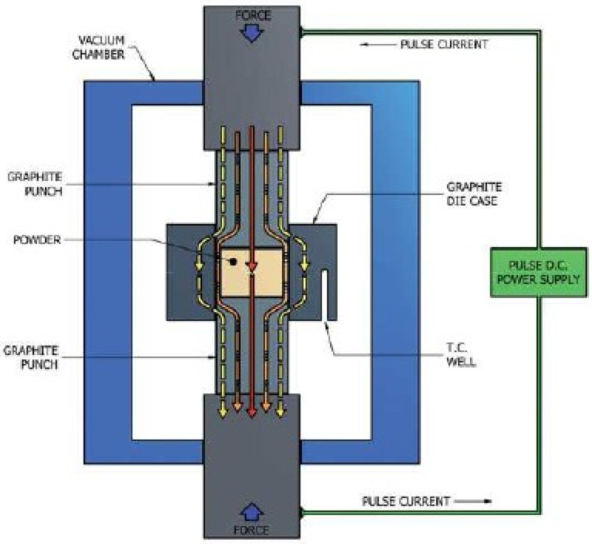

Figure 3.5: Configuration of HP-FARS. The apparatus used for the preparation of the samples studied here has an internal silicon carbide die, instead of the graphite one here illustrated.

Sample ID	Grain size of starting powders (nm)	Average crystallite size of sintered pellets (nm)	Sintering temperature (°C)	Sintering pressure (MPa)
A	15[a]	34(1)	800	504
B	43[a]	42(1)	800	489.6
E	600	75(1)	900	518.4
F	3660	136(3)	900	576

[a] These values refer to crystallite size.

Table 3.1: Sintering conditions for pellets prepared for RUS. Values of starting grain size are from Sarkar et al. (2008); crystallite sizes of sintered pellets are from x-ray diffraction data collected in the present study.

during depressurization and the piece used for experiments was about half of the disc (0.055 g). The sintering temperatures and pressures used for making the pellets are summarized in Table 3.1.

In order to compare the elastic behaviour of separated nanocrystalline grains with that of the hot pressed pellets, the same four starting powders that had been used for the hot pressed pellets were also mixed with CsI powder that had been dried at ~110 °C. Mixtures of 65 wt% CsI + 35 wt% sample powder for B, E and F and ~84 wt% CsI + 16 wt% powder for sample A were ground together by hand in an agate mortar and pestle and then mechanically pressed in an infrared pellet press to ~31 MPa. This produced discs 13 mm in diameter, ~2 mm thick and with mass ~1.17 g for B, E, F, and ~1.31 g for A. A pellet of pure CsI was also created, in order to eliminate its contribution from the data relative to the samples.

3.3.2 X-ray powder diffraction

In order to verify that the particle dimensions after sintering did not grow, the hot pressed pellets, already analysed through the other techniques used for this study, were reground in an agate mortar, so to conduct measurements by means of X-ray powder diffraction. The analyses were carried out using the θ-2θ Bragg-Brentano PANalytical X'Pert PRO diffractometer, already mentioned above (Fig. 2.7). Data were measured in the range 5-120° 2θ, with 0.0084° 2θ step size and 30 seconds/step; the divergence slit was fixed at 0.5°. The determination of crystallite size of each pellet was done using the MAUD program [Ferrari & Lutterotti, 1994] and the isotropic model, in order to separate the size effect from the microstrain contribution.

3.3.3 Resonant ultrasound spectroscopy

RUS spectra were collected from the hot pressed and the CsI pellets, *in-situ* at low temperatures, with the instrument present at the Department of Earth Sciences of University of Cambridge, UK (Fig. 3.6). The setup consisted of a standard RUS arrangement controlled by a Dynamic Resonance System (DRS) M3ODULUS II system. Each sample was held across its opposite faces without any bonding agents between two piezoelectric transducers coated in gold, one of which transmits the ultrasonic waves to the sample, and so drives it to resonate, and the other one detects the resulting signal. The RUS head (inset of Fig. 3.6) is made mainly of Tufnol composite G10/40 and is mounted on the end of a stick, which is inserted vertically into a standard Orange 50 mm helium flow cryostat, supplied by AS Scientific Products Ltd. A silicon diode and a LakeShore model 340 controller regulate and measure the temperature of the apparatus. Once the head with the sample mounted was lowered into the cryostat, the sample chamber was sealed, vacuum was pumped and liquid nitrogen was added to achieve temperatures as low as 100 K. The system was left to cool for several hours and, after that, liquid helium was added too, in order to cool down the system as far as 5 K. During this setup procedure, the sample chamber was held just below room temperature (280 K) to avoid cooling the sample suddenly, but, after cryogens had been added, it was filled with He gas to permit heat exchange between sample and cryostat.

Figure 3.6: Resonant ultrasound spectroscopy apparatus used for the elastic measurements. The inset at the top-left corner shows the head where the sample is located.

The hot pressed pellets under study were cooled in 30 K intervals from 280 K to 5 K with a 20 min equilibration time and then heated up again to 305 K in 5 K stages with the same settle time. Pellet F was investigated more deeply in the ranges of 265-190 K (every 5 K) and 20-60 K (every 2 K). RUS spectra were measured using DRS software at each step in the frequency range 0.05-1.2 MHz with 65,000 data points and were then transferred to the software package IGOR PRO for analysis. Frequency, f, and the width at half maximum height, Δf, of selected peaks were determined by fitting them with an asymmetric Lorentzian function. Acoustic resonances of a small

polycrystalline oxide sample are dominated by shearing rather than breathing motions and f^2 for the peaks scales closely with the shear modulus in most cases [*e.g.* Oravova et al., 2013]. Anelastic loss is characterized in terms of the inverse mechanical quality factor, Q^{-1}, as given by $Q^{-1} = \frac{\Delta f}{f}$.
Concerning the CsI pellets, RUS measurements were carried out from 290 to 140 K and back to room temperature, every 5 K, with 130,000 data points and the same frequency range and settle time used for hot pressed pellets. Again, data were transferred to IGOR PRO for the fitting analysis.

3.3.4 Superconducting quantum interference device system

Magnetic measurements on the four hot pressed pellets have been carried out using the MPMS-XL 7T Superconducting Quantum Interference Device (SQuID) magnetometer, at the Department of Engineering of University of Cambridge, UK. Each pellet was inserted in the middle of a straw which acts as sample-holder and this latter was placed inside the instrument.

The Quantum Design Magnetic Properties Measurement System (MPMS) is a device formed by two essential components: a superconducting magnet and a detection coil. The former is a solenoid constructed as a completely closed loop, so that it can be charged up to a specific current and then operate without the use of any external current source; the latter is a single piece of a superconducting wire, rolled in a set of three counterwound coils configured as a second-order gradiometer. These coils are located outside the sample chamber and in the midpoint of the magnet and are connected with the input coil of the SQuID, which is placed in a superconducting magnetic shield, some distance below the detection coils and the magnet. The configuration of a SQuID is illustrated in 3.7. As the sample moves through the coils along their symmetry axis and the magnet applies a DC magnetic field to the sample, the magnetic dipole moment of the sample induces an electric current in the detection coils. The SQuID functions as a detector of these variations in the current and so gives information exactly on the magnetic flux in the sample, as it is proportional to the current. A thermometry is installed in close proximity to the sample within the sensitive coil detection region, so that measurements under extreme temperature changes can be possible. For a deeper and more detailed explanation of the technique, see McElfresh et al.

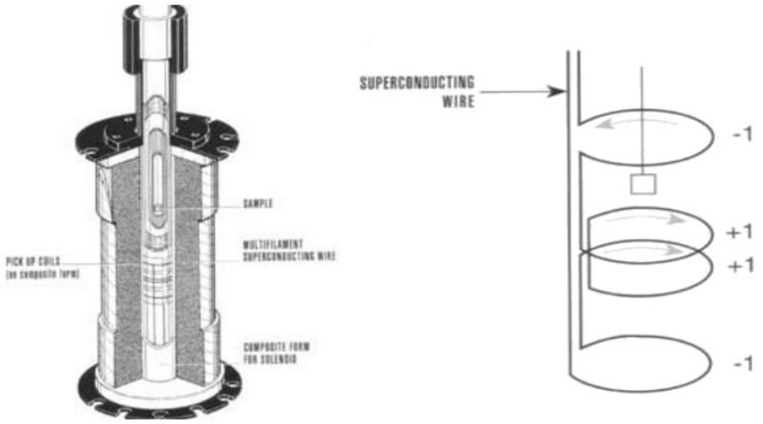

Figure 3.7: Configuration of SQuID. Figure taken from McElfresh et al.

In the present study, SQuID measurements were conducted collecting data in two different ways: firstly, the magnetic moments were determined in nominally zero field and in a 5 T field during both cooling and heating in the range 5-300 K every 0.01 K; after that, the magnetic moments were measured in hysteresis loops, with 0.03 kOe intervals between +3 and -3 kOe at temperatures of 300, 250, 200, 150, 75 and 5K in a cooling sequence.

3.4 Elastic theory

Differences in lattice parameters between bulk and nano samples of $La_{0.5}Ca_{0.5}MnO_3$ reflect differences in the spontaneous strains associated with octahedral tilting, charge ordering and magnetic transitions. Two characteristic shear strains may be defined in terms of the lattice parameters of the *Pnma* structure, a_{Pnma}, b_{Pnma} and c_{Pnma}, with respect to the lattice parameter of the cubic reference structure, a_0, (following Carpenter et al. (2001), McKnight et al. (2009) and Carpenter (2007)):

$$e_{tx} = \frac{1}{\sqrt{3}}(2e_1 + e_2 + e_3) = \frac{1}{\sqrt{3}}\Big(2\Big(\frac{\frac{b_{Pnma}}{2} - a_0}{a_0}\Big) - \Big(\frac{\frac{a_{Pnma}}{\sqrt{2}} - a_0}{a_0}\Big) - \Big(\frac{\frac{c_{Pnma}}{\sqrt{2}} - a_0}{a_0}\Big)\Big) \tag{3.1}$$

$$e_4 = \Big(\frac{\frac{a_{Pnma}}{\sqrt{2}} - a_0}{a_0}\Big) - \Big(\frac{\frac{c_{Pnma}}{\sqrt{2}} - a_0}{a_0}\Big) \tag{3.2}$$

where the value of a_o can be taken as $(\frac{a_{Pnma}b_{Pnma}c_{Pnma}}{4})^{\frac{1}{3}}$. Variations of these shear strains as a function of temperature are shown in Fig. 3.8 for samples A and F, using original lattice parameter data of Sarkar et al. (2008). For comparison, shear strains for bulk samples have been added using the lattice parameters given by Radaelli et al. (1997). These reproduce the substantial differences in structural evolution between the nanocrystalline sample A and the more coarsely crystalline sample F already reported by Sarkar et al. (2008), but also show differences between sample F and the bulk sample of Radaelli et al. (1997). In particular, the onset of changes in e_{tx} occurs at a lower temperature during heating of sample F than in the bulk sample, and there is an additional anomaly in e_4 at ∼130 K. Unpublished high resolution neutron powder diffraction data of Chatterji and co-workers from sample F do not show the anomaly in e_4 and show the intensity of antiferromagnetic ordering reflections decreasing to zero at ∼155 K. For present purposes, it is assumed that sample F has properties that are intermediate between the nano and bulk materials, consistent with the new determination of crystallite size as ∼136 nm (Table 3.1).

The lattice parameter data of Sarkar et al. (2008) are not of sufficient resolution to determine the evolution of volume strains because they are substantially smaller than the shear strains. Some idea of their likely magnitude and sign is given by data for other sources, however. For $Pr_{0.48}Ca_{0.52}MnO_3$ there is a small but significant positive volume strain of up to ∼0.002 accompanying charge ordering [Carpenter et al., 2010]. On the other hand, ferromagnetic ordering in $La_{0.75}Ca_{0.25}MnO_3$ is accompanied by a negative volume strain which, from the data in figure 1 of Radaelli et al. (1995), is estimated to reach ∼–0.002. The antipathetic relationship between ferromagnetism and charge order/orbital order must at least be enhanced by the opposite sign of these volume strains.

3.5 Results

Different experiments were carried out in order to check the crystallite size of LCMO pellets and to investigate the evolution of elastic properties and the phase transitions occurring at low temperatures in each sample. So, this Section is separated into three parts: the sample characterization, the outcome obtained from RUS measurements and the results coming from magnetic data collections.

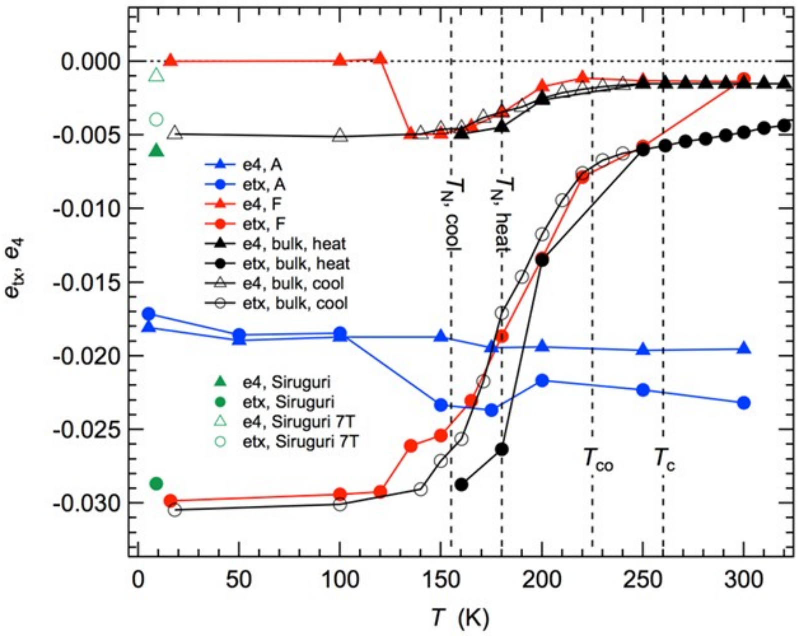

Figure 3.8: Variation of shear strains, e_{tx} and e_4, with respect to a parent cubic lattice determined using lattice parameter data for samples A and F from Sarkar et al. (2008) and for a bulk sample from Radaelli et al. (1997). (The data of Sarkar et al. were collected during heating). Also shown are values of transition temperatures for bulk samples (T_N, T_{co}) and for nano samples (T_c). Uncertainties propagated from uncertainties in the lattice parameters are estimated as $\pm \sim 0.001$. Data shown at 9 K are from lattice parameters of Siruguri et al. (2013).

3.5.1 Sample characterization through XRPD

Diffraction patterns obtained from XRPD experiments are illustrated in Fig. 3.9: as expected, they contain only peaks of the orthorhombic perovskite. Table 3.1 shows the particle size of the sintered pellets, determined by Rietveld analyses [Rietveld, 1969 & 2010]. Similar crystallite sizes to those reported by Sarkar et al. (2008) were obtained for samples A and B but much smaller sizes were obtained for samples E and F. The good agreement for the fine grained samples is due to the fact that the same method was used (*i.e.* powder diffraction line broadening). However, Sarkar et al. used transmission electron microscopy to measure grain sizes of the coarser samples, and grains observed in this way were presumably composed of aggregates of smaller crystallites or affected by grain mosaicity. What is important here is that hot pressing did not change the crystallite size of the hot pellets in a significant way (they remained in the nano range).

3.5.2 RUS analysis

All the studied discs were found to give measurable resonance spectra when placed with their large flat faces in contact with the transducers.

Figs. 3.10 and 3.11 show two representative sections of the RUS spectra collected from sample F (taken as example): the former was obtained during heating from hot pressed pellet, the latter during both heating and cooling from pellet containing also CsI.

As illustrated by Fig. 3.11, a characteristic feature of all spectra collected in this way is hysteresis, such that the pellet is elastically slightly softer during heating than during cooling. This is believed to be due to some relaxation of grain boundaries between the two phases in the pellets, but does not detract from the internal consistency in the sense that the influence of the sample powder can be clearly seen in both the cooling and heating sequences.

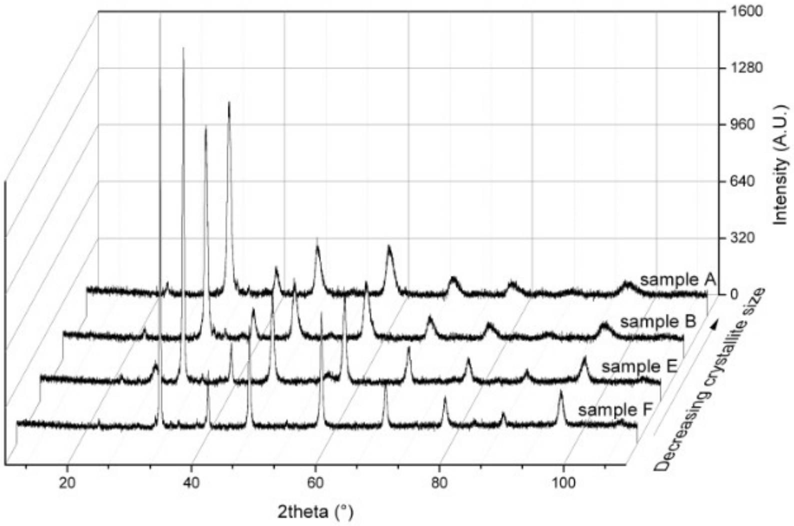

Figure 3.9: X-ray powder diffraction patterns from reground portions of the four hot pressed pellets.

Fig. 3.11 shows resonance peaks which have the same break in trend near 225 K that is seen in spectra from the hot-pressed pellets. Fig. 3.10 also displays a second break in the evolution of peak positions at 40 K.

Fig. 3.12 contains data for f^2 (left axis) and Q^{-1} (right axis) extracted from fitting of selected RUS peaks in spectra from the hot pressed pellets. For comparative purposes, f^2 values for a given peak have been scaled with respect to the value at ~290 K. Also shown are data from Zheng et al. (2000) for the square of shear wave velocities measured at 10 MHz by the pulse-echo technique and from Zheng et al. (2002a) for the shear modulus measured at 1 Hz using the forced vibration method. (Grain sizes were not specified for the samples used in these studies). These have been scaled so as to overlap with the RUS data above T_{co}, which is taken as the literature value, 225 K. The square of shear wave velocities scales with the shear modulus and resonance frequencies from RUS are expected to be determined predominantly by the shear modulus, so the data should be directly comparable. All show the same softening as T_{co} is approached from above, followed by stiffening with further decreasing temperature, though the amount of stiffening differs. Data for attenuation of shear waves at 10 MHz [Zheng et al., 2000] are shown as a dotted line, scaled with respect to data for Q^{-1} just above T_{co} in the case of sample F. These have a peak in acoustic loss just below T_{co} that is not reproduced in the RUS data.

Stiffening of sample F below T_{co} is less than shown by the 10 MHz ultrasonic data but comparable in magnitude to the stiffening reported for 1 Hz. The f^2 data have breaks in slope near 90 K and 40 K and little, if any, hysteresis between cooling and heating. Q^{-1} has a very slight increase below T_{co} that appears to be reproducible between separate resonance peaks. There is then a maximum in Q^{-1} at ~85 K and a second small peak near 40 K. The increase in f^2 and the loss peak at ~85 K have the form expected of a typical Debye-like relaxation process. The break in slope of f^2 near 40 K involves a reduction in the rate of stiffening with falling temperature, however, which is more likely to be indicative of strain coupling to some structural, magnetic or electronic transition. This differs from the peak in attenuation of transverse ultrasonic waves at 10 MHz which occurs immediately below T_{co}. Zheng et al. (2002a) do not show acoustic loss behaviour specifically for a sample with x = 0.5, but their data for x = 0.55 and x = 0.8 show a loss peak immediately below T_{co} which reduces in magnitude steeply between 0.1 and 5 Hz.

Stiffening below T_{co} in samples A and B is markedly different from that shown by sample F. There is a rounded minimum slightly below T_{co} and then a slight and approximately linear recovery with falling temperature. Q^{-1} values are generally higher for all resonances and again there is no reliable evidence for changes in acoustic

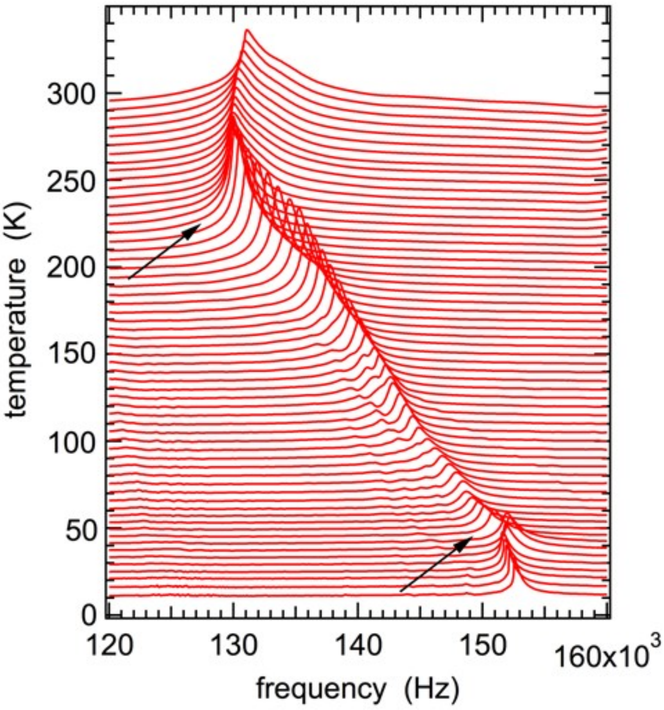

Figure 3.10: Segments of RUS spectra collected from sample F during heating. The y-axis is amplitude from the detector transducer but the spectra have been offset in proportion to the temperature at which they were collected and the axis then labeled as temperature. Breaks in the evolution of peak positions with temperature, indicated by arrows, occur near 225 K and 40 K.

loss between 290 and 90 K. It was not possible to follow resonance peaks down to the lowest temperatures in spectra from sample A but for sample B there is definitely a temperature interval between ~80 and ~50 K where the resonance peaks became significantly broader. Q^{-1} values decreased below ~50 K but did not show overt evidence for any anomaly near 40 K. The evolution of f^2 for sample E is more nearly the same as that of sample F than of samples A and B, in which the data show a more distinct break in slope at T_{co}.

It is not clear whether there is any dispersion with respect to frequency. f^2 data for different resonance peaks in the case of sample F scale closely together, consistent with their common dependence predominantly on the shear modulus. Variations of f^2 for different peaks in spectra from samples A and E show more spread below T_{co} when they are scaled to the same room temperature values and the anelastic losses are higher, but there does not seem to be a systematic trend of increasing or decreasing stiffness with measuring frequency. At least part of the differences may be due to differences in the proportion of a breathing component, dependent on the bulk modulus, involved in the relevant normal modes of the samples. Only in the case of sample E does there appear to be an anomaly in the vicinity of T_c (82 and 110 kHz modes).

Fig. 3.13 shows f^2 and Q^{-1} data from the CsI pellets. f^2 values for a single peak from each set of spectra collected during heating, scaled with respect to their values at ~290 K. CsI by itself has a linear reduction in the effective shear modulus with increasing temperature and the pellets containing ~1.17 g of the powders of samples B, E and F, ~1.31 g of the powder of sample A have trends which deviate from this. The form of the deviations closely matches the patterns seen for the hot-pressed pellets, again indicating that the hot pressing process does not modify the elastic properties significantly. In particular, the pellet containing sample A gives a small and rounded degree of softening with respect to CsI alone. The pellet containing sample B displays the same form of softening, while the pellets containing samples E and F give relative softening and stiffening with an obvious break in slope

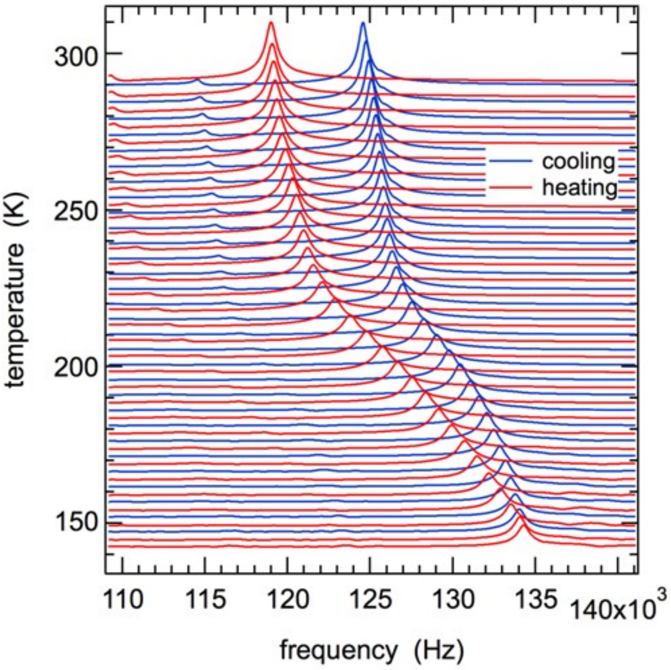

Figure 3.11: Segment of the RUS spectra collected from a pellet consisting of CsI and powder of sample F, in the proportions given in the text. The y-axis is amplitude from the detector transducer but the spectra have been offset in proportion to the temperature at which they were collected and the axis then labeled as temperature. The same difference between heating and cooling occurs for all pellets prepared in this way but the trend of peak frequencies clearly shows the same break in slope near 225 K as seen in Fig. 3.10 for the hot-pressed pellet.

in the vicinity of T_{co}. The loss behaviour must depend, in part at least, on grain contacts in the CsI pellets but the temperature dependence of Q^{-1} down to ~140 K does not show any gross features, apart from a slight increase immediately below T_{co} in the case of samples E and F.

3.5.3 Magnetic analysis

Fig. 3.14 shows data for magnetic moment during cooling and then heating in zero field and at 5 T. The magnetic properties of samples A and B are closely similar, consistent with the determination of crystallite size (34 and 42 nm, respectively). Both show patterns of evolution expected for a paramagnetic–ferromagnetic transition, with slight hysteresis, and only a further additional small anomaly near 42 K. If the small hysteresis is not due to thermal lag in the instrument, values of T_c for cooling and heating at zero field would be ~268 and ~284 K for A and ~270 and ~278 K for B, as estimated from the expanded view shown in Fig. 3.14 c. Both at zero field and under the influence of a 5 T field, there are irregularities in the magnetic moment at temperatures between 300 and 150 K during cooling but these are not present during heating (Fig. 3.14 a and b). Sample F (136 nm) does not show the characteristic pattern of ferromagnetic ordering followed by a ferromagnetic–antiferromagnetic transition reported elsewhere for bulk samples in either zero field or in an applied field [*e.g.* Levy et al., 2000; Schiffer et al., 1995; Radaelli et al., 1995; Ramirez et al., 1997; Granado et al., 1998; Freitas et al., 2002; Kallias et al., 2000]. Instead it appears to have a paramagnetic–ferromagnetic transition near 260 K in zero field (T_c ~257 K during cooling and ~262 K during heating, as estimated from Fig. 3.14 c), followed by a very obvious hysteresis pattern with limits of ~45 and ~155 K which is perhaps analogous to the hysteresis between limits of 125 and 180 K that is attributed to the ferromagnetic–antiferromagnetic transition in bulk samples [*e.g.* Levy et al., 2000; Freitas et al., 2002]. The characteristic pattern for bulk samples involves lower moments due to the antiferromagnetic structure,

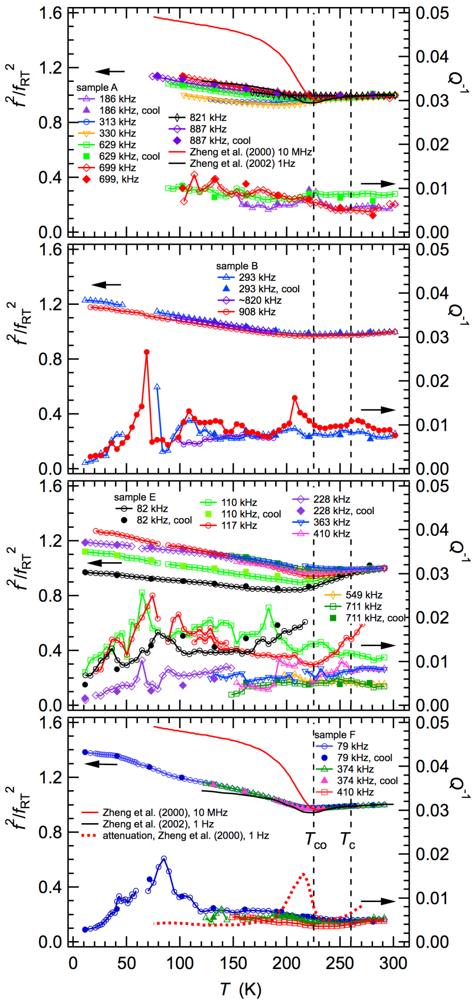

Figure 3.12: Variations of f^2 and Q^{-1} from selected peaks in spectra from hot-pressed pellets of samples A, B, E and F. The f^2 data are all scaled to 1 at ∼290 K. Values of the frequency at room temperature for each resonance peak are indicated in the captions. Data for the velocities of transverse ultrasonic waves at 10 MHz are reproduced from figure 1a of Zheng et al. (2000) and for the shear modulus at 1 Hz from figure 1 of Zheng et al. (2002a); both sets are also scaled with respect to their values at ∼290K. Attenuation at 10 MHz [Zheng et al., 2002a], scaled with respect to Q^{-1} data above T_{co}, is shown in the plot for sample F. Broken vertical lines indicate values of T_{co} (225 K) and T_c (260 K) taken from literature.

however, while sample F has consistently increasing moment with falling temperature. There is a further increase in moment near 42 K, as opposed to the decrease seen in zero field data for samples A, B and E. Sample E (75 nm) has variations different from those of A, B, F, but still with a trend consistent with a paramagnetic–ferromagnetic transition near 270 K in zero field (T_c ∼267 K during cooling and ∼275 K during heating, estimated from Fig. 3.14). Details of the anomaly near 42 K are considered below (Fig. 3.16).

Fig. 3.15 shows hysteresis curves for samples A, E and F. Data for sample B are not shown as they are closely similar to those of sample A. Both sets are consistent with paramagnetism at 300 K and ferromagnetism at $T \leq$ 250 K. Sample F appears to be paramagnetic at 300 and 250 K, but the pattern at 5 K is more nearly typical of ferromagnetism, though saturation magnetization is not reached at 3 kOe. At intermediate temperatures (200, 150, 75 K) the loops also remain open, which is suggestive of metamagnetic transitions and/or the response of a mixture of phases with different magnetic properties. Typical paramagnetic behaviour of sample E is limited to 300 K. At 250, 200 and 5 K the forms of the hysteresis curves are consistent with ferromagnetism, while the loops remain

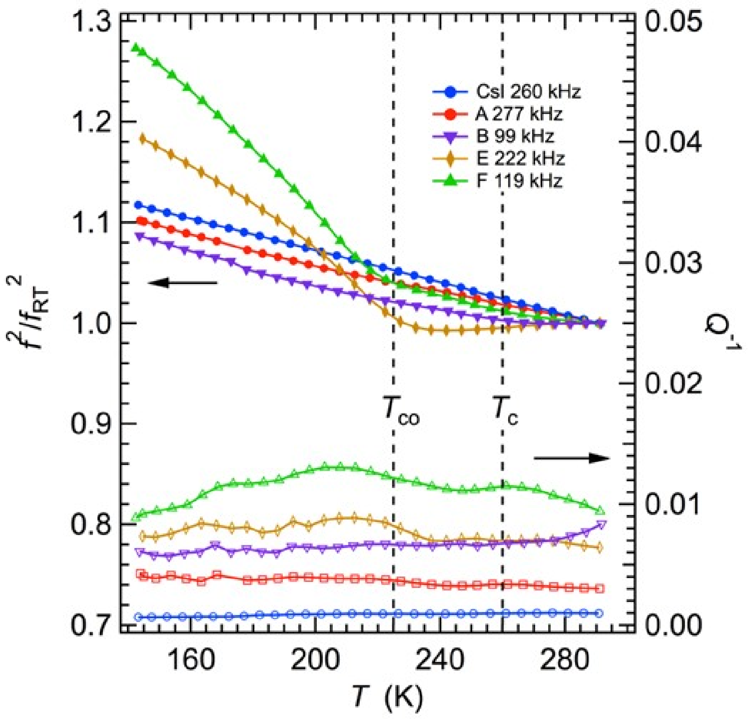

Figure 3.13: Data extracted from fitting of selected peaks in spectra collected during heating from ~140 K for a pure CsI pellet and pellets containing mixtures of CsI and sample powder. f^2 values are shown scaled with respect to their values at room temperature and the actual room temperature frequencies are given in the legend.

open to high fields at 150 and 75 K.

Fig. 3.16 shows details of anomalies in magnetic and acoustic properties at temperatures close to 40 K. The moments of A, B and E in zero field show a decrease with falling temperature that differs by ~3-5 K between heating and cooling. For sample F there is little or no hysteresis, the step is of increasing rather than decreasing moment with falling temperature, and there is a distinct peak in Q^{-1}. If there is an anomaly in the acoustic loss for the other samples it is below the level of noise in data. At 5 T, there is still an anomaly in moment near 40 K but it is more nearly in the form simply of a break in slope. There appears to still be a hysteresis in the data for A and B a few degrees above this, however.

3.6 Discussion

The working hypothesis for the present study was that reducing grain size to the nano scale for materials with structural phase transitions leads, primarily, to suppression of macroscopic strain and that this will be evident from suppression of elastic anomalies. In the case of quartz, a single order parameter gives rise to a co-elastic structural phase transition and the outcome is expected to be a reduction in the magnitude of the accompanying elastic softening. The onset of this occurs in ceramic samples with grain sizes of ~50 and ~65 nm [McKnight et al., 2008]. For $La_{0.5}Ca_{0.5}MnO_3$ the change from elastic properties which are similar in form to those of a bulk sample also occurs between ~75 nm (sample E) and ~40 nm (sample B). However, the transformation behaviour of $La_{0.5}Ca_{0.5}MnO_3$ is more complex than that of quartz because of the involvement of multiple order parameters, each of which has the capability to couple separately with strain.

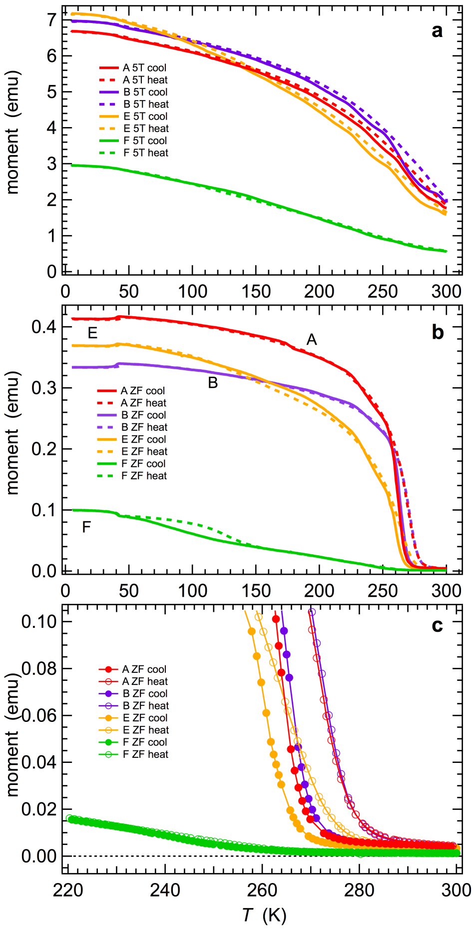

Figure 3.14: Magnetic moments of the pellets used for RUS measurements, as measured in zero field during cooling and then heating, followed by measurements in a 5 T field, again cooling followed by heating. Note that sample F had about half the mass of samples A, B and E. (c) is an expanded view of (b) in the temperature interval 220-300 K.

3.6.1 Strain/order parameter coupling

As set out in detail in Carpenter et al. (2010a & b), with respect to *Pnma* as the parent space group the order parameter for the commensurate structure of half-doped manganites transforms as the irreducible representation (irrep) X_1. This has two components, such that (a, 0) gives the *P*2_1*/m* structure and (a, a) gives *Pnm*2_1. The transition would be improper ferroelastic or co-elastic, respectively. However, treatment in terms of a single order parameter conceals the separate contributions which might develop from charge ordering, cooperative Jahn-Teller distortions and octahedral tilting. With respect to a parent cubic structure with space group *Pm*$\bar{3}$*m* these transform as Σ_2 (charge order), M_2^+ and Γ_3^+ (cooperative Jahn-Teller), M_3^+ and R_4^+ (octahedral tilting). Shear strains e_{tx} and e_4 couple with each order parameter component, q, as set out in Eqs. 10 and 11 for *Pnm*2_1 in Carpenter et al. (2010b). Coupling of e_{tx} with the Γ_3^+ order parameter is bilinear, *i.e.* with the form $\lambda e_{tx} q$ where λ defines the coupling strength, and the other couplings are linear quadratic, *i.e.* $\lambda e q^2$ (see Subsection 1.3.2.2). With respect to anomalies of shear elastic constants, the linear-quadratic contributions will give a stepwise softening below the transition point (improper ferroelastic or co-elastic), while the bilinear term will give non-linear softening as the transition point is approached from both above and below (pseudoproper ferroelastic) [Rehwald, 1973; Luthi & Rehwald, 1981; Fleury & Lyons, 1981; Carpenter & Salje, 1998]. From Fig. 3.8 it is clear that the dominant strain in coarse grained samples is e_{tx} and from Fig. 3.12 it is clear that the dominant softening mechanism has the form

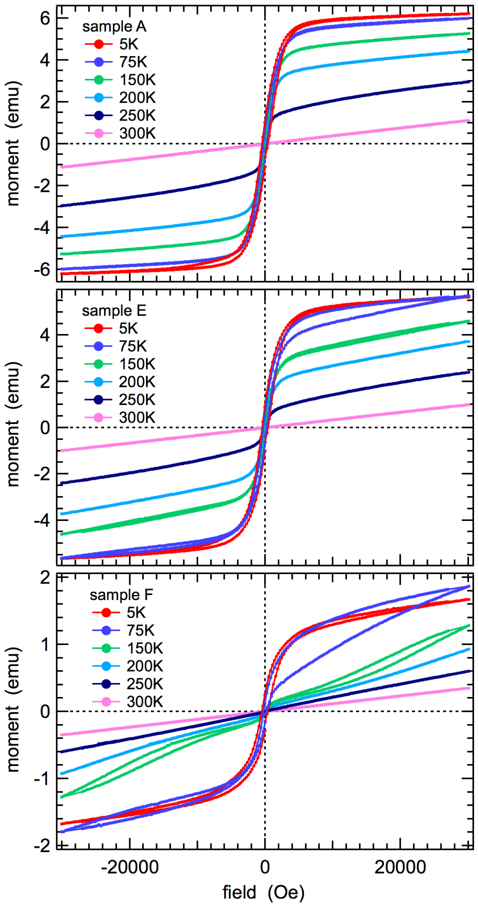

Figure 3.15: Hysteresis loops for samples A, E and F, measured in steps of 0.03 kOe. Data for sample B (not shown) are very closely similar to those of sample A.

expected for a pseudoproper ferroelastic transition. The dominant spontaneous strain must therefore be due to the bilinear coupling between e_{tx} and the Γ_3^+ order parameter which gives elastic softening of the form

$$(C_{11} - C_{12}) = (C_{11}^0 - C_{12}^0)\Big(\frac{T - T_{c\Gamma}^*}{T - T_{c\Gamma}}\Big). \tag{3.3}$$

$T_{c\Gamma}^*$ is the transition temperature for a transition driven by the order parameter and is related to the unrenormalised critical temperature according to (from Carpenter et al., 2010a)

$$T_{c\Gamma}^* = T_{c\Gamma} + \frac{\lambda^2}{a\frac{1}{2}(C_{11}^0 - C_{12}^0)}. \tag{3.4}$$

In Eqs. 3.3 and 3.4, λ is the coefficient for the bilinear coupling term, a is the coefficient for the second order term in a Landau expansion (Eq. 1.73) and $(C_{11}^0 - C_{12}^0)$ is a shear elastic constant for the cubic parent structure without influence from the phase transition. The shear modulus depends also on other shear elastic constants, specifically C_{44} in the case of a cubic phase, but the bulk modulus is expected to display a step wise softening due to linear quadratic coupling of volume strain with any of the order parameters, as shown schematically in figure 1 of Carpenter et al. (2010a). Eq. 3.4 has the same form as derived from consideration of Jahn-Teller theory, and

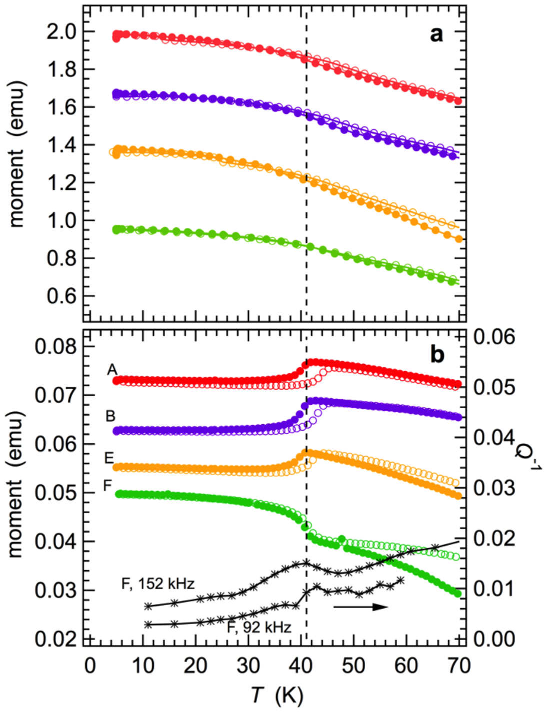

Figure 3.16: Details of magnetic moment (from Fig. 3.14) and Q^{-1} (sample F, black stars) in the vicinity of 40 K. The magnetic moment data have been shifted along the y-axis by arbitrary amounts to allow easy comparison between them. Filled symbols are data collected during cooling; open symbols represent data collected during heating. The vertical dashed line has been put at 41 K. (a) 5 T. (b) Zero field. In zero field, the moments for samples A, B and E have a rounded step with hysteresis, while for sample F the hysteresis is much less, the change in magnitude is opposite in sign and the anomaly is accompanied by a peak in acoustic loss. In a 5 T field, the rounded step with hysteresis still exists for samples A and B but the moment decreases rather than increases with increasing temperature. There is still a slight break in slope and/or hysteresis for samples E and F at 5 T.

softening of the shear modulus above T_{co} has been used to estimate a value of $T^*_{c\Gamma} - T_{c\Gamma}$ = 2 K for La$_{0.5}$Ca$_{0.5}$MnO$_3$ [Chen et al., 2010].

The strain evolution and elastic properties obtained by RUS for the incommensurate structure of La$_{0.5}$Ca$_{0.5}$MnO$_3$ are similar in form to those previously obtained for Pr$_{0.48}$Ca$_{0.52}$MnO$_3$, which has a nearly identical incommensurate structure stable below ~235 K [Cox et al., 2007 & 2008; Sanchez et al., 2008]. Comparison of figure 7 of Carpenter et al. (2010b) with Fig. 3.8 of the present work shows that values of $|e_{tx}|$ for bulk samples increase by ~0.025 through T_{co}, and $|e_4|$ changes by ~0.003 in both cases. This implies that the strength of coupling between shear strains and the Σ_2, M_2^+, Γ_3^+, M_3^+ and R_4^+ order parameter components is broadly similar, if not the same, for bulk samples of both materials. Data for the shear modulus and Q^{-1} are reproduced in Fig. 3.17 to show that, while the form of the elastic anomaly in Pr$_{0.48}$Ca$_{0.52}$MnO$_3$ is the same as of f^2 for sample F, the magnitude of softening as the transition is approached from above is less, as is the recovery below T_{co}. This is consistent with a larger value of $T^*_{c\Gamma} - T_{c\Gamma}$ (57 ± 24 K) estimated by applying Eq. 3.4 to the data for Pr$_{0.48}$Ca$_{0.52}$MnO$_3$ [Carpenter et al., 2010a], as opposed to 2 K referred to above for La$_{0.5}$Ca$_{0.5}$MnO$_3$. If the coupling strength (λ) is about the same, it follows that the effective values of a and/or $(C^0_{11} - C^0_{12})$ in Eq. 3.4 would be larger. In other words, replacing Pr by La may cause the entropy associated with the Jahn-Teller component of the transition and/or the bare elastic constants to increase. This remains somewhat speculative, however, because although values of the shear modulus reported by Zheng et al. (2002a) are comparable with those obtained here, the ultrasonic data of

Zheng et al. (2000) show a much steeper recovery below T_{co} and are rather similar to those of $\mathrm{Pr_{0.48}Ca_{0.52}MnO_3}$. It is possible that data for the elastic properties of sample F are not fully representative of those of a bulk sample of $\mathrm{La_{0.5}Ca_{0.5}MnO_3}$.

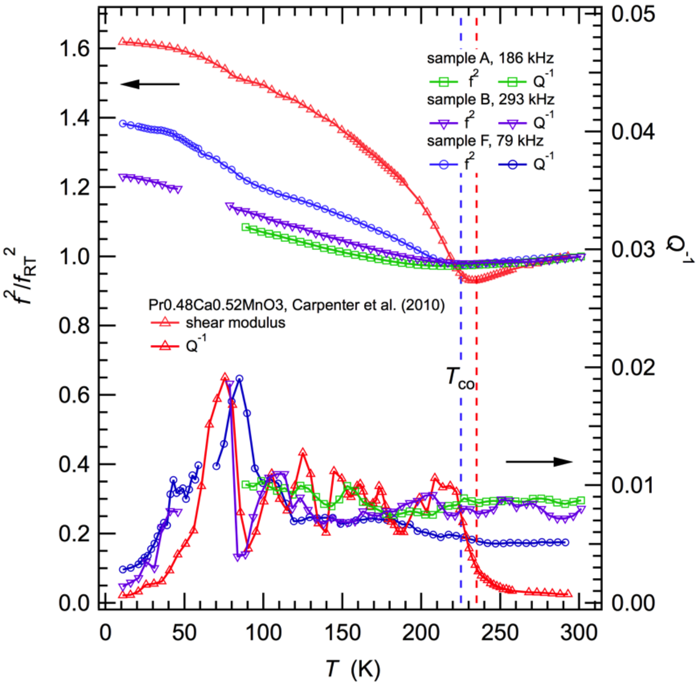

Figure 3.17: Comparison of RUS results from the present study with those of Carpenter et al. (2010a) for $\mathrm{Pr_{0.48}Ca_{0.52}MnO_3}$.

Comparison of Q^{-1} in Fig. 3.17 shows that a common feature for all the samples is the increase in loss below ~100 K. The peak in Q^{-1} at ~75 K for $\mathrm{Pr_{0.48}Ca_{0.52}MnO_3}$ was tentatively ascribed to a freezing process with an activation energy of ~5-10 $\mathrm{kJmol^{-1}}$ which might be related the motion of polarons as part of the response of the incommensurate structure to the application of external stress [Carpenter et al., 2010a]. Essentially the same loss peak appears to occur at ~85 K in data from sample F and, even though Q^{-1} variations are not constrained, there is an increase in loss through the same temperature range for the other samples of $\mathrm{La_{0.5}Ca_{0.5}MnO_3}$. However, two notable differences remain. Firstly, the 40 K anomaly is seen only in the data for $\mathrm{La_{0.5}Ca_{0.5}MnO_3}$. As $\mathrm{Pr_{0.48}Ca_{0.52}MnO_3}$ is purely antiferromagnetic at low temperatures, it follows that this anomaly is due to the ferromagnetic phase of $\mathrm{La_{0.5}Ca_{0.5}MnO_3}$. Secondly, Q^{-1} at $T > T_{co}$ drops to low values for $\mathrm{Pr_{0.48}Ca_{0.52}MnO_3}$ but remains high for $\mathrm{La_{0.5}Ca_{0.5}MnO_3}$, signifying that some degree of relaxational disorder with strain coupling remains at high temperatures in hot pressed pellets of the latter.

Suppression of the changes in shear strain at crystallite sizes of ~30-40 nm is accompanied by the expected reduction in the magnitude of the recovery of the shear modulus below T_{co} but not by complete elimination of the elastic anomaly. Softening as $T \rightarrow T_{co}$ from above appears to remain almost the same but recovery occurs in the form of a broad, rounded minimum rather than the concave-down form expected for pseudoproper ferroelastic behaviour. The macroscopic shear strain e_{tx} arising from coupling with the Γ_3^+ order parameter is suppressed by reducing grain size, but some local ordering apparently still remains and a convenient analogy is perhaps with the difference between a ferroelectric transition and freezing of dynamical polar nano regions in a relaxor ferroelectric. The signature of the latter with respect to strain and elastic properties is a frequency-dependent minimum in the elastic constants above the freezing point and Vogel-Fulcher dynamics through it. This is seen in RUS data for $\mathrm{Pb(Mg_{1/3}Nb_{2/3})O_3}$, for example [Carpenter et al., 2012]. There are hints in the present data for samples A and B of dispersion with respect to resonance frequencies, such that the same may apply also to $La_{0.5}Ca_{0.5}MnO_3$, but the quality of the data is not quite sufficient to determine this definitively. Evidence of local Jahn-Teller distortions of MnO_6 octahedra in nanocrystalline grains is provided also from XAFS investigation of sample A by Lahiri et al. (2012).

3.6.2 Magnetoelastic behaviour

Variations in elastic properties of the hot pressed pellets appear to be the same as for the powders pressed into pellets with CsI, suggesting that the measured elastic properties are intrinsic to the individual grains. There is, however, some contrast in magnetic properties between the pellets produced by hot pressing for the present work relative to those reported by Sarkar et al. (2008) for pellets produced by sintering at one atmosphere. The magnetic moment shown in figure 8 of Sarkar et al. (2008) for F increases below ∼250 K, due to ferromagnetic ordering, followed by a decrease with hysteresis below ∼200 K characteristic of the ferromagnetic–antiferromagnetic transition. Data for the pellet of F shown in Fig. 3.14 show a steady increase in magnetic moment below ∼260 K but no further reduction and a hysteresis interval at lower temperatures. The difference must be due to near surface effects when grains are in close proximity, since hot pressing will produce a denser ceramic with a higher proportion of grain boundaries in close contact.

There are no elastic anomalies in data collected above ∼40 K from the hot pressed pellets which correlate with changes in magnetic moment shown in Fig. 3.14 or from the CsI pellets which correlate with changes in magnetic moment shown in figure 8 of Sarkar et al. (2008). This confirms the conclusion from the incommensurate structure of $Pr_{0.48}Ca_{0.52}MnO_3$ that coupling between shear strain and the magnetic order parameter is weak.

Magnetic ordering in samples A, B and E is predominantly ferromagnetic. In detail the transition from para- to ferromagnetism in the hot pressed pellets occurs near 270 K, with first order character implied by the hysteresis between heating and cooling (Fig. 3.14 c). This mirrors the first order character of the paramagnetic–ferromagnetic transition seen in bulk samples of $La_{0.7}Ca_{0.3}MnO_3$ [*e.g.* Chen et al., 1999; Loudon & Midgley, 2006a & b], but there are contrasting features as well. Most notably, a bulk sample of $La_{0.7}Ca_{0.3}MnO_3$ does not show the elastic softening as $T \to T_c$ from above and there is a steep increase in stiffness at the transition point [Chen et al., 1999]. The same pattern of stiffening is seen for both longitudinal and transverse acoustic waves in $La_{0.67}Ca_{0.33}MnO_3$ [Zhu et al., 1999b & 2000] and resembles the pattern expected from biquadratic coupling of strain with the magnetic order parameter ($\lambda e^2 m^2$), *i.e.* stiffening (or softening, depending on the sign of the coupling coefficient, λ) which scales with m^2 as seen in the case of $YMnO_3$ [Thomson et al., 2014]. This difference reinforces the view that the elastic properties of nanocrystalline $La_{0.5}Ca_{0.5}MnO_3$ as a function of temperature are not determined by the magnetic transition but are indicative of local ordering of Jahn-Teller distorted octahedra. There are small irregularities in the temperature dependence of magnetic moments measured during cooling in a 5 T field, suggesting that the ferromagnetic ordering is not necessarily homogeneous over the entire temperature interval between ∼40 and ∼270 K (Fig. 3.16 shows the data up to 70 K).

3.6.3 Low temperature anomalies

There are a number of reports of changes in magnetic structure of half-doped manganites at low temperatures. For example, a peak in AC magnetic susceptibility at 41 K in $Pr_{0.5}Ca_{0.5}MnO_3$ has been explained in terms of a reentrant spin glass transition that leads to a low temperature state with ferromagnetic and spin glass clusters in an antiferromagnetic matrix [Cao et al., 2006]. The reported frequency dependence is rather slight, such that the peak shifts by only 0.2 K between 0.01 and 3 kHz. Doping of $La_{1-x}Ca_xMnO_3$ with Y also leads to a frequency dependent anomaly in the magnetic susceptibility near 40 K. In this case the shift in maximum susceptibility is several K for a frequency change of 0.001 to 1 kHz [Maignan et al., 1998; Freitas et al., 2001]. Glass-like arrested states have also been proposed for bulk samples of $La_{0.5}Ca_{0.5}MnO_3$ at low temperatures but the distinct anomaly in magnetic behaviour near 35 K was ascribed to a change from metastable ferromagnetic order to equilibrium antiferromagnetic order [Siruguri et al., 2013; Banerjee et al., 2008; Chaddah et al., 2008]. In nanowires of $La_{0.5}Sr_{0.5}MnO_3$ a magnetic anomaly at 42 K was attributed to freezing behaviour of surface spins [Chandra et al., 2013]. By way of contrast, the changes in magnetic moment near 40 K shown in Fig. 3.16 perhaps more closely resemble the pattern expected for a first order transition between structures with different magnetic ordering states. In the case of F, a peak in acoustic loss measured at ∼150 kHz occurs at the same temperature as the anomaly in DC magnetic moment, ruling out the possibility of any substantial dispersion with respect to frequency that would be expected for a freezing process. In this case, the data for f^2 just show a break in slope rather than an increase with falling temperature that would signify a classical Debye loss mechanism of the type well illustrated by the data for f^2 and Q^{-1} near 85 K. There must be some strain contrast across the transition and the loss mechanism perhaps involves motion under stress of interfaces between coexisting phases which also have slightly different elastic constants.

From the hysteresis curves in Fig. 3.15 it is clear that sample A (and B) has predominantly ferromagnetic structures above and below 41 K, so the transition is between one ferromagnetic structure and another. Changes in magnetic moment across the transition presumably reflect some or all of differences in moment, changes in the proportion of any relict antiferromagnetic moment and changes in domain structure. These are less obvious in the 5 T data (Fig. 3.16), which show only a break in slope of the moment at ∼40 K, presumably reflecting saturation magnetization. Not all samples of $La_{0.5}Ca_{0.5}MnO_3$ seem to show the same behaviour at low temperatures. For example, there are anomalies similar to those reported here near 40 K in the magnetic data of Levy et al. (2000) but not in the data of Sarkar et al. (2008), Rozenberg et al. (2009), Jirak et al. (2010) or Freitas et al. (2002). Chen et al. (2005) found an anomaly in the evolution of the longitudinal modulus at ∼50 K which is similar to that observed here in f^2 for acoustic resonances, and more marked changes at the same temperature in samples with higher Ca-contents. Several possible explanations may be offered but this issue is not resolved here. Firstly, some impurity phase(s) might be present in some samples. For example, Mn_3O_4 has prominent magnetoelastic transitions near 40 K [*e.g.* Suzuki & Katsufuji, 2008; Kim et al., 2011], though there does not appear to be evidence for its presence in powder diffraction patterns. Secondly, there could be differences of stoichiometry. For example, increasing the number of oxygen vacancies causes an anomaly to appear near 40 K in zero field cooled magnetic moments, in comparison with a stoichiometric sample with 3 oxygen atoms per formula unit [Trukhanov et al., 2002]. However, the reduction in oxygen content is also accompanied by a reduction in the magnetic ordering temperature below 240 K and, in the present study at least, it is has been found that the 40 K anomaly occurs in samples with $T_c \sim$ 260-280 K. Sarkar et al. (2008) reported that their samples all had some oxygen deficiency, $\sim La_{0.5}Ca_{0.5}MnO_{2.98}$ for the finest grain sizes and slightly greater non-stoichiometry for the coarsest sample, but it is possible that this was changed in the hot-pressing process. Finally, grain size effects, particularly with respect to magnetism, depend substantially on the changing ratio of material in the surface to material within the bulk in the usual way, but these can be modified by interactions between grains. Samples with higher density, such as produced by hot pressing, have a higher proportion of welded grain boundaries across which there should be relatively strong magnetic interactions, giving rise to the possibilities of changing patterns of stability in nanocrystalline samples.

3.6.4 Heterogeneity and local structure in nanocrystals

Jahn-Teller and charge ordering are suppressed both by application of a magnetic field and by reducing grain size, but the resulting ferromagnetic phases are not the same with respect to their macroscopic strain. It follows that other contributions to the structural state also cannot be the same, in particular because shear strains are coupled to octahedral tilting. Fig. 3.8 contains values for symmetry-adapted shear strains calculated from lattice parameters in Siruguri et al. (2013) for a bulk sample measured at 9 K in zero field and in an applied field of 7 T. In zero field the sample is antiferromagnetic, with strains that have values which are indistinguishable from those calculated from the original data of Radaelli et al. (1997). At 7 T these become more typical of an orthorhombic perovskite with distortions from cubic lattice geometry associated only with octahedral tilting. In particular, e_{tx} is nearly 3% for the structural state with cooperative Jahn-Teller distortions and only a few ‰ when this is suppressed. The comparison is essentially the same as between $Pr_{0.52}Ca_{0.48}MnO_3$ and $SrZrO_3$ in Carpenter et al. (2010b). On the other hand, values of e_{tx} and e_4 for the ferromagnetic nanocrystalline sample are $\sim$2% and show no evidence of changes through T_{co} or T_c (Fig. 3.8). A homogeneous ferromagnetic state with no Jahn-Teller ordering can be represented by $La_{0.75}Ca_{0.25}MnO_3$ for which lattice parameters of Radaelli et al. (1995) give e_{tx} and e_4 values of $\sim$ –0.003. This is again consistent with the effects of coupling between strain and octahedral tilting alone. The primary data show that the main strain associated with ferromagnetic ordering is a volume strain which reaches a maximum value of $\sim$ –0.002 in this case. Large shear strains in nanocrystalline sample of $La_{0.5}Ca_{0.5}MnO_3$ are presumably due to octahedral tilting alone, but the octahedra must on average be more distorted than at compositions where charge order/orbital order does not develop.

Comparison above of the elastic properties through the ferromagnetic transition in samples A and B with the more typical effects of magnetoelastic coupling seen in $La_{0.7}Ca_{0.3}MnO_3$ and $La_{0.67}Ca_{0.33}MnO_3$ also confirms that the structural state of the nanomaterials is somehow different with respect to strain. The minimum in shear modulus near T_{co} seen in the data for samples A and B has been interpreted here as indicative of local ordering of Jahn-Teller distorted octahedra, but without the development of additional macroscopic strain. This appears to be analogous to the suppression of strain accompanying tilting due to the introduction of A-site cation/vacancy disorder in the perovskite $La_{0.6}Sr_{0.1}TiO_3$. Local heterogeneous strain fields arising from the disorder hinder the development of a coherent macroscopic strain but do not suppress the tilting [Howard et al., 2007]. The length scale of these local heterogeneities is likely to be comparable with that seen associated with replacing one cation by another of different size, *i.e.* $\sim$10-20 Å [Carpenter et al., 2009]. If, as is proposed and raised as a possibility by Sarkar et al. (2008), nanocrystals of $La_{0.5}Ca_{0.5}MnO_3$ contain heterogeneous shear strains locally within them, they would not be expected to show identical physical properties to thin films in which a homogeneous strain is imposed by the substrate.

3.7 Conclusions

In the present investigation LCMO samples of particle size ranging between 34 and 136 nm were measured by means of resonant ultrasound spectroscopy with the aim to detect their elastic and anelastic properties. In particular, the evolution of shear modulus with temperature was considered, in order to evaluate the role of particle size in the occurrence of structural and magnetic phase transitions at low temperatures. Softening of the shear modulus was observed at crystallite sizes of 75 and 136 nm, with a minimum value near the charge order transition temperature ($\sim$225 K): this is consistent with a bilinear coupling between tetragonal strain and the Jahn-Teller order parameter. The form of this softening matches well with the one seen previously in samples with bulk properties. On the contrary, when the nano scale is reached, it is clear the suppression of shear strains, which leads to the suppression of charge ordering, even though some local distortions should still be present. This can be gathered by observing the tendency of the temperatures at which the minima values of shear modulus occur to be frequency dependent: therefore, some degree of pseudoproper ferroelastic behaviour is retained also in nano pellets, leading to the belief of the occurrence of a freezing process, rather than a discrete phase transition. Ferromagnetism in all the samples is believed to occur simply because ferroelastic strain relaxations, acting locally or more "macroscopically" within the structure, stabilizes the Jahn-Teller distortions in MnO_6 octahedra. As consequence of all these considerations, in manganites the control of strain becomes a useful tool, in order to tune the physical properties towards a desired feature. However, it should be paid attention to the structural states, as they can vary much, depending on the method that is chosen to be applied.

Chapter 4

Study of local structure in nanocrystalline zirconia

4.1 Introduction

4.1.1 Zirconia polymorphism

The polymorphism of zirconium oxide (zirconia, ZrO_2) is a deeply investigated topic, for its fundamental aspects and because many technological applications [Stevens, 1983] in areas such as energy conversion [Kharton et al., 2004], electrochemical sensors [Kharton et al., 2004], thermal coatings [Clarke et al., 2005], and structural ceramic materials are based on the performing properties of the tetragonal and/or cubic polymorphs. These are thermodynamically stable above 1175 and 2370 °C, respectively, while the monoclinic form is stable in the lowest temperature range (see the left hand side of Fig. 4.2). Fig. 4.1 shows the structures of the three mentioned polimorphs: A represents the monoclinic phase (space group: $P2_1/c$; a = 5.15 Å, b = 5.20 Å, c = 5.32 Å), with zirconium in coordination VII; B is the tetragonal structure (space group: $P4_2/nmc$; a = 3.64 Å, c = 5.27 Å), where Zr forms distorted cubes with oxygen atoms; C is relative to the cubic polymorph (space group: $Fm\bar{3}m$; a = 5.16 Å), where Zr is linked to O atoms through 8 bonds of the same lenght.

It is well known that doping zirconia (Y^{3+} and Ca^{2+} are the most common ions used) stabilizes the high temperature phases at room conditions, in a way that can be easily appreciated by moving from the left hand side towards the right hand side of Fig. 4.2. The doping method is very useful, as it produces good solid electrolytes: indeed, it strongly enhances oxygen ion transport in the zirconia structure, by supplying oxygen vacancies through compensation of the substitutional defects. It is possible, however, to obtain the tetragonal polymorph without any doping, when the crystal size of the sample is below a certain limit value, which is approximetely 25 nm (Garvie, 1978).

4.1.2 Literature and aim of the project

The present study is part of a project focussed on fabrication and functional characterization of the fully dense oxides with nanometer-sized grains, which can be produced by sintering of zirconia nanopowders without significant grain growth using the HP-FARS technique (see Subsection 3.3.1 and Maglia et al. (2010 & 2013) for a deeper description). As the tetragonal phase is required at room temperature, the size-induced stabilization is the fabrication route of interest.

A size-induced stabilization of the tetragonal polymorph (without the use of dopant elements) has been first shown

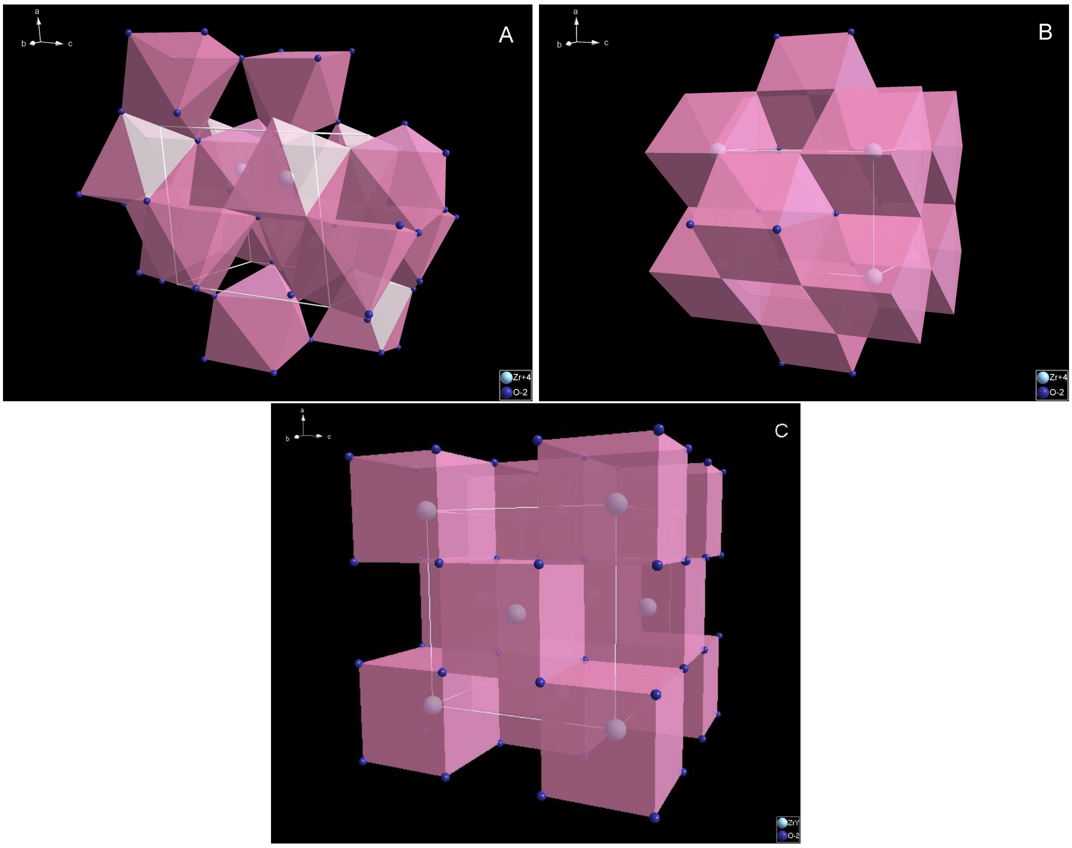

Figure 4.1: The unit cells of zirconia polymorphs: A refers to the monoclinic structure, stable at room temperature (baddeleyite is the name of the mineral forming in nature), while B and C represent the tetragonal and cubic HT structures, respectively.

by Garvie (1965 & 1978). He proposed that the presence of tetragonal ZrO_2 at room temperature can be explained by a crystallite size effect, which is strongly related to non-hydrostatic stresses occurring within the crystal. Specifically, he predicted that particles below ∼25 nm in diameter stabilize the high temperature form, while those with critical size above 25 nm are subject to the tetragonal–monoclinic transformation. Fig. 4.3 points out what just said: if a crystal is strain-free, the tetragonal structure is observed where only monoclinic should be present, that is, strain induced by reduction of particle size lowers substantially the transition temperature.

Other reports on the stabilization of tetragonal zirconia in forms of nanopowders or thin films can be found in Shukla & Seal (2005) and references therein. In particular, these mentioned authors have reviewed the controversial mechanism by considering the effects of surface energy, strain energy, pressure, structure, phase and chemical impurities, and water vapor, and propose that generation of excess oxygen ion vacancies within the nanocrystalline ZrO_2 is primarily responsible for the room temperature stabilization of the tetragonal phase.

In nanocrystals the coherence is very limited (just a few nanometers), thus they are objects very difficult to be studied. A local probe is necessary in order to highlight the local differences with respect to the average structure obtainable from conventional crystallography. Indeed, difficulties arise when nanocrystals are investigated (even if the average structure is finally derived), as the integrated intensities of Bragg's peaks can be determined only with large uncertainty because of the extremely broad profile. Local probes that can be used, in order to face the problem, include EXAFS, Raman spectroscopy, solid state NMR, and also total scattering with Pair Distribution Function (PDF) analysis. While the scientific literature reports thousands of papers variously dealing with the structure of tetragonal zirconia, it is hereafter accounted only for the few of them concerning the local structure of

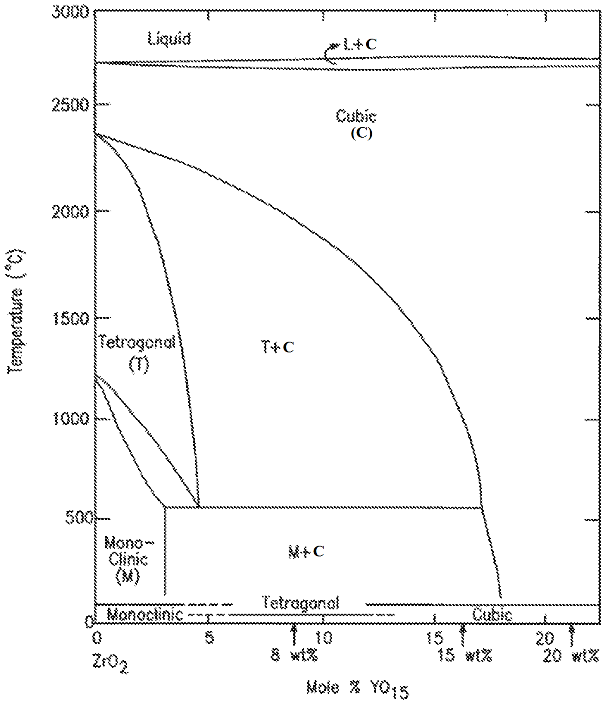

Figure 4.2: The zirconia phase diagram. Figure taken from `http://www.google.com/patents/US8197950`.

pure as well as doped nanocrystalline materials.

When investigating the local structure of undoped tetragonal zirconia nanocrystals with different grain sizes in the range of 10 nm, Acuna et al. (2010) have shown that the tetragonal model with 4+4 equal distances in the first coordination shell of Zr does not fit the EXAFS data, if the Debye-Waller factors of the two subsets are constrained to equal values. When the latter parameters are instead left free to vary independently, the results unquestionably show that one of the two sub-shells is much more disordered than the other one. This can be summarized as a model with 4+2+2 different Zr-O distances. Gateshki et al. (2005), on the other hand, have shown that the nanocrystalline zirconia obtained from ball-milling of pure monoclinc zirconia, seemingly retains locally its monoclinic structure, while the average structure shifts towards a tetragonal/cubic arrangement. The same local 'monoclinic' environment has been confirmed by two other papers from the same first author [Gateshki et al., 2006& 2007] on nanocrystalline zirconia, synthesized in different ways. Finally, Dapiaggi et al. (2010), talking about the slow transition of the tetragonal phase into the monoclinic one, ascribe the reason of the occurrence of the tetragonal–monoclinic phase transformation to the release of the microstrain.

Here are presented the results of a series of total scattering experiments with high energy synchrotron X-rays on undoped (or very lightly doped) nanocrystalline zirconia samples ($Zr_{1-x}Y_xO_2$ with x = 0, 0.005, 0.01 and 0.02). The experimental data are processed both in a classical crystallographic way, with the Rietveld method [Rietveld, 1969 & 2010] and with the PDF approach [Egami & Billinge, 2003, and references within], which is described in the next Section. PDF refinements allow to evaluate the local as well as the average structure at the same time, because the whole powder diffraction pattern is taken into account in the assessment of the atomic pair distribution function for the sample under study. As known, heterovalent cation such as Y^{3+} (in place of Zr^{4+}) injects oxygen vacancies: the local environment of zirconium and oxygen atoms in samples with small quantities of Y (x = 0.005, 0.01, and 0.02) can be directly compared with that of undoped samples obtained through the same synthetic route. The results show that the PDFs of the different samples allows to characterize the variations of

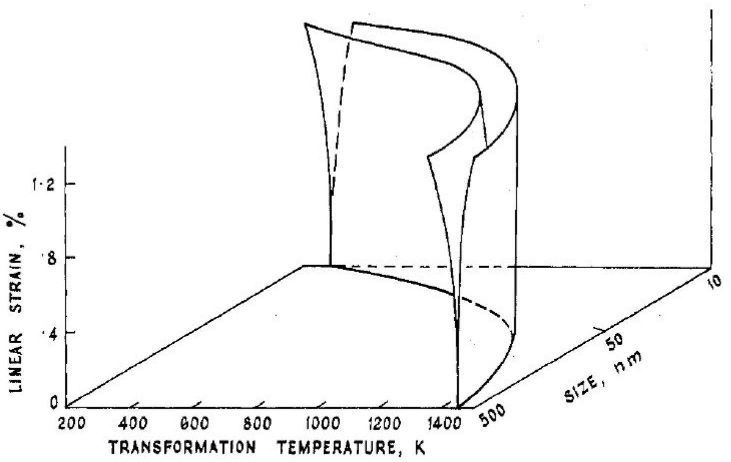

Figure 4.3: The tetragonal–monoclinic transition temperature of zirconia as a function of crystallite size and internal strain. To the left of the band the structure is monoclinic, to the right it is tetragonal and within the band both polymorphs coexist. Figure taken from Garvie (1978).

local and the average structures, as well as the presence of local distortions and their features.

4.2 Theory

The modern material science deals with materials becoming always more and more complicated and/or characterized by a structural coherence limited to little inner regions. In many cases, these complexities and local distortions are what determines the peculiarity of a material with respect to its physical properties. Classical crystallography, which has been for decades the appropriate tool to study the crystal stucture of compounds, is no longer sufficient to understand the properties on the atomic scale, since it only refers to Bragg scattering and so it only yields the long range average structure of the material. On the contrary, total scattering includes both Bragg and diffuse scattering, thus it contains information not only about long range order but also about short range order (SRO), which means that chemical SRO, distortions, correlated motions, orientational SRO of molecules can be detected and examined. The best method to determine accurately crystallographic structures is single crystal diffraction. However, in many cases only poor quality crystals can be grown or even the compound of interest is not able to form single crystals of the required size. This is why powder diffraction is the suitable technique to which resort, and the atomic pair distribution function method, widely used at first for glasses and liquids [Klug and Alexander, 1968; Warren, 1969], becomes the powerful approach from which one gets information on the local structure of even polycrystalline materials, thanks to the advent of high power X-ray and neutron sources and fast computing.

The basis of the total scattering method is the normalized, measured, scattering intensity from a sample, the total scattering structure function, S($\mathbf{Q}$). This intensity distribution is a continuous function of the wavevector, $\mathbf{Q}$, and in general contains both Bragg and diffuse intensity. The *sample scattering amplitude* $\Psi(\mathbf{Q})$ is given by the following:

$$\Psi(\mathbf{Q}) = \frac{1}{<b>}\sum_{\nu} b_\nu e^{i\mathbf{Q}\mathbf{R}_\nu} \tag{4.1}$$

where $\mathbf{Q}$ is the diffraction vector, or the momentum transfer (see Fig. 4.4), and is defined by:

$$\mathbf{Q} = \mathbf{k_{init}} - \mathbf{k_{fin}} \tag{4.2}$$

where $\mathbf{k_{init}}$ ($|\mathbf{k_{init}}| = 2\pi/\lambda_{init}$) is the wavevector of the incoming beam and $\mathbf{k_{fin}}$ ($|\mathbf{k_{fin}}| = 2\pi/\lambda_{fin}$) is the wavevector of the scattered beam. For elastic scattering $\lambda_{init} = \lambda_{fin}$, thus the magnitude of $\mathbf{Q}$ is:

$$Q = |\mathbf{Q}| = 2k\sin\theta = \frac{4\pi\sin\theta}{\lambda} \tag{4.3}$$

where $k = |\mathbf{k_{init}}| = |\mathbf{k_{fin}}|$.

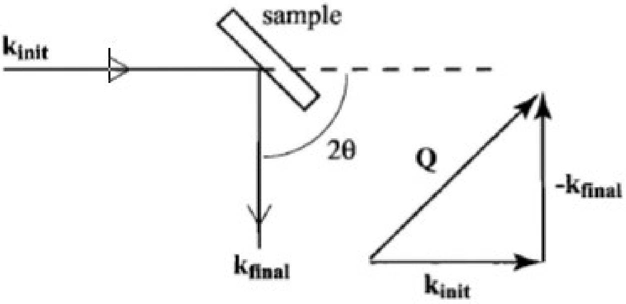

Figure 4.4: Geometry of the powder diffraction measurement and definition of the scattering vector, $\mathbf{Q}$. Figure taken from Egami & Billinge (2003).

In Eq. 4.1 $\mathbf{R}_\nu$ defines the position of the νth atom, b_ν is the scattering amplitude of the atom ν (a measure of how strongly it scatters), and $< ... >$ represents a compositional average:

$$< b > = \frac{1}{N}\sum_\nu b_\nu = \sum_\alpha c_\alpha b_\alpha. \tag{4.4}$$

Here the sum over ν is over every atom in the sample: c_α is the atomic fraction and b_α is the scattering amplitude of the element α. For X-rays, b_ν depends fairly strongly on Q and is usually denoted as $f(Q)$, but for neutrons it is independent of Q. This difference reflects the quite different spatial spread of the scatterer: electron density for X-rays and nucleus for neutrons.

In general, the Fourier transform of a function $f(\mathbf{x})$ is given by $F(\mathbf{Q}) = \sum_{j=-\infty}^{\infty} f(\mathbf{x}_j)e^{i\mathbf{k}\mathbf{x}_j}$. Upon inspection of Eq. 4.1 it is evident that $\Psi(\mathbf{Q})$ is just the Fourier transform of the atomic position, $\mathbf{R}_\nu$. The structural information is contained in the phase of the exponential factor. Thus, if this scattering amplitude is known, the atomic structure can be determined exactly, merely by taking the inverse Fourier transformation of $\Psi(\mathbf{Q})$. However, as is well known, a diffraction experiment does not give directly the scattered amplitude $\Psi(\mathbf{Q})$, but only the intensity of the diffracted beam, which is directly related to the square of the magnitude of $\Psi(\mathbf{Q})$, *i.e.* $|\Psi(\mathbf{Q})|^2$. In details,

$$\begin{aligned}
\frac{\mathrm{d}\sigma_C(\mathbf{Q})}{\mathrm{d}\Omega} &= \frac{<b>^2}{N}|\Psi(\mathbf{Q})|^2 = \frac{1}{N}\sum_{\nu,\mu} b_\nu b_\mu e^{i\mathbf{Q}(\mathbf{R}_\nu - \mathbf{R}_\mu)} \\
I(\mathbf{Q}) &= \frac{\mathrm{d}\sigma_C(\mathbf{Q})}{\mathrm{d}\Omega} + <b>^2 - <b^2> \\
S(\mathbf{Q}) &= \frac{I(\mathbf{Q})}{<b>^2}
\end{aligned} \tag{4.5}$$

where $\frac{\mathrm{d}\sigma_C(\mathbf{Q})}{\mathrm{d}\Omega}$ is the coherent scattering cross-section, N is the number of atoms in the system, and $\mathrm{d}\Omega$ is the solid angle that the detector subtends with the origin where the sample is located. $S(\mathbf{Q})$ is called the *total scattering structure function* or often just *structure function*, which converges to unity at large $\mathbf{Q}$. The term $<b>^2 - <b^2>$ in the expression for $S(\mathbf{Q})$ is called the Laue monotonic scattering and is needed for convenience simply because $\frac{\mathrm{d}\sigma_C(\mathbf{Q})}{\mathrm{d}\Omega}$ approaches $<b^2>$ at large Q, while we want to make $S(\mathbf{Q})$ approach unity at large Q. Actually it is possible to define $S(\mathbf{Q})$ differently by normalizing with respect to $<b^2>$ rather than $<b>^2$: in this case the Laue term is no longer necessary.

For crystallography, the assumption of perfect periodicity is the centerpiece. However, a crystal structure is never perfectly periodic even when the crystal is perfect, because atoms are not static, but are vibrating due either to thermal or zero-point quantum vibrations. Consequently, $\mathbf{R}_\nu$ changes with time, and $\Psi(\mathbf{Q})$ is a function of time. Thus, Eq. 4.1 becomes:

$$\Psi(\mathbf{Q},t) = \frac{1}{<b>}\sum_\nu b_\nu e^{i\mathbf{Q}\mathbf{R}_\nu(t)} \tag{4.6}$$

with $\mathbf{R}_\nu(t) = \mathbf{u}(t) + \ll R \gg$, where $\ll R \gg$ is the time-averaged position of the atom and $\mathbf{u}$ is the deviation from that position. As it can be demonstrated that:

$$\ll e^{i\mathbf{Q}\mathbf{R}} \gg \simeq e^{i\mathbf{Q}\ll\mathbf{R}\gg} e^{-\frac{1}{2}Q^2\ll u^2\gg} = e^{i\mathbf{Q}\ll\mathbf{R}\gg} e^{-W}, \tag{4.7}$$

it is clear that the effect of lattice vibrations is not to broaden out the Bragg peaks, but to diminish their intensity by the factor $e^{-\frac{1}{2}Q^2\ll u^2\gg}$. Eq. 4.7 is known as the Debye-Waller approximation, which was developed in order to incorporate the effect of lattice vibrations in the structure function, and the term $e^{-\frac{1}{2}Q^2\ll u^2\gg} = e^{-W}$ is called the Debye-Waller factor.

The lost intensities of the Bragg scattering (reduced by the Debye-Waller factor) appear in between the Bragg peaks and become what is called *diffuse scattering*. The diffuse intensity is widely spread over Q-space, compared to the Bragg peaks that are strongly confined at reciprocal lattice points in Q-space. However, a significant proportion of the total integrated intensity can reside in the diffuse scattering: indeed, in the high Q-region where the Bragg peaks are small due to Debye-Waller factor, the scattering is predominantly diffuse. In the cases of gases, liquids and glasses, as well as in materials of finely powdered crystallites, the scattering is isotropic, so the diffuse scattering only weakly depends upon $\mathbf{Q}$ and forms a continuous background which is usually discarded in crystallographic analyses, but provides important information regarding the local deviations from the average structure.

The *total scattering* technique is an approach, alternative, and sometimes complementary, to standard crystallographic analysis, which treats both the Bragg peaks and diffuse scattering on an equal basis by considering the

normalized, measured, scattering intensity from a sample, $S(\mathbf{Q})$, and the atomic pair distribution function analysis is the Fourier analysis of the total scattering, from which information on local structure can be obtained.
Starting from the definition of the scattering amplitude, it is possible to derive the PDF as a convolution of the atomic density function. Eq. 4.1 can be written as follows, in terms of the *atomic density function*, $\rho(\mathbf{r})$, defined in Eq. 4.9:

$$\Psi(\mathbf{Q}) = \int \rho(\mathbf{r}) e^{i\mathbf{Q}\mathbf{r}} \mathrm{d}\mathbf{r} \tag{4.8}$$

where $\mathbf{r}$ is a radial distance.
Since

$$\rho(r) = \rho_0 g(r) = \frac{1}{4\pi N r^2} \sum_{\nu} \sum_{\mu} \delta(r - r_{\nu\mu}) \tag{4.9}$$

and

$$S(\mathbf{Q}) = \frac{1}{N} |\Psi(\mathbf{Q})|^2, \tag{4.10}$$

it can be derived the Fourier transform of the scattered intensity

$$G(r) = 4\pi r(\rho(r) - \rho_0) = 4\pi r \rho_0 (g(r) - 1) = \frac{2}{\pi} \int_0^\infty Q[S(Q) - 1] sin(Qr) \mathrm{d}Q \tag{4.11}$$

which defines the *reduced pair distribution function* $G(r)$, and provides the *atomic pair distribution function*, $g(r)$. In Eq. 4.9 ρ_0 is the average atomic number density, δ is a Dirac delta function and $r_{\nu\mu} = |\mathbf{r}_\nu - \mathbf{r}_\mu|$ is the distance separating the νth and μth atoms.
The function $G(r)$ gives information about the number of atoms in a spherical shell of unit thickness at a distance r from a reference atom. It peaks at characteristic distances separating pairs of atoms. An example of $G(r)$ from fcc nickel is shown in Fig. 4.5 b, while Fig. 4.5 a represents the *reduced structure function* $F(Q) = Q[S(Q) - 1]$, from which the PDF plotted in b is obtained.

While the atomic pair distribution function $g(r)$ is normalized so that, as $r \rightarrow \infty$, $g(r) \rightarrow 1$, and, as $r \rightarrow 0$, it becomes zero, the reduced pair distribution function $G(r)$ oscillates around zero in the limit of large r, and behaves like $-4\pi\rho_0 r$ as $r \rightarrow 0$, which means that at low-r this latter function is a straight line going through zero with a slope that is proportional to the average number density of the material. The main advantage of $g(r)$ is that it emphasizes the low-r short-range order. However, when this function is determined experimentally, the uncertainties in the data fall off like $\frac{1}{r}$, that is they scale with the amplitude of the signal (which also falls off like $\frac{1}{r}$). On the contrary, in the $G(r)$, which is the direct Fourier transform of the intensity data, the random uncertainties on the data are constant in r, and thus fluctuations in the difference curve between calculated and measured plots have the same significance at all values of r. A further advantage of the $G(r)$ is that the amplitude of the oscillations gives a direct measure of the structural coherence of the sample: in a crystal with perfect structural coherence, oscillations in $G(r)$ extend to infinity with a constant peak-peak amplitude; in the $G(r)$ from a real crystal, the peak-peak amplitude of the signal gradually falls off due to the finite Q-resolution of the measurement, which is

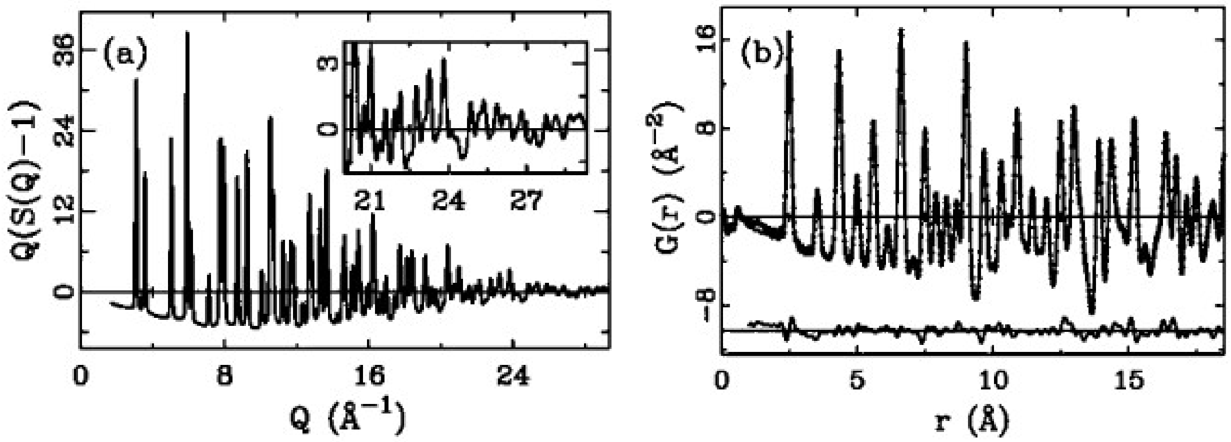

Figure 4.5: The reduced structure function, $Q[S(Q)-1]$, of crystalline Ni (a) and the PDF (b) obtained by Fourier transforming the data in (a). The figures were taken from Billinge & Kanatzidis (2004).

the limitation; in samples with some degree of structural disorder, the signal amplitude in $G(r)$ falls off faster than dictated by the Q-resolution and this becomes a useful measure of the structural coherence of the sample [Mazadeh et al., 2007].

The trouble with the Fourier transform is that it depends from the Debye-Waller factor, which gives rise to lost of the scattered intensity at high-Q. So, we would like to measure data up to Q infinity, but, of course, this is not possible. The cutoff at finite Q decreases the real-space resolution of the PDF and causes the so-called termination ripples. Moreover, the increase of Q_{max} allows also to obtain detailed structural information, which, otherwise, would not be available. These concepts are clearly illustrated in Fig. 4.6, where the $G(r)$s obtained on the semiconductor alloy ZnSe$_{0.5}$Te$_{0.5}$ from data terminated at different Q_{max} show the big differences in resolution and structural details: the Zn–Se and Zn–Te peaks at about 2.45 Å and 2.6 Å are, indeed, distinct only at higher Q_{max}.

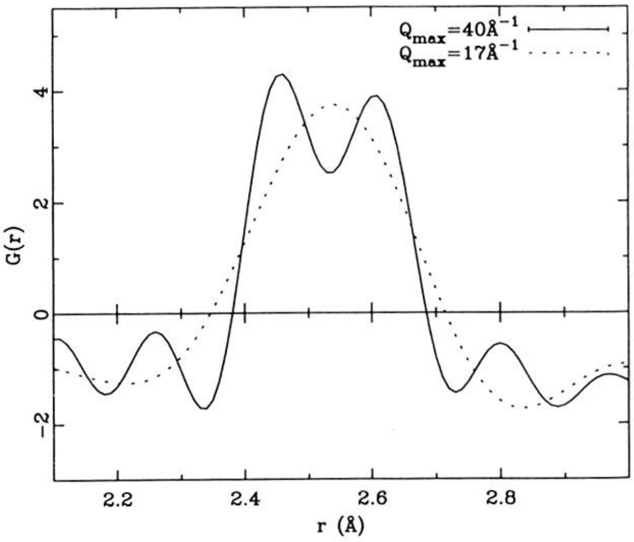

Figure 4.6: Resolution in PDF. Example of the nearest neighbor peaks of the semiconductor alloy ZnSe$_{0.5}$Te$_{0.5}$. The solid line corresponds to terminating at Q_{max} = 40 Å^{-1}, clearly showing the peak split relative to the two bond lenghts Zn–Se and Zn–Te. The dotted line shows the PDF obtained from the same data terminated at Q_{max} = 17 Å^{-1}: the peak split is no longer visible. Figure taken from Proffen et al. (2002).

Since $Q = \frac{4\pi sin\theta}{\lambda} \leq \frac{4\pi}{\lambda}$, to increase Q_{max}, it is necessary to decrease λ. Data should be collected up to the Q_{max} at which the Debye-Waller factor is less significant: ideally Q_{max} should be 40-60 $Å^{-1}$ but 20-30 $Å^{-1}$ can be satisfactory. For neutron PDF measurements, spallation neutron sources are the most suitable. In the case of X-rays, increasing the real-space resolution presents an additional challenge: indeed, the scattering factor $f(Q)$ falls off sharply with increasing Q, resulting in a weak signal at high diffracting angles. However, when data are divided by $|f(Q)|^2$, as per Eq. 4.11, diffuse structure becomes visible in the high-Q region. It is, therefore, important to carry out data collections up to these high-Q values with good statistics. This does not present a problem when high-flux, high-energy synchrotrons are used, such as the Advanced Photon Source (APS) (Argonne National Laboratory, Illinois, USA), or the European Synchrotron Radiation Facility (ESRF) (Grenoble, France), where the measurements here elaborated were actually collected.

4.3 Experimental procedure

4.3.1 Sample synthesis

Zirconia nanopowders with $YO_{1.5}$ as dopant were synthetized by a modified Pechini method (Pechini, 1967), so to obtain samples with 0, 0.5, 1 and 2 at.% Y content (*i.e.* from pure ZrO_2 to $Zr_{0.98}Y_{0.02}O_{2-x/2}$). A commercial aqueous solution containing the proper amount of zirconyl (IV) nitrate and yttrium nitrate was mixed with a solution of citric acid in the total metal *versus* citric acid molar ratio of 1:1. The solution was then stirred on a hot plate at 80 °C, to obtain a solution of increasing viscosity. After 3 h the mass turned into a colorless transparent glass. Further heating (5 h for the reported amounts) provided a white solid, which was subsequently ground in a mortar and calcined in a furnace at 500 °C for 1 h, in order to avoid the formation of monoclinic zirconia, to minimize the amount of carbonaceous residual and to promote the smallest possible grain size.

4.3.2 X-ray powder diffraction

Data collection was carried out at the beamline ID31 (European Synchrotron Radiation Facility, Grenoble, France), during experiments HS3611 and HS3654.

The beamline, which has been transferred to ID22 in 2014, offers high-resolution powder diffraction [Fitch, 2004]. Figure 4.7 shows the diffractometer set in the hutch (left) and the outline of its optics (right), which is described in the following steps:

1. the highly collimated beam from the undulator source is incident on a cryogenically-cooled Si 111 double-crystal monochromator: the first one is side cooled by Cu blocks through which liquid nitrogen flows; the second one is cooled by thermally conducting braids that link to the first crystal, and has electrical heaters to keep its temperature stable to -60 ± 0.05 °C;

2. a piezoelectric feedback system compensates for changes in the Bragg angle of the second monochromator crystal caused by changes in the heat load on its supporting mechanics;

3. water-cooled slits define the size of the beam incident on the monochromator and of the monochromatic beam transmitted to the sample;

4. the sample has dimensions tipically in the range 0.5-2.5 mm (horizontal) and 0.1-1.5 mm (vertical);

5. the diffractometer arm, equipped with nine Si 111 analyser crystals and detectors (channels separated by $\sim 2°$), is scanned vertically in a continuous mode, thus registering nine high-resolution diffraction patterns

in parallel, as a function of 2θ. The channels are normalised and combined in a subsequent data-reduction step to produce the equivalent step scan.

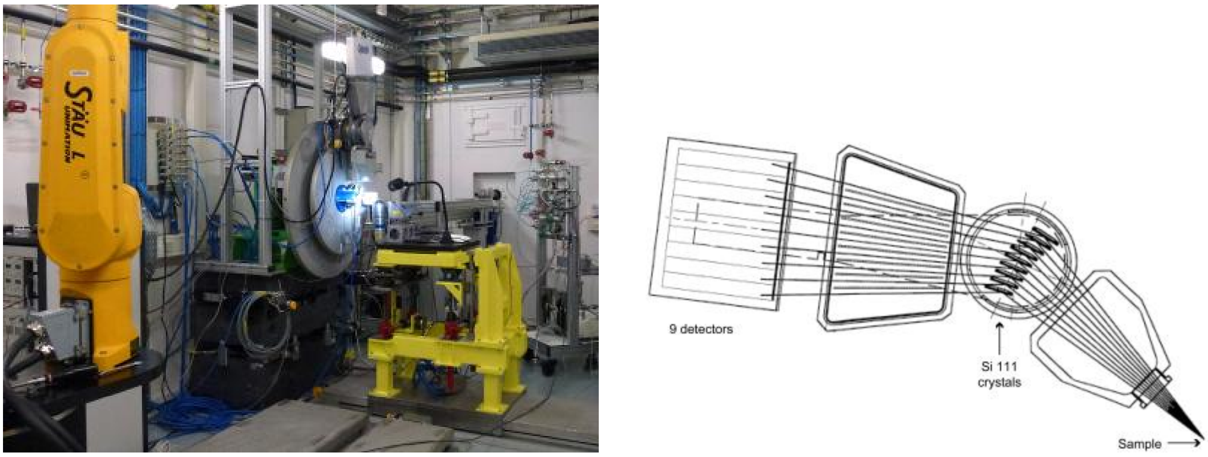

Figure 4.7: ID31 beamline. Figures taken from `http://www.esrf.eu/id22/technical-description`.

Among the applications of this high-resolution powder diffraction beamline are the following:

1. structural studies: solving and refining of crystal structures, structure of glasses and atomic pair distribution function analysis;
2. *in-situ* studies: observation of materials evolving with temperature, time, voltage, etc. during phase changes, solid-state chemistry, electrochemistry, etc.;
3. anomalous scattering: access to the K or L edge (sometimes both) for all elements beyond Cr in the periodic table;
4. high-throughput studies: explorations involving many samples, synthesized with different compositions, or under varied preparation conditions, etc.;
5. quantitative analysis: complex mixtures, detection of phases present in low proportions;
6. microstructural analysis: detailed analysis of diffraction peak shapes;
7. residual strain measurement: either by the sin2(ψ) technique, or by defining a gauge volume and mapping from within the bulk and surface of a sample;
8. grazing incidence (and reflectivity): measurements from thin films and surfaces.

For the present experiments, which fall in the first category of applications, the wavelenght employed was of about 0.4 Å, while the Q_{max} was used up to 23 Å^{-1}. A boron glass capillary, used as sample-holder, was measured indipendently, in order to subtract its contribution from the diffraction pattern of each sample. Thus, the collected data were corrected and normalised with PDFgetX3 [Juhas et al., 2013], using a low-Q-space polynomial, and the resulting $G(r)$ were calculated between 0 and 200 Å, in order to compare the PDF refinements of the high r regions with Rietveld refinements of the same datasets. The PDF refinements were performed using PDFgui [Farrow et al., 2007], while Rietveld refinements were made with the MAUD package [Ferrari & Lutterotti, 1994].

4.3.3 Transmission electron microscopy

TEM observations were carried out at Department of Earth Siences, University of Milano (Italy), using a FEI Tecnai F20 with Field Emission Gun (FEG), with an accelerating voltage of 200 kV. The microscope is equipped with an S-Twin lens that gives a point resolution of 0.24 nm. An energy dispersive X-ray spectrometer (EDS) with ultrathin window is present. The imaging system is composed by one tv rate 626 Gatan and one slow scan 794 Gatan CCD cameras.

Figure 4.8: The FEI Tecnai F20 TEM. Picture taken from `http://nano.tau.ac.il/index.php/labs/9-equipment/microscopes/23-philips-tecnai-f20-tem`.

4.4 Results and discussion

The present Section is hereafter divided into three Subsections, which contain different, but complementary, structural observations deduced from the conducted experiments. Powder diffraction data gave the possibility to investigate the lattice configuration of tetragonal zirconia through both reciprocal-space and real-space refinements, and to calculate the crystallite size and microstrain of synthesized powders, while TEM images provided a further check of particle dimensions and size distribution.

4.4.1 Rietveld refinements

The Rietveld refinements show that the nanopowders are all tetragonal, without any content in monoclinic polymorph (Fig. 4.9). The cubic and tetragonal polymorphs are very similar to eah other, and so are their diffraction patterns. However, the (102) peak, which is allowed only in the tetragonal structure, not in the cubic one, is well recognised in the patterns in Fig. 4.9, where it is indicated by an arrow.

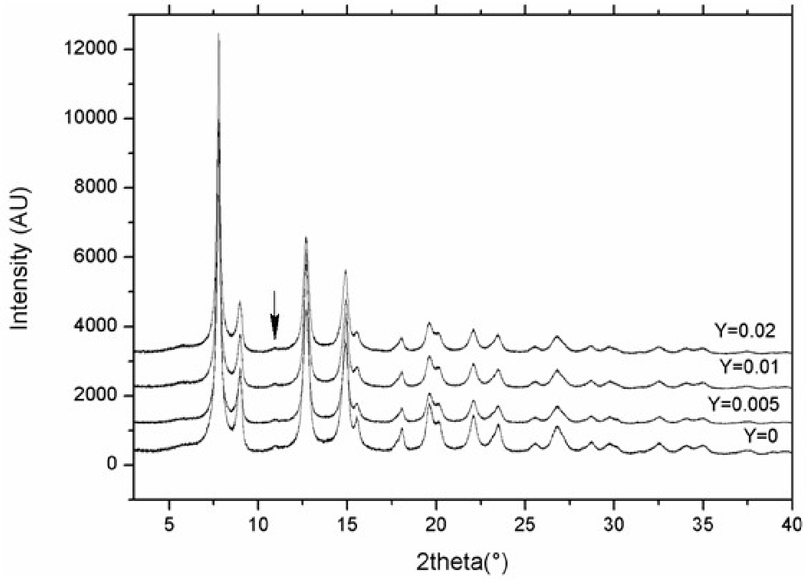

Figure 4.9: Data sets of the nanocrystalline zirconia samples. The small peak indicated by an arrow is the (102) of the tetragonal structure.

Crystallite size and RMS strain were evaluated using the isotropic model available in MAUD [Ferrari & Lutterotti, 1994]. The fit is very good, as it can be clearly seen from R_{wp} values reported in Table 4.1.

Table 4.1: Rietveld refinements.

Sample	a (Å)	c (Å)	$c/a\sqrt{2}$	<D$_v$>(Å)	RMS strain	U(Zr, Y) (Å^2)	U(O) (Å^2)	X(O)	R_{wp} (%)
Y0	3.5963(2)	5.1684(5)	1.015	97.1(1)	0.0015(8)	0.013(1)	0.028(9)	0.282(1)	6.49
Y0.005	3.5964(2)	5.1706(5)	1.017	93.2(1)	0.0024(8)	0.011(1)	0.024(9)	0.281(1)	6.25
Y0.01	3.5972(2)	5.1692(5)	1.016	95.6(1)	0.0023(3)	0.012(1)	0.028(8)	0.280(2)	6.25
Y0.02	3.5988(2)	5.1692(6)	1.016	86.1(2)	0.0021(3)	0.013(1)	0.030(8)	0.278(1)	6.40

In the model used, with space group *P4$_2$/nmc*, Zr (and Y) sits in $2a$ (0,0,0) position, and oxygen in $4c$ (0,0,z) position, with z = 0.285. The refinements were performed keeping free cell dimensions, microstructural parameters, isotropic thermal parameters (one for oxygen atoms, and a common one for Zr and Y), and the fractional coordinate of oxygen. The samples are very similar to each other in their microstructural characteristics: their crystallite size ranges from 86 to 97 Å, putting them well within the size range for size stabilization of the tetragonal structure, and their RMS strain ranges from 0.015 to 0.024. The variations of the cell parameters as function of composition are on the 3rd decimal place (the content of Y in the samples is very small), and their degree of tetragonality (represented by $c/a\sqrt{2}$, in Table 4.1) is very close to one, thus confirming that the tetragonal distortion is indeed very small. The empty squares in Fig. 4.10 show the trend of the cell volume as a function of composition (Y content), with a more or less smooth increase of the cell dimensions with increasing Y content. This is expected, as Y ions have ionic radius of 1.08 Å, while Zr^{4+} ionic radius is 0.89 Å (according to Shannon, 1976).

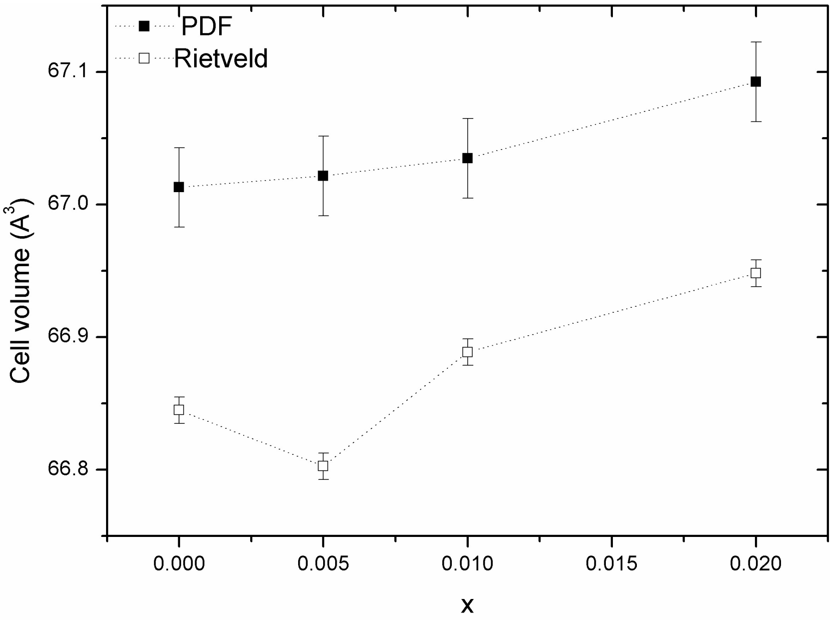

Figure 4.10: Comparison of the cell volumes as a function of Y content for Rietveld and average PDF refinements. The dotted lines are just guides for the eye.

4.4.2 TEM observations

HRTEM observations have been made on the pure zirconia sample, with the double aim of directly checking particle size and homogeneity of size distribution, and of controlling the degree of disorder within the single particles. Fig. 4.11 shows a high resolution image (and the corresponding bright field image) for the undoped zirconia: the particle size (better measurable in the bright field image) is around 10-12 nm on average (other images were also counted), in good agreement with the crystallite size results from the Rietveld refinements. This matches with the fact that nanocrystals are usually single crystals, with a small contribution from microstrains. Moreover, the size distribution can be considered quite homogeneous, as the variations in particle size are usually very small.

4.4.3 PDF refinements

For a better understanding of the local bond distances in zirconia (and their relationship with the corresponding Rietveld refined distances) the partial PDFs for the various interatomic distances, for the tetragonal structure, are plotted on Fig. 4.12. The first doublet (at 2-2.5 Å) corresponds to first coordination shell of zirconium atoms, *i.e.* to Zr–O distances. The second peak, at about 3.6 Å, is the most intense one and corresponds to Zr–Zr distances. After that, there is a doublet at about 4-4.5 Å, which is relative to the Zr–O distances, a single peak at about 5.1 Å, which represents the Zr–Zr bond, and finally another Zr–O doublet at about 5.5 Å. The contributions arising from O–O interactions are much smaller, due to the atomic scattering factors.

The PDFs of the samples here investigated were all obtained with a Q_{max} of 22.5 Å^{-1}. They look very similar to each other (Fig. 4.13), as a whole as well as locally.

The first coordination shell is displayed in the left hand side of the figure, in an enlarged scale. Two peaks are clearly visible (indicated by the arrows) for all the sample compositions: the first is located at $r \simeq$ 2.12 Å and has a bigger area than the second one, which is present at $r \simeq$ 2.46 Å. This latter peak could be taken as an artifact, as are the oscillations nearby; in order to verify if this peak was real, the Q_{max} of the Fourier transform procedure

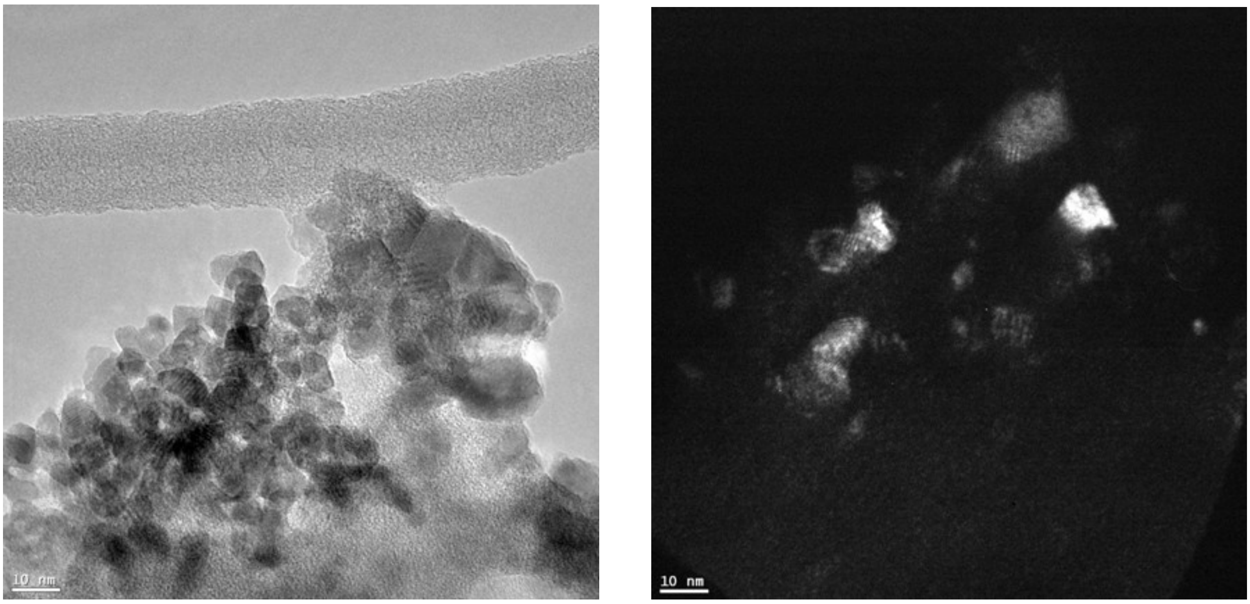

Figure 4.11: TEM images of the undoped sample: the image on the right is the bright field version of the top part of the left hand side one, allowing the particle size to be better measured.

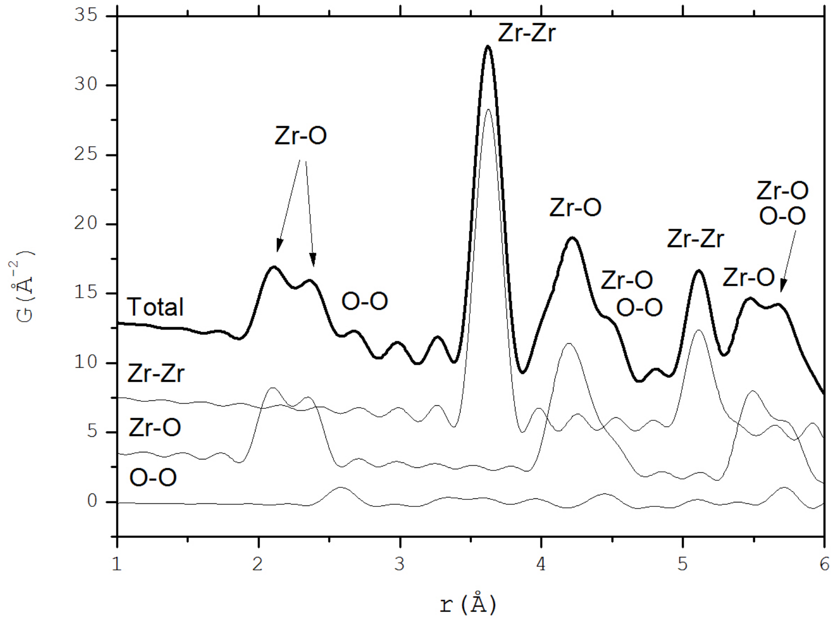

Figure 4.12: Zr–Zr, Zr–O, O–O partials, superposed to the total G(r) , as calculated from the starting tetragonal model.

was roughly changed to different values (in the range of 20-25 Å^{-1}), and new patterns relative to the same samples were obtained: the peak was always well visible, thus it can be attributed for sure to the sample contribution. The ratio between the areas of first and second peak could refer to a local environment with 6 equivalent Zr–O bonds, 2.12 Å long, and 2 other equivalent Zr–O bonds, 2.46 Å long. There are no significant differences due to Y doping, as all the main features are present (and are closely similar) for doped as well as for undoped samples. In particular, the position of the two peaks does not change significantly with composition. The second peak, however, becomes less intense and wider with increasing Y content, a possible indication of slightly different local disorder in the various samples.

In order to compare results with those obtained from the Rietveld refinements, PDF analyses were performed

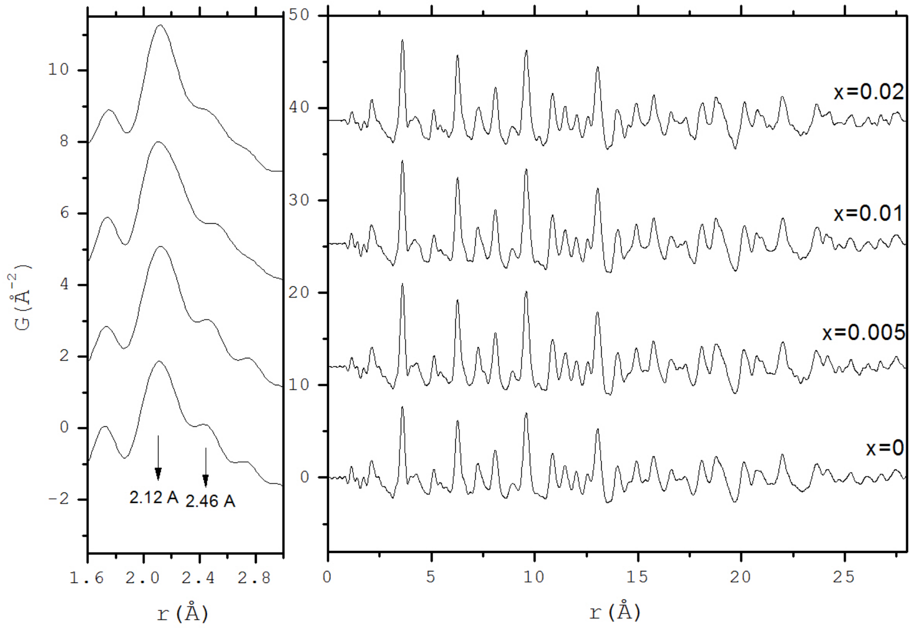

Figure 4.13: Comparison of the PDFs of the various samples.

keeping refined the same parameters refined with the Rietveld method (*i.e.* the symmetry constrains of the space group were kept). The general fit of the PDF data shows a good agreement with the tetragonal structure for $r > 10$ Å, while, below this distance, the accordance is much worse (see the grey rectangle on Fig. 4.14, which represents the pure zirconia powder). This discrepancy assesses the presence of local structural distortions (below $r < 10$ Å) in the nanocrystalline samples, thus the two regions (below and above 10 Å) must be refined with different structural models, which are hereafter discussed.

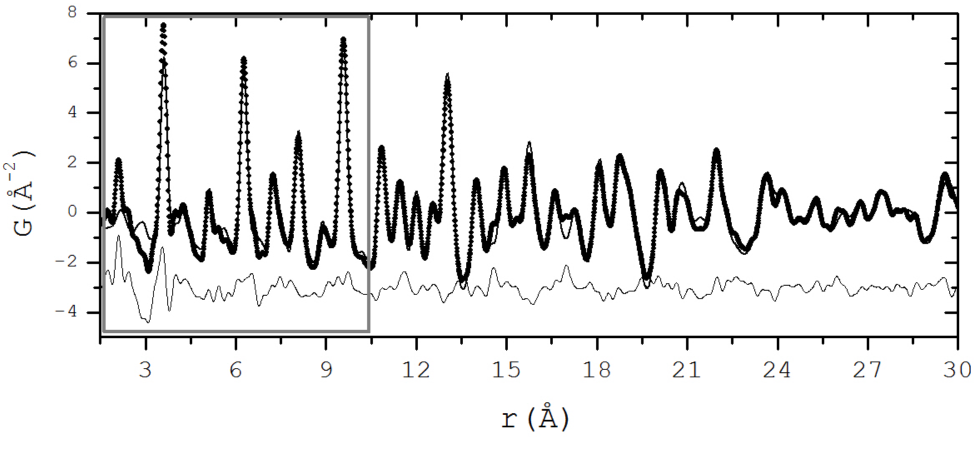

Figure 4.14: Fit of the PDF data from $r = 1$ to $r = 30$ Å with the same tetragonal structure used for Rietveld refinements in the pure zirconia sample.

The average region ($r > 10$ Å) can be refined in a straightforward manner with the tetragonal model used in the Rietveld refinement. In the two refinements, the same parameters are left free for optimization and the structure underlying the PDF refinements is constrained to the space group $P4_2/nmc$. An example of the PDF fit is shown in Fig. 4.15, and the numerical results are reported in Table 4.2. The Table does not report the esd of the results of the PDF refinements, as the PDFgui software does not provide reliable esd on the refined parameters when the data file does not include the esd of the measured diffracted intensities. Error on the parameters, however, may be estimated to be about 10 times larger than the corresponding errors given by Rietveld refinement. The difference curve in Fig. 4.15, as well as the R_w values given in Table 4.2 are not particularly satisfying: this can be ascribed to the fact that the PDF refinments were performed by refining only the structural parameters refined with the Rietveld method.

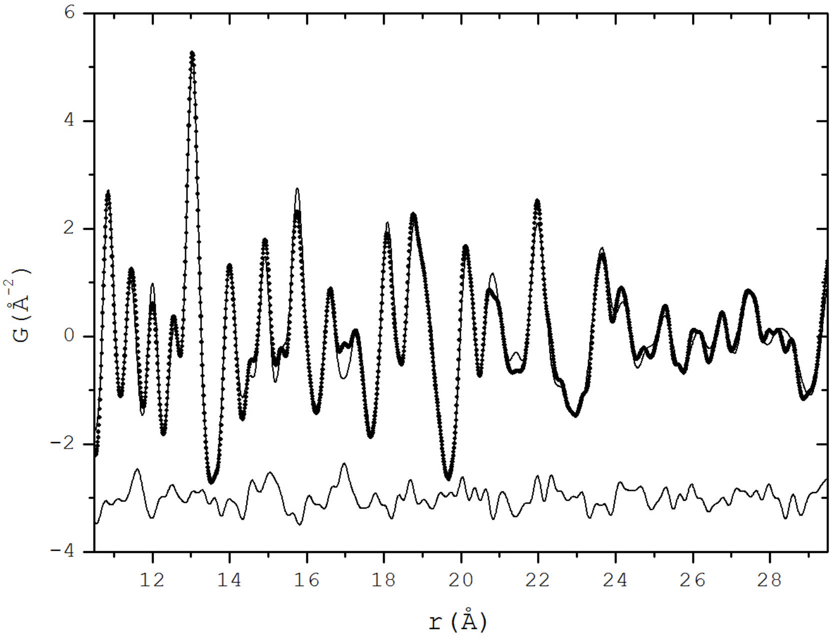

Figure 4.15: PDF fit of the undoped zirconia in the average region (r_{min} = 10 Å, r_{max} = 30 Å). The black dots are the experimental data and the curve below the graph is the difference between calculated and experimental PDFs.

Table 4.2: PDF refinements results in the average region (r_{min} = 10 Å, r_{max} = 30 Å).

Sample	a (Å)	c (Å)	U(Zr, Y) (Å^2)	U(O) (Å^2)	X(O)	R_w (%)
Y0	3.5997	5.1719	0.0043	0.010	0.281	18.3
Y0.005	3.5999	5.1717	0.0042	0.011	0.281	19.8
Y0.01	3.6013	5.1687	0.0044	0.011	0.280	18.9
Y0.02	3.6024	5.1700	0.0046	0.012	0.279	20.1

The results in Table 4.2 are in good agreement with those coming from the Rietveld refinements (Table 4.1), even for what concerns the oxygen coordinate, and this is considered a great outcome, as nanocrystalline samples provide very broad peaks in the diffraction patterns and so big troubles in the structural analyses are commonly encountered. In particular, the cell volumes obtained applying the tetragonal model to Rietveld and PDF refinements show very negligible differencies (within $\sim 2\sigma$; look at Fig. 4.10), validating the PDF refinements in the average region and the use of the tetragonal model itself, also given that Rietveld cell refinement is a much more accurate approach.

Going now to the local structure (the region below 10 Å), the first step is to identify the most appropriate structural model for properly refining the PDF features. To that purpose, the local environments of the Zr atoms were analysed by considering three different crystal systems: the tetragonal structure, where there are two sets of 4 equal Zr–O distances, which corresponds to two PDF peaks of equal intensity; the orthorhombic system, where 9 distances are encoutered, 7 of them are centred between 2.1 and 2.2 Å and the other 2 are represented at about 2.5 Å; the monoclinic structure, in which 7 slightly different Zr–O distances are observed, merging into a single

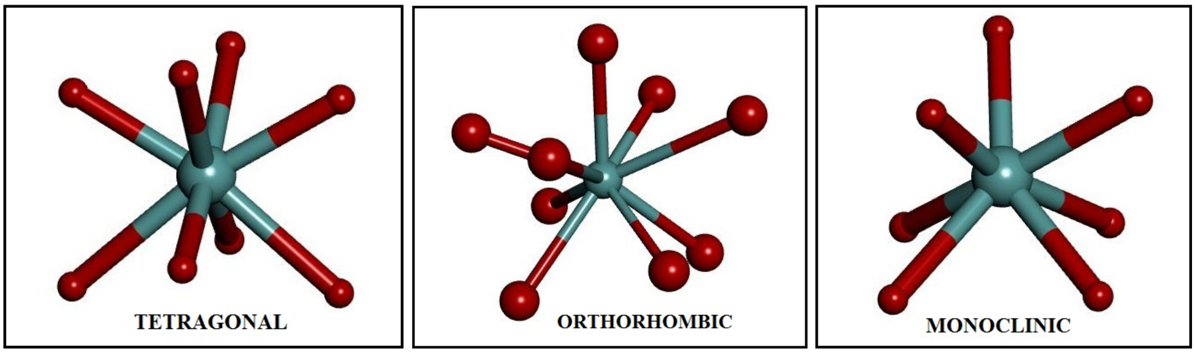

Figure 4.16: Local environment of the Zr atoms in the tetragonal, orthorhombic and monoclinic crystal systems. Figures are made with Discovery Studio 3.5 (Accelerys Software Inc.).

PDF peak. This descriptions can be easily deduced from Fig. 4.1 or, better, from Fig. 4.16.

In the experimental data, the first two peaks, with noticeably different intensities, suggest the presence, in the first coordination shell of zirconium, of two different sets of Zr–O distances. This agrees neither with the tetragonal structure (two peaks with equal intensities), nor with the monoclinic one (a single PDF peak). This line of thinking is graphically shown by Fig. 4.17, where the experimental data are compared with the structural models in the three cases: the structural data are directly taken from the corresponding CIF files, without performing any refinement.

In the average region, the best agreement is given by the tetragonal model, while, in the local region, the orthorhombic model is the only one that agrees with the feature of PDF at the Zr–O closest distances. The regions with the best agreement with the structural models are highlighted with grey rectangles in Fig. 4.17, and have been used in a carbox type approach in order to reach a more detailed understanding of the local structure of the materials under study.

Fig. 4.18 (upper part) shows a detail of the fit of a single tetragonal model in the region between 1 and 10 Å. It can be clearly seen that the correspondence is poor, especially at $r < 3$ Å. Instead, the orthorhombic model gives, in the very local region, the satisfying results represented in the lower left part of Fig. 4.18; the rest of the PDF is fitted with two slightly different tetragonal models, which are reported on the right of the orthorhombic model, in the same figure.

Table 4.3 shows the results obtained from a PDF refinement in the low-r region (r_{max} = 3 Å), with the use of the orthorhombic structural model. As it can be seen, the R_w values do not look so good, but it must be considered that the refinement is done in a very narrow range of distances, so that a large weight is given to the smallest uncertainties when trying to fit the termination ripples. The narrow r range also makes it impossible to refine any structural parameter (*i.e.* oxygen coordinate).

Since the second, less intense, peak decreases in intensity with increasing Y content, the same r range was also refined using the monoclinic model: the difference in R_w between the monoclinic and the orthorhombic refinements are reported in the last column in Table 4.3. This value decreases as a function of Y content and this tendency could indicate that the monoclinic structure becomes more and more likely as the Y content increases, in keeping with the results obtained by Gateshki et al. (2006 & 2007).

The last part of the local range, *i.e.* the r range from 3 to 10 Å, was then refined separately, using a single tetragonal model. The results are illustrated in the upper part of Table 4.4: the R_w values are not so good and the oxygen thermal factors are much larger than they should be in an undistorted structural environment. When structural distortions are present, in fact, the residuals can be reduced by simply increasing the atomic thermal factors. In order to improve the fit (and to reduce this effect), the r range is further divided into two regions:

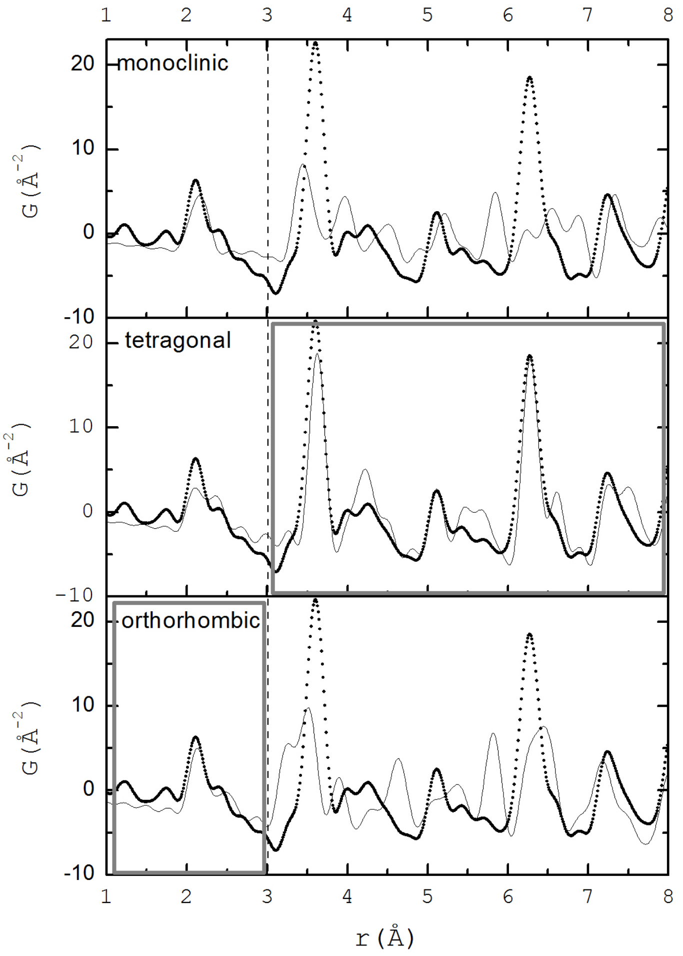

Figure 4.17: Models for the local structure: comparison with experimental PDF (dots) of the monoclinic, tetragonal and orthorhombic models (no refinement made). The grey boxes show the best agreement between the model and the experimental data in the two low-r regions.

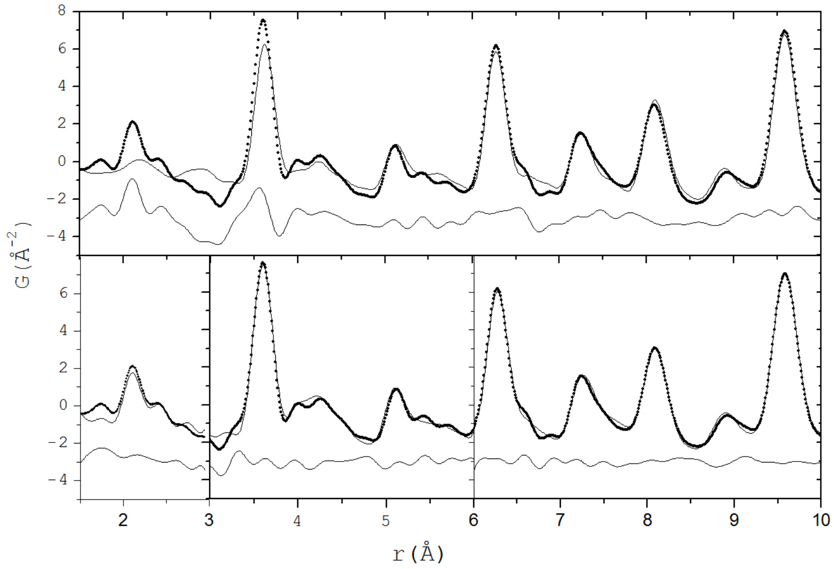

Figure 4.18: Carbox approach for PDF refinement.

Table 4.3: Fit with the orthorhombic model in the low-r region (r_{max} = 3 Å). The last column reports the difference in R_w between the refinements done with the monoclinic and the orthorhombic models.

Sample	a (Å)	b (Å)	c (Å)	U(Zr, Y) (Å^2)	U(O) (Å^2)	R_w (%)	ΔR_w (%)
Y0	5.5552	6.3073	3.0399	0.001	0.001	46.7	9.0
Y0.005	5.5777	6.3486	3.0327	0.001	0.005	47.9	6.9
Y0.01	5.5655	6.3613	3.0472	0.001	0.003	49.0	2.9
Y0.02	5.5734	6.3759	3.0510	0.001	0.002	47.9	3.9

both of them are fitted with the tetragonal model, but in an independent way, so that the results of the refinements are different from each other (see middle and lower part of Table 4.4). As it can be clearly seen, the R_w values become much better, with smaller (and more reasonable) values for oxygen thermal parameters. The goodness of fit can be visually appreciated in the lower part of Figure 4.18 and of Table 4.4. Moreover, it should be noticed that $c/a\sqrt{2}$, which describes the degree of tetragonality, *i.e.* the tetragonal distortion, is smaller for the second tetragonal portion (from 6 to 10 Å) with respect to the first one (3-6 Å) and that the oxygen coordinate is larger and more similar to that of the average structure, leading to a distortion less pronounced when r is near 10 Å.

Table 4.4: Carbox approach. Upper part shows the refinement between 3 and 10 Å, the middle the refinement between 3 and 6 Å and the lower the refinement between 6 and 10 Å.

Sample	a (Å)	c (Å)	U(Zr, Y) (Å^2)	U(O) (Å^2)	X(O)	R_{wp} (%)
r = 3–10 Å						
Y0	3.5822	5.2052	0.006	0.06	0.239	16.6
Y0.005	3.6103	5.1409	0.007	0.03	0.204	17.6
Y0.01	3.6084	5.1465	0.007	0.06	0.223	18.0
Y0.02	3.6289	5.0949	0.007	0.06	0.222	18.2

Sample	a (Å)	c (Å)	$c/a\sqrt{2}$	U(Zr, Y) (Å^2)	U(O) (Å^2)	X(O)	R_{wp} (%)
r = 3–6 Å							
Y0	3.5812	5.1580	1.018	0.005	0.02	0.185	13.3
Y0.005	3.5808	5.1616	1.019	0.005	0.03	0.191	12.2
Y0.01	3.5778	5.1640	1.021	0.005	0.03	0.187	11.2
Y0.02	3.5866	5.1360	1.013	0.006	0.03	0.190	13.1
r = 6–10 Å							
Y0	3.6156	5.1354	1.004	0.007	0.04	0.201	15.4
Y0.005	3.6132	5.1401	1.006	0.007	0.03	0.195	10.1
Y0.01	3.6015	5.1782	1.017	0.007	0.04	0.208	9.1
Y0.02	3.6202	5.1279	1.002	0.008	0.04	0.204	10.1

Summarizing, the carbox approach gives a model for the local distortions in the zirconia samples, composed by an orthorhombic structure in the very low-r region (r < 3 Å) and two tetragonal models, which slightly change in the cell parameters, in r ranges of 3-6 Å and 6-10 Å. These two different tetragonal distortions are necessary, in the nanocrystals, to relax the Zr–O bonds into the average structure: indeed, both the orthorhombic and the double tetragonal local environments can match the 4+4 distances of the ideal tetragonal structure, which is, actually, the resulting average structure of the investigated samples.

The local, low symmetry, distortions may be responsible for the room temperature stabilization of the undoped tetragonal phase. Below the critical particle size of ∼25 nm (the samples studied here are about 10 nm), most of the bonds are near the surface of the particle, with a certain degree of relaxation needed. A lower symmetry distortion, such as the orthorhombic one (but it could be also monoclinic, as found by Gateshki et al. (2006 & 2007), and as seen in the samples here discussed with higher Y content), may come on help, with a different number of Zr–O bonds, in the relaxation process. This, in turn, may be render the high temperature crystal structure the more favorable at room temperature. Moreover, Garvie (1965 & 1978) explained the great role played by strain in the stabilization of the HT phase. Total RMS strain in the measured samples is of the order of 10^{-3}. The presence of two different tetragonal distortions and of a low symmetry one (either orthorhombic or monoclinic) can certainly increase the local strain level. The influence of local strain in structure relaxation may therefore give rise to the stabilization of the tetragonal polymorph, likely through the reduction of surface free energy.

4.5 Conclusions

The undoped (or lightly doped) zirconia samples produced during this research work are very similar to each other, either in their powder diffraction features, or in the effect of diffuse scattering on their PDFs. Their crystallite size and their RMS strain are similar to each other, and comparable to those obtained by direct TEM observations on the undoped sample. The refinements of the PDFs in the average region (above 10 Å) are in good agreement with the Rietveld refinements results on the same data. The local region, however, cannot be fitted with the crystallographic tetragonal model, owing to the presence of a lower-symmetry distortion in the first coordination shell (Zr–O bond). This region can be fitted with an orthorhombic model, which gives particularly good results. The rest of the local region in the PDF can be fitted with the tetragonal model, but, in a carbox approach, two slightly different models should be used in order to produce the best results. Regarding these local distortions, there are no differences among the samples, depending on the Y content, with respect to the undoped one: the undoped sample has exactly the same behaviour as samples with low Y content. These distortions originate therefore in the very small grain size, and likely in surface relaxation effects, rather than in the effect of the dopant in the structure. The match between different local distortions increases the strain level, which can be the reason of the stabilization of the tetragonal structure. The results on the nanocrystalline zirconia samples are in good agreement with previous results with the same technique, as well as with results obtained with other local techniques (such as EXAFS).

Part IV

Final conclusions and references

Chapter 5

Final conclusions

Particle size reduction and nanocrystallinity are two widely studied factors in scientific disciplines, such as chemistry, physics, biology, etc., and particularly in the field of material science, as their effects lead to peculiar behaviours in materials undergoing non-ambient conditions, and so produce challenging variations in the physical properties, which can be tuned through controlled industrial procedures in order to provide the desired characteristics to the materials. Therefore, understanding the influence of changing particle size is crucial when one deals with phase transitions of functional minerals.

In the present thesis it has been explored the world of micrometric quartz used as raw material in traditional ceramics as well as that of nanomaterials employed in electronics and energetics. When particle size is varied, all the objects studied here were found to gain important features, in terms of different behaviours during phase transitions induced by changes in environmental temperature. For example, zirconia in its tetragonal form is stabilized at room conditions when the crystallite size is below the critical diameter, *i.e.* about 25 nm [Garvie, 1978] and this lowering of tetragonal-to-monoclinic transition temperature is explained by a non-hydrostatic stress effect. In the study presented in Chapter 4, indeed, it was possible to synthesize monophasic tetragonal zirconia stable at ambient conditions, with crystallite size of about 10 nm. Moreover, it is argued that the nanocrystallinity of these samples and the resulting strains are the reason of the stabilization of tetragonal structure, as average, and of orthorhombic structure, together with two slightly different tetragonal environments, in the local region ($r < 10$ Å).

Strain has a driving role also in the structural phase transition occurring at low temperature in half-doped La, Ca manganites: in fact, it is believed that the suppression of shear strain in nanocrystalline pellets is responsible for the suppression of charge ordering; nevertheless, a freezing process in nano samples was observed, proving the presence of local Jahn-Teller distortions within their structure. Therefore, the reduction of size induces different behaviours also in this kind of material, and this belief is verified also when inspecting magnetic transitions: while the nano samples undergo only the paramagnetic–ferromagnetic transition between $\sim$270 K and $\sim$280 K, in the bulk sample it is observed not only the paramagnetic–ferromagnetic transition occurring at lower temperature (near 260 K), but also a huge hysteresis pattern attributed to the ferromagnetic–antiferromagnetic phase transition in the range 125-180 K.

The influence of particle size in mineral transformations is confirmed also by heating quartz powders: the decrease of crystallization temperature of cristobalite and tridymite (when mineralizers are added to the system) is always promoted by small grain sizes, which tend to accelerate the occurring reactions.

On the ground of all these considerations, it is obvious that solid state reactivity and phase transitions can be driven through control of particle size. If a system is well known, the choice of appropriate working temperatures and times and of starting raw materials can be made, yielding to the stabilization of the desired structural form as well as the required physical properties of the final product, so to make it suitable for the requisite application.

Chapter 6

References

L. M. Acuna, D. G. Lamas, R. O. Fuentes, I. O. Fabregas, M. C. A. Fantini, A. F. Craievich & R. J. Prado (2010). "Local atomic structure in tetragonal pure ZrO_2 nanopowders", *J. Appl. Crystallogr.*, **43**, 227–36.

O. Alharbi, D. Zaki & E.Hamzawy (2012). "Effect of TiO_2, LiF and Cr_2O_3 in the crystallization of cristobalite and tridymite in sintered glass-ceramics", *Silicon*, **4**, 281–7.

U. Anselmi-Tamburini, F. Maglia &, I. G. Tredici (2012). "Field assisted sintering of nanometric ceramic materials", *Ceram. Trans.*, **232**, 133–49.

M. Auslender, C. E. Lee, E. Rozenberg, A. I. Shames, D. Mogilyansky, E. Sominski & A. Gedanken (2010). "Nanometric size on magnetic ordering in half-doped $La_{0.5}Ca_{0.5}MnO_3$ manganite: EPR probing", *J. Kor. Phys. Soc.*, **57**, 1559–62.

M. Avrami (1939). "Kinetics of phase change: I. General theory", *J. Chem. Phys.*, **7**, 1103–12.

M. Avrami (1940). "Kinetics of phase change: II. Transformation-time relations for random distribution of nuclei", *J. Chem. Phys.*, **8**, 212–24.

M. Avrami (1941). "Granulation, phase change and microstructure. Kinetics of phase change: III", *J. Chem. Phys.*, **9**, 177–84.

A. Banerjee, K. Kumar & P. Chaddah (2008). "Enhancement of equilibrium fraction in$La_{0.5}Ca_{0.5}MnO_3$ by recrystallization", *J. Phys.: Cond. Matter*, **20**, 255245 .

B. I. Belevtsev, G. A. Zvyagina, K. R. Zhekov, I. G. Kolobov, E. Yu. Beliayev, A. S. Panfilov, N. N. Galtsov, A. I. Prokhvatilov & J. Fink-Finowicki (2006). "Influence of magnetic field on paramagnetic-ferromagnetic transition in $La_{1-x}Ca_xMnO_3$ (x $\approx$ 0.25) crystal: ultrasonic and transport studies", *Phys. Rev. B*, **74**, 054427.

A. Bernasconi, V. Diella, A. Pagani, A. Pavese, F. Francescon, K. Young, J. Stuart & L. Tunnicliffe (2011). "The role of firing temperature, firing time and quartz grain size on phase-formation, thermal dilatation and water absorption in sanitary-ware vitreous bodies", *J. Eur. Ceram. Soc.*, **31**(8), 1353–60.

S. J. L. Billinge & M. G. Kanatzidis (2004). "Beyond crystallography: the study of disorder, nanocristallinity and crystallographically challenged matrials with pair distribution functions", *Chem. Commun.*, **7**, 749–60.

N. S. Bingham, P. Lampen, M. H. Phan, T. D. Hoang, H. D. Chinh, C. L. Zhang, S. W. Cheong & H. Srikanth (2012). "Impact of nanostructuring on the magnetic and magnetocaloric properties of microscale phase-separated $La_{5/8-y}Pr_yCa_{3/8}MnO_3$ manganites", *Phys. Rev. B*, **86**, 064420.

A. Biswas, I. Das & C. Majumdar (2005). "Modification of the charge ordering in $Pr_{0.5}Sr_{0.5}MnO_3$ nanoparticles", *J. Appl. Phys.*, **98**, 124310.

M. J. Buerger (1954). "The stuffed derivatives of the silica structures", *Amer. Mineral.*, **39**, 600–614.

G. Cao, J. Zhang, S. Wang, J. Yu, C. Jing, S. Cao & X. Shen (2006). "Reentrant spin glass behavior in CE-type

AFM $Pr_{0.5}Ca_{0.5}MnO_3$ manganite", *J. Magn. Magn. Mater.*, **301**, 147–54.

M. A. Carpenter (1992). "Thermodynamics of phase transitions in minerals: a macroscopic approach", in: *Stability of minerals*, Vol. 3 The Mineralogical Society Series, 172–215. Chapman & Hall, London.

M. A. Carpenter (2007). "Elastic anomalies accompanying phase transitions in (Ca,Sr)TiO_3 perovskites: Part I. Landau theory and a calibration for $SrTiO_3$", *Am. Mineral.*, **92**, 309–27.

M. A. Carpenter, A. I. Becerro & F. Seifert (2001). "Strain analysis of phase transitions in (Ca,Sr)TiO_3 perovskites", *Am. Mineral.*, **86**, 348–63.

M. A. Carpenter, J. F. J. Bryson, G. Catalan, S. J. Zhang & N. J. Donnelly (2012). "Elastic and anelastic relaxations in the relaxor ferroelectric $Pb(Mg_{1/3}Nb_{2/3})O_3$: I. Strain analysis and a static order parameter", *J. Phys.: Cond. Matter*, **24**, 045902.

M. A. Carpenter, C. J. Howard, R. E. A. McKnight, A. Migliori, J. B. Betts & V. R. Fanelli (2010a). "Elastic and anelastic relaxations associated with the incommensurate structure of $Pr_{0.48}Ca_{0.52}MnO_3$", *Phys. Rev. B*, **82**, 134123.

M. A. Carpenter, R. E. A. McKnight, C. J. Howard & K. S. Knight (2010b). "Symmetry and strain analysis of structural phase transitions in $Pr_{0.48}Ca_{0.52}MnO_3$", *Phys. Rev. B*, **82**, 094101.

M. A. Carpenter, R. E. A. McKnight, C. J. Howard, Q. Zhou, B. J. Kennedy & K. S. Knight (2009). "Characteristic length scale for strain fields around impurity cations in perovskites", *Phys. Rev. B*, **80**, 214101.

M. A. Carpenter & E. K. H. Salje (1998). "Elastic anomalies in minerals due to structural phase transitions", *Eur. J. Mineral.*, **10**, 693–812.

P. Chaddah, K. Kumar & A. Banerjee (2008). "Devitrification and recrystallization of magnetic glass $La_{0.5}Ca_{0.5}MnO_3$", *Phys. Rev. B*, **77**, 100402(R).

S. Chandra, A. Biswas, S. Datta, B. Ghosh, A. K. Raychaudhuri & H. Srikanth (2013). "Inverse magnetocaloric and exchange bias effects in single crystalline $La_{0.5}Sr_{0.5}MnO_3$ nanowires", *Nanotech.*, **24**, 505712.

C. H. Chen & S-W. Cheong (1996). "Commensurate to incommensurate charge ordering and its real-space images in $La_{0.5}Ca_{0.5}MnO_3$", *Phys. Rev. Lett.*, **76**, 4042–5.

C. X. Chen, G. S. Jiang, J. L. Jiang, Q. L. Zhang & R. K. Zheng (2007). "Elastic-effects study of charge-ordering transition in $La_{0.25}Ca_{0.75}MnO_3$ perovskite", *J. Magn. Magn. Mater.*, **308**, 71–3.

C. X. Chen, J. Y. Zheng, Y. Y. Jiang, J. Li & R. K. Zheng (2010). "Elastic anomalies in the perovskite manganite $La_{0.5}Ca_{0.5}MnO_3$", *Physica B*, **405**, 2088–90.

C. X. Chen, R. K. Zheng, T. Qian, Y. Liu & X. G. Li (2005). "Charge ordering correlated elastic anomalies in $La_{1-x}Ca_xMnO_3$ perovskite", *J. Phys. D: Appl. Phys.*, **38**, 807–10.

X. B. Chen, J. S. Zhu, G. H. Hwang, C. M. Fu, H. M. Duh, C. H. Lin, W. S. Gao, X. Y. Mao & Y. N. Wang (1999). "A mechanical investigation on the phase transition behavior of $La_{0.7}Ca_{0.3}MnO_{3-\delta}$ ceramics", *Phys. Stat. Sol. a*, **173**, 451–7.

P. M. Chowdhury, B. Ghosh, A. K. Raychaudhuri, S. D. Kaushik & V. Siruguri (2013). "Stability of charge and orbital order in half-doped $Y_{0.5}Ca_{0.5}MnO_3$ nanocrystallites", *J. Nanopart. Res.*, **15**, 1585.

D. R. Clarke & S. R. Phillpot (2005). "Thermal barrier coating materials". *Mater. Today*, **8**, 22–9.

S. Cox, J. C. Lashley, E. Rosten, J. Singleton, A. J. Williams & P. B. Littlewood (2007). "Evidence for the charge-density-wave nature of the stripe phase in manganites ", *J. Phys.: Cond. Matter*, **19**, 192201.

S. Cox, J. C. Loudon, A. J. Williams, J. P. Attfield, J. Singleton, P. A. Midgley & N. D. Mathur (2008). "Very weak electron-phonon coupling and strong strain coupling in manganites", *Phys. Rev. B*, **78**, 035129.

J. M. Criado, M. Gonzales & C. Real (1986). "Correlation between crystallite size and microstrains in materials subjected to thermal and/or mechanical treatments", *J. Mater. Sci. Lett.*, **5**, 467–9.

M. Dapiaggi, G. Artioli, C. Righi & R. Carli (2007). "High temperature reactions in mold flux slags: kinetic *versus* composition control", *J. Non-Cryst. Solids*, **353**(30–31), 2852–60.

M. Dapiaggi, F. Maglia, I. Tredici, B. Maroni, G. Borghini & U.A. Tamburini (2010). "Complex thermal evolution of size-stabilized tetragonal zirconia", *J. Phys. Chem. Solids*, **71**, 1038–41.

M. D'Incau, M. Leoni & P. Scardi (2007). "High-energy grinding of FeMo powders", *J. Mater. Res.*, **22**, 1744–53.

D. S. Dos Santos & D. R. Dos Santos (2002). "Crystallization kinetics of Fe–B–Si metallic glasses", *J. Non-Cryst. Solids*, **304**(1–3), 56–63.

T. Egami & S. J. L. Billinge (2003). "Underneath the Bragg peaks: structural analysis of complex materials", Vol. 7 Pergamon Materials Series. Pergamon, New York.

C. L. Farrow, P. Juhas, J. W. Liu, D. Bryndin, E. S. Bozin, J. Bloch, T. Proffen & S. J. L. Billinge (2007). "PDFfit2 and PDFgui: computer programs for studying nanostructure in crystals", *J. Phys. Condens. Matter*, **19**, 335219(1–7).

Y. Fei (1995). "Thermal expansion", in: *Mineral Physics and Crystallography: a Handbook of Physical Constants*. American Geophysical Union, Washington DC.

C. N. Fenner (1913). "The stability relations of the silica minerals", *Amer. J. Sci.*, **36**, 331–84.

S. Ferrari & A. Gualtieri (2006). "The use of illitic clays in the production of stoneware tile ceramics", *Appl. Clay Sci.*, **32**, 73–81.

M. Ferrari & L. Lutterotti (1994). "Method for the simultaneous determination of anisotropic residual stresses and texture by X-ray diffraction", *J. Appl. Phys.*, **76**(11), 7246–55.

P. A. Fleury & K. Lyons (1981). "Optical Studies of Structural Phase Transitions" in: *Structural phase transitions I*, Vol. 23 Topics in Current Physics. Springer, Berlin.

O. W. Flörke (1956). "The unicomponent system SiO_2", *Naturwissenschaften*, **43**, 419–20.

O. W. Flörke & H. Schneider (1986). "Intergrowth relationships between the silica polymorphs quartz, cristobalite and tridymite in silica-rich ceramic materials", *Ceram. Forum Inst.*, **63**, 368–72.

R. S. Freitas, L. Ghivelder, F. Damay, F. Dias & L. F. Cohen (2001). "Magnetic relaxation phenomena and cluster glass properties of $La_{0.7-x}Y_xCa_{0.3}MnO_3$ manganites", textitPhys. Rev. B, **64**, 144404.

R. S. Freitas, L. Ghivelder, P. Levy & F. Parisi (2002). "Magnetization studies of phase separation in $La_{0.5}Ca_{0.5}MnO_3$", *Phys. Rev. B*, **65**, 104403.

A. N. Fitch (2004). "The high resolution powder diffraction beam line at ESRF", *J. Res. Natl. Inst. Stand. Technol.*, **109**, 133.

H. Fujishiro, T. Fukase & M. Ikebe (2001). "Anomalous lattice softening at x = 0.19 and 0.82 in $La_{1-x}Ca_xMnO_3$", *J. Phys. Soc. Jpn.*, **70**, 628–31.

H. Fujishiro, M. Ikebe, T. Kikuchi & T. Fukase (2006). "Anomalous sound velocity behavior of $La_{1-x}Ca_xMnO_3$ (x $\sim$ 0.48) in applied field", *Physica B*, **378–380**, 518.

A. K. Galwey & M. E. Brown (1998). "Thermal decomposition of ionic solids", Vol. 86 Studies in Physical and Theoretical Chemistry. Elsevier, Amsterdam.

J. L. García-Muñoz, A. Llobet, C. Frontera & C. Ritter (1999). "Charge localization and magnetic dynamics in ferromagnetic and charge-ordered manganites", *J. Appl. Phys.*, **85**, 5639–41.

R. C. Garvie (1965). "The occurrence of metastable tetragonal zirconia as a crystallite size effect", *J. Phys. Chem.*, **69**, 1238–43.

R. C. Garvie (1978). "Stabilization of the tetragonal structure in zirconia microcrystals". *J. Phys. Chem.*, **82**, 218–24.

M. Gateshki, M. Niederberger, A. S. Deshpande, Y. Ren & V. Petkov (2007). "Atomic scale structure of nanocrystalline CeO_2-ZrO_2 oxides by total X-ray diffraction and pair distribution function analysis", *J. Phys. Condens. Matter*, **19**, 156205/1.

M. Gateshki, V. Petkov, T. Hyeon, J. Joo, M. Niederberger & Y. Ren (2006). "Interplay between the local structural disorder and the length of structural coherence in stabilizing the cubic phase in nanocrystalline ZrO_2", *Solid State Commun.*, **138**, 279–84.

M. Gateshki, V. Petkov, G. Williams, S. K. Pradhan & Y. Ren (2005). "Atomic-scale structure of nanocrystalline ZrO2 prepared by high-energy ball milling", *Phys. Rev. B*, **71**, 224107.

B. Ghosh, V. Siruguri, A. K. Raychaudhuri & T. Chatterji (2014). "Effect of size reduction on the structural and magnetic order in $LaMnO_{3+\delta}$ (δ approximate to 0.03) nanocrystals: a neutron diffraction study", *J. Phys.: Cond. Matter*, **26**, 025603.

E. Granado, N. O. Moreno, A. Garcia, J. A. Sanjurjo, C. Rettori, I. Torriani, S. B. Oseroff, J. J. Neumeier, K. J. McClellan, S-W. Cheong & Y. Tokura (1998). "Phonon Raman scattering in $R_{1-x}A_xMnO_{3+\delta}$ (R = La, Pr; A = Ca, Sr)", *Phys. Rev. B*, **58**, 11435–40.

A. Gualtieri (2000). "Accuracy of XRPD QPA using the combined Rietveld-RIRmethod", *J Appl Crystallogr*, **33**, 267–78.

A. Gualtieri, M. Bellotto, G. Artioli & S.M. Clark (1995). "Kinetic study of the kaolinite-mullite reaction sequence", *Phys. Chem. Miner.*, **22**(4), 215–22.

A. F. Gualtieri, M. Gemmi & M. Dapiaggi (2003). "Phase transformations and reaction kinetics during the temperature-induced oxidation of natural olivine", *Am. Mineral.*, **88**(10), 1560–74.

T. K. Gupta & J. Jau-Ho (1994). "Origin of cristobalite formation during sintering of a binary mixture of borosilicate glass and high silica glass", *J. Matter. Res.*, **9**(4), 999–1005.

P. J. Heaney (1994). "Structure and chemistry of the low-pressure silica polymorphs", in: *Silica: Physical Behavior, Geochemistry and Materials Applications*, Vol. 29 Reviews in Mineralogy. Mineralogical Society of America Publication, Washington DC.

V. Hill & R. Roy (1958). "Silica structure studies VI. On tridymites", *Trans. Br. Ceram. Soc.*, **57**, 496–510.

S. B. Holmquist (1958). "A note on the sluggish silica transformations", *Zeit. Krist.*, **111**, 71–6.

C. J. Howard, Z. Zhang, M. A. Carpenter & K. S. Knight (2007). "Suppression of strain coupling in perovskite $La_{0.6}Sr_{0.1}TiO_3$ by cation disorder", *Phys. Rev. B*, **76**, 054108.

A. M. Hu, M. Li & D. L. Mao (2007). "Crystallization of spodumene-diopside in the las glass ceramics with CaO and MgO addition", *J. Therm. Anal. Calorim.*, **90**(1), 185–9.

Q. Huang, J. W. Lynn, R. W. Erwin, A. Santoro, D. C. Dender, V. N. Smolyaninova, K. Ghosh & R. L. Greene (2000). "Temperature and field dependence of the phase separation, structure, and magnetic ordering in $La_{1-x}Ca_xMnO_3$ (x = 0.47, 0.50, and 0.53)", *Phys. Rev. B*, **61**, 8895.

Z. Jirak, E. Hadova, O. Kaman, K. Knizek, M. Marysko, E. Pollert, M. Dlouha & S. Vratislav (2010). "Ferromagnetism *versus* charge ordering in the $Pr_{0.5}Ca_{0.5}MnO_3$ and $La_{0.5}Ca_{0.5}MnO_3$ nanocrystals", *Phys. Rev. B*, **81**, 024403.

P. Juhas, T. Davis, C. L. Farrow & S. J. L. Billinge (2013). "PDFgetX3: a rapid and highly automatable program for processing powder diffraction data into total scattering pair distribution functions", *J. Appl. Crystallogr.*, **46**, 560–6.

Kallias G, Pissas M & A. Hoser (2000). "Neutron diffraction study of $La_{0.5}Ca_{0.5}MnO_3$ under an external magnetic field", *Physica B*, **276-278**, 778–9.

V. V. Kharton, F. M. B. Marques & A. Atkinson (2004). "Transport properties of solid oxide electrolyte ceramics: a brief review", *Solid State Ionics*, **174**, 135–49.

A. Khawam & D. R. Flanagan (2006). "Solid-state kinetic models: Basics and mathematical fundamentals", *J. Phys. Chem. B*, **110**, 17315–28.

M. Kim, X. M. Chen, X. Wang, C. S. Nelson, R. Budakian, P. Abbamonte & S. L. Cooper (2011). "Pressure and field tuning the magnetostructural phases of Mn3O4: Raman scattering and x-ray diffraction studies", *Phys. Rev. B*, **84**, 174424.

N. Koga & J. M. Criado (1997). "Influence of the particle size distribution on the CRTA curves for the solid-state reactions of interface shrinkage", *J. Therm. Anal.*, **49**(3), 1477–84.

N. Koga & J. M. Criado (1998). "Kinetic analyses of solid-state reactions with a particle-size distribution", *J. Am. Ceram. Soc.*, **81**(11), 2901–9.

H. P. Klug & L. E. Alexander (1968). "X-ray diffraction procedures for polycrystalline and amorphous materials", Wiley, New York.

D. Lahiri, S. Khalid, T. Sarkar, A. K. Raychaudhuri & S. M. Sharma (2012). "XAFS investigation of the role of orientational disorder in the stabilization of the ferromagnetic metallic phase in nanoparticles of $La_{0.5}Ca_{0.5}MnO_3$", *J. Phys.: Cond. Matter*, **24**, 336001.

J. C. Loudon & P. A. Midgley (2006a). "Comparison of the ferromagnetic phase transitions in $La_{0.7}Ca_{0.3}MnO_3$ and single crystal nickel by micromagnetic imaging", *Phil Mag*, **86**, 2941–56.

J. C. Loudon & P. A. Midgley (2006b). "Micromagnetic Imaging to Determine the Nature of the Ferromagnetic Phase Transition in $La_{0.7}Ca_{0.3}MnO_3$", *Phys. Rev. Lett.*, **96**, 027214.

B. Luthi & W. Rehwald (1981). "Ultrasonic studies near structural phase transitions", in: *Structural phase transitions I*, Vol. 23 Topics in Current Physics. Springer, Berlin.

P. Levy, F. Parisi, G. Polla, D. Vega, G. Leyva, H. Lanza, R. S. Freitas & L. Ghivelder (2000). "Controlled phase separation in $La_{0.5}Ca_{0.5}MnO_3$", *Phys. Rev. B*, **62**, 6437–41.

X. G. Li, R. K. Zheng, G. Li, H. D. Zhou, R. X. Huang, J. Q. Xie & Z. D. Wang (2002). "Jahn-Teller effect and stability of the charge-ordered state in $La_{1-x}Ca_xMnO_3$ ($0.5 \leq x \leq 0.9$) manganites", *Europhys. Lett.*, **60**, 670–76.

J. C. Loudon, N. D. Mathur & P. A. Midgley (2002). "Charge-ordered ferromagnetic phase in $La_{0.5}Ca_{0.5}MnO_3$", *Nature*, **420**, 797–800.

F. Maglia, M. Dapiaggi, I. G. Tredici, B. Maroni & U. Anselmi-Tamburini (2010). "Synthesis of fully dense nanostabilized undoped tetragonal zirconia", *J. Am. Ceram. Soc.*, **93**, 2092–7.

F. Maglia, I. G. Tredici & U. Anselmi-Tamburini (2013). "Densification and properties of bulk nanocrystalline functional ceramics with grain size below 50 nm", *J. Eur. Ceram. Soc.*, **33**, 1045–66.

A. Maignan, A. Sundaresan, U. V. Varadaraju & B. Raveau (1998). "Magnetization relaxation and aging in spin-glass $(La,Y)_{1-x}Ca_xMnO_3$ (x = 0.25, 0.3 and 0.5) perovskite", *J. Magn. Magn. Mater.*, **184**, 83–8.

A. S. Mazadeh, E. S. Bozin, C. L. Farrow, G. Paglia, P. Juhas, S. J. L. Billinge, A. Karkamkar & M. G. Kanatzidis (2007). "Quantitative size-dependent structure and strain determination of CdSe nanoparticles using atomic pair distribution function analysis", *Phys. Rev. B*, **76**, 115413.

M. McElfresh, S. Li & R. Sager. "Effects of magnetic field uniformity on the measurement of superconducting samples", `www.qdusa.com/sitedocs/appNotes/mpms/effects.pdf`.

R. E. A. McKnight, M. A. Carpenter, T. W. Darling, A. Buckley & P. A. Taylor (2007). "Acoustic dissipation associated with phase transitions in lawsonite, $CaAl_2Si_2O_7(OH)_2 \cdot H_2O$", *Am. Mineral.*, **92**, 1665–72.

R. E. A. McKnight, C. J. Howard& M. A. Carpenter (2009). "Elastic anomalies associated with transformation sequences in perovskites: I. Strontium zirconate, $SrZrO_3$", *J. Phys.: Cond. Matter*, **21**, 015901.

R. E. A. McKnight, T. Moxon, A. Buckley, P. A. Taylor, T. W. Darling & M. A. Carpenter (2008). "Grain size dependence of elastic anomalies accompanying the alpha-beta phase transition in polycrystalline quartz", *J. Phys.: Cond. Matter*, **20**, 075229.

H. J. McSkimin (1964). "Ultrasonic methods for measuring the mechanical properties of liquids and solids." in: *Physical Acoustics*, Academic Press, New York.

A. Migliori & J. L. Sarrao (1997). "Resonant Ultrasound Spectroscopy: applications to physics, material measurements and nondestructive evaluation", Wiley, New York.

S. Mori, C. H. Chen & S-W. Cheong (1998a). "Paired and unpaired charge stripes in the ferromagnetic phase of $La_{0.5}Ca_{0.5}MnO_3$", *Phys. Rev. Lett.*, **81**, 3972–75.

S. Mori, C. H. Chen & S-W. Cheong (1998b). "Pairing of charge-ordered stripes in (La,Ca)MnO_3", *Nature*, **392**, 473–6.

M. Moseman & K. Pitzer (1941). "Thermodynamic properties of the crystalline forms of silica", *J. Am. Chem. Soc.*, **63**, 2348–56.

D. Njoya, M. Hajjaji & D. Njopwouo2012). "Effects of some processing factors on technical properties of a clay-based ceramic material", *Appl. Clay Sci.*, **65–66**, 106–113.

A. Nukui, H. Nakazawa & M. Akao (1978). "Thermal changes in monoclinic trydimite", *Am. Min.*, **63**, 1252–9.

A. Nukui & O. W. Flörke (1987). "Tridymite structural modifications and cristobalite intergrown in one crystal", *Amer. Miner.*, **72**, 167–9.

L. Oravova, Z. Zhang, N. Church, R. J. Harrison, C. J. Howard & M. A. Carpenter (2013). "Elastic and anelastic relaxations accompanying magnetic ordering and spin-flop transitions in hematite, Fe_2O_3", *J. Phys.: Cond. Matter*, **25**, 116006.

D. C. Palmer (1994). "Stuffed derivatives of the silica polymorphs", in: *Physical Behavior, Geochemistry and Materials Applications*, Vol. 29 Reviews in Mineralogy. Mineralogical Society of America Publication, Washington DC.

R. Pandu (2014). "$CrFe_2O_4$ - $BiFeO_3$ perovskite multiferroic nanocomposites – A Review", *Mat. Sci. Res. India*, **11**(2), 128–45.

F. Parisi, P. Levy, L. Ghivelder, G. Polla & D. Vega (2001). "Magnetoresistance induced by low-field control of phase separation in $La_{0.5}Ca_{0.5}MnO_3$", *Phys. Rev. B*, **63**, 144419.

M. P. Pechini (1967). "Method of preparing lead and alkaline-earth titanates and niobates and coating method using the same to form a capacitor", U.S. Patent No. 3, 330, 697.

M. Pissas & G. Kallias (2003). "Phase diagram of the $La_{1-x}Ca_xMnO_3$ compound (0.5 $\leq$ x $\leq$ 0.9)", *Phys. Rev. B*, **68**, 134414.

Th. Proffen, S. J. L. Billinge, T. Egami & D. Louca (2002). "Structural analysis of complex materials using the atomic pair distribution function – a practical guide", *Z. Kristallogr.*, **218**, 132–43.

A. Putnis (1992). "Introduction to mineral sciences", Cambridge University Press, New York.

T. Qian, R. K. Zheng, T. Zhang, T. F. Zhou, W. B. Wu & X. G. Li (2005). "Effect of Jahn-Teller interactions on the specific heat and magnetic properties of charge-ordered $La_{1-x}Ca_xMnO_3$ (0.55 $\leq$ x $\leq$ 0.87) compounds", textitPhys. Rev. B, **72**, 024432.

P. G. Radaelli, D. E. Cox, M. Marezio & S-W. Cheong (1997). "Charge, orbital, and magnetic ordering in $La_{0.5}Ca_{0.5}MnO_3$", *Phys. Rev. B*, **55**, 3015–23.

P. G. Radaelli, D. E. Cox, M. Marezio, S-W. Cheong, P. E. Schiffer & A. P. Ramirez (1995). "Simultaneous structural, magnetic, and electronic-transitions in $La_{1-x}Ca_xMnO_3$ with x = 0.25 and 0.50", *Phys. Rev. Lett.*, **75**, 4488–91.

A. P. Ramirez, S-W. Cheong & P. Schiffer (1997). "Colossal magnetoresistance and charge order in$La_{1-x}Ca_xMnO_3$", *J. Appl. Phys.*, **81**, 5337–42.

A. P. Ramirez, P. Schiffer, S-W. Cheong, C. H. Chen, W. Bao, T. T. M. Palstra, P. L. Gammel, D. J. Bishop & B. Zegarski (1996). "Thermodynamic and electron diffraction signatures of charge and spin ordering in $La_{1-x}Ca_xMnO_3$", *Phys. Rev. Lett.*, **76**, 3188–91.

S. S. Rao, K. N. Anuradha, S. Sarangi & S. V. Bhat (2005). "Weakening of charge order and antiferromagnetic to ferromagnetic switch over in $Pr_{0.5}Ca_{0.5}MnO_3$ nanowires ", *Appl. Phys. Lett.*, **87**, 182503.

S. S. Rao, S. Tripathi, D. Pandey & S. V. Bhat (2006). "Suppression of charge order, disappearance of antiferromagnetism, and emergence of ferromagnetism in $Nd_{0.5}Ca_{0.5}MnO_3$ nanoparticles", *Phys. Rev. B*, **74**, 144416.

W. Rehwald (1973). "The study of structural phase transitions by means of ultrasonic experiments", *Adv. Phys.*, **22**, 721–55.

P. Richet, Y. Bottinga, L. Denielou, J. Petitet & C. Tequi (1982). "Thermodynamic properties of quartz, cristobalite and amorphous SiO_2: drop calorimetry measurements between 1000 and 1800 K and a review from 0 to 2000 K", *Geochim. Cosmochim. Acta*, **46**, 2639–58.

H. M. Rietveld (1969). "A Profile Refinement Method for Nuclear and Magnetic Structures", *J. Appl. Crystallogr.*, **2**, 65–71.

H. M. Rietveld (2010). "The Rietveld method. A retrospection", *Z. Kristallogr.*, **225**, 545–7.

F. Rivadulla, M. Freita-Alvite, M. A. Lopez-Quintela, L. E. Hueso, D. R. Miguens, P. Sande & J. Rivas (2002). "Coexistence of paramagnetic-charge-ordered and ferromagnetic-metallic phases in $La_{0.5}Ca_{0.5}MnO_3$ evidenced by electron spin resonance", *J. Appl. Phys.*, **91**, 785–8.

E. E. Rodriguez, Th. Proffen, A. Llobet, J. J. Rhyne & J. F. Mitchell (2005). "Neutron diffraction study of average and local structure in $La_{0.5}Ca_{0.5}MnO_3$", *Phys. Rev. B*, **71**, 104430.

E. Rozenberg, M. I. Tsindlekht, I. Felner, E. Sominski, A. Gedanken, Ya. M. Mukovskii & C. E. Lee (2009). "Size and nonstoichiometry effects on magnetic properties of $La_{0.5}Ca_{0.5}MnO_3$ manganite", *IEEE Trans. Magn.*, **45**, 2576–79.

D. Sanchez, M. J. Calderon, J. Sanchez-Benitez, A. J. Williams, J. P. Attfield, P. A. Midgley& N. D. Mathur (2008). "Limited local electron-lattice coupling in manganites", *Phys. Rev. B*, **77**, 092411.

T. Sarkar, B. Ghosh, A. K. Raychaudhuri & T. Chaterji (2008). "Crystal structure and physical properties of half-doped manganite nanocrystals of less than 100 nm size", *Phys. Rev. B*, **77**, 235112.

P. Schiffer, A. P. Ramirez, W. Bao & S-W. Cheong (1995). "Low Temperature Magnetoresistance and the Magnetic Phase Diagram of $La_{1-x}Ca_xMnO_3$", *Phys. Rev. Lett.*, **75**, 3336–39.

J. F. Shackelford & R. H. Doremus (2008). "Ceramic and glass materials: structure, properties and processing". Springer, New York.

R. D. Shannon (1976). "Revised effective ionic radii and systematic studies of interatomic distances in halides and chalcogenides", *Acta Crystallogr.*, A**32**, 751–67.

S. Shukla & S. Seal (2005). "Mechanisms of room temperature metastable tetragonal phase stabilisation in zirconia", *Int. Mater. Rev.*, **50**, 45–64.

V. Siruguri, P. D. Babu, S. D. Kaushik, A. Biswas, S. K. Sarkar, M. Krishnan & P. Chaddah (2013). "Neutron diffraction evidence for kinetic arrest of first order magneto-structural phase transitions in some functional magnetic materials", *J. Phys.: Cond. Matter*, **25**, 496011.

J. C. Slonczewsk & H. Thomas (1970). "Interaction of elastic strain with the structural transition of strontium titanate", *Phys. Rev. B*, **1**, 3599–608.

R. L. Snyder, F. Jaroslav & H. J. Bunge (1999). "Defect and microstructure analysis by diffraction", Vol. 10

International Union of Crystallography Monographs on Crystallography. Oxford Science Publications, New York.

R. Stevens (1983). "Introduction to zirconia", Magnesium Elektron Limited, 1–22.

T. Suzuki & T. Katsufuji (2008). "Magnetodielectric properties of spin-orbital coupled system Mn_3O_4", *Phys. Rev. B*, **77**, 220402(R).

R. I. Thomson, T. Chatterji, C. J. Howard, T. T. M. Palstra & M. A. Carpenter (2014). "Elastic anomalies associated with structural and magnetic phase transitions in single crystal hexagonal $YMnO_3$", *J. Phys.: Cond. Matter*, **26**, 045901.

S. V. Trukhanov, I. O. Troyanchuk, H. Szymczak & K. Barner (2002). "Phase transitions in the $La_{0.5}Ca_{0.5}MnO_{3-y}$ manganites", *Phys. Stat. Sol. b*, **229**, 1417–26.

W. M. Visscher, A. Migliori, T. M. Bell & R. A. Reinert (1991). "On the normal-modes of free-vibration of inhomogeneous and anisotropic elastic objects", *J. Acoust. Soc. Am.*, **90**, 2154-62.

A. M. Venezia, V. L. Parola, A. Longo & A. Martorana (2001). "Effect of alkali ions on the amorphous to crystalline phase transition of silica", *J. Solid State Chem.*, **161**(2), 373–8.

B. E. Warren (1969). "X-ray diffraction", Addison-Wesley Publishing Company, Reading, MA.

R. K. Zheng, R. X. Huang, A. N. Tang, G. Li, X. G. Li, J. N. Wei, J. P. Shui & Z. Yao (2002a). "Internal friction and Jahn-Teller effect in the charge-ordered $La_{1-x}Ca_xMnO_3$ (0.5 < x < 0.87)", *Appl. Phys. Lett.*, **81**, 3834–36.

R. K. Zheng, G. Li, A. N. Tang, Y. Yang, W. Wang, X. G. Li, Z. D. Wang & H. C. Ku (2003). "The role of the cooperative JahnâĂŞTeller effect in the charge-ordered $La_{1-x}Ca_xMnO_3$ ($0.5 \leq x \leq 0.87$) manganites", textitAppl. Phys. Lett., **83**, 5250–2.

R. K. Zheng, C. F. Zhu & X. G. Li (2001). "Magnetic field dependent on ultrasonic sound velocity and attenuation in charge-ordering manganese oxide $La_{0.5}Ca_{0.5}MnO_3$", *Phys. Stat. Sol. a*, **184**, 251–6.

R. K. Zheng, C. F. Zhu, J. Q. Xie & X. G. Li (2000). "Structural change and charge ordering correlated ultrasonic anomalies in $La_{1-x}Ca_xMnO_3$ (x = 0.5, 0.83) perovskite", *Phys. Rev. B*, **63**, 024427.

R. K. Zheng, C. F. Zhu, J. Q. Xie, R. X. Huang & X. G. Li (2002b). "On-line phase transition in $La_{1-x}Sr_xMnO_3$ ($0.28 \leq x \leq 0.36$) perovskites through ultrasonic studies", *Mat. Chem. Phys.*, **75**, 121–4.

C. F. Zhu & R. K. Zheng (1999a). "Ultrasonic anomalies in $La_{0.67}Ca_{0.33}Mn_{1-x}Zn_xO_3$ perovskites", *J. Phys. Condens. Mater.*, **11**, 8505–10.

C. Zhu, R. Zheng, J. Su & J. He (1999b). "Ultrasonic anomalies in $La_{0.67}Ca_{0.33}MnO_3$ near the Curie temperature", *Appl. Phys. Lett.*, **74**, 3504–6.

C. Zhu, R. Zheng, J. Su & W. Shong (2000). "Ultrasonic behaviours near different phase transitions in $La_{1-x}Ca_xMnO_3$", *J. Phys.: Cond. Matter*, **12**, 823–28.

The results described in the present thesis have been published in three different papers: i) L. Pagliari, M. Dapiaggi, A. Pavese & F. Francescon (2013), "A kinetic study of the quartz-cristobalite phase transition", *Journal of the European Ceramic Society*, 33, 3403-3410; ii) L. Pagliari, M. Dapiaggi, F. Maglia, T. Sarkar, A. K. Raychaudhuri, T. Chatterji & M. A. Carpenter (2014) "Strain heterogeneity and magnetoelastic behaviour of nanocrystalline half-doped La, Ca manganite, $La_{0.5}Ca_{0.5}MnO_3$", *Journal of Physics: Condensed Matter*, 26, 435303-435315; iii) M. Dapiaggi, F. Maglia, L. Pagliari, I. G. Tredici & N. Rotiroti (2014), "The role of local structural distortions in the stabilisation of undoped nanocrystalline tetragonal zirconia", *Materials Chemistry and Physics*, 147, 395-402.

Acknowledgments

In the previous theses, I thanked and mentioned a lot of people.
This time I wanna give special thanks to my supervisor, Monica Dapiaggi. She has been patient with me and supported me, for better or worse, for three entire years. She never made pressures on me and let me work with my times. And, above all, she teached me not only science, but also ways to live: everything is possible; seize the opportunities; act more and think less. I still have troubles in some situations, but I have been able to do a lot of things which I couldn't think before. Her encouragement was determining.
A mention to my parents is right, as they were always present and helped me and sustained me, especially during my bad times.
Finally, many thanks to Prof. Alessandro Pavese and Prof. Michael. A. Carpenter for their valuable scientific contributions.

Nelle tesi precedenti ho citato e ringraziato molte persone.
Questa volta, desidero fare un ringraziamento speciale alla mia tutor, Monica Dapiaggi. È stata paziente con me e mi ha sopportato, nel bene e nel male, per tre anni interi. Non mi ha mai fatto pressioni e mi ha permesso di lavorare coi miei tempi. E soprattutto, mi ha insegnato non solo nozioni scientifiche, ma anche modi di vivere: tutto *è* possibile; cogli le opportunità; buttati. Ho ancora dei problemi ad applicare questi insegnamenti in certe situazioni, ma sono molto migliorata, tant'è vero che sono riuscita a fare cose prima impensabili per me. Il suo incoraggiamento è stato determinante.
Un cenno ai miei genitori è d'obbligo, poichè sono sempre stati presenti e mi hanno saputo aiutare e sostenere, soprattutto nei miei momenti più brutti.
Infine, molti ringraziamenti a Prof. Alessandro Pavese e Prof. Michael A. Carpenter per i loro preziosi contributi scientifici.